Ultrahigh Frequency Characterization of Complex Materials Using Transient Grating Techniques

by

Timothy Francis Crimmins

B.S. Chemistry, Michigan State University, 1995

Submitted to the Department of Chemistry in partial fulfillment of the requirements for the degree of

DOCTOR OF PHILOSOPHY

at the

MASSACHUSETTS INSTITUTE OF TECHNOLOGY

June 2000

Signature of Author Signature redacted
Department of Chemistry
May 2, 1997

Certified by Signature redacted
Keith A. Nelson
Thesis Supervisor

Accepted by Signature redacted
Robert W. Field
Chairman, Departmental Committee on Graduate Students

This doctoral thesis has been examined by a committee of the Department of Chemistry as follows:

Professor Jeffrey I. Steinfeld — Signature redacted — Chairman

Professor Keith A. Nelson — Signature redacted — Thesis Supervisor

Professor Robert W. Field — Signature redacted

Ultrahigh Frequency Characterization of Complex Materials Using Transient Grating Techniques

by

Timothy Francis Crimmins

Submitted to the Department of Chemistry
on May 17, 2000 in Partial Fulfillment of the
Requirements for the Degree of Doctor of Philosophy in
Chemistry

Abstract

In a first set of experiments, a transient grating technique is used to detect picosecond acoustic pulses in supported metal films. Crossed femtosecond laser pulses generate acoustic responses with longitudinal components propagating normal to the film plane and surface acoustic wave components propagating in the film plane. Surface "ripple" associated with both components is detected through the diffraction of a probe beam. The measurements yield enhanced information content for characterization of film thickness and mechanical properties.

In a second set of experiments, phonon-polariton dispersion is characterized in ferroelectric lithium tantalate and lithium niobate through femtosecond time-resolved impulsive stimulated Raman scattering (ISRS). An improvement in the ISRS setup permits optical heterodyne detection of the signals. In addition to substantially increasing the sensitivity and accuracy of the measurements, the phase sensitivity of heterodyne detection makes it possible to fully characterize the polariton wave after it has propagated outside of the excitation region. The detection of propagating responses with heterodyned ISRS is explored theoretically and experimentally. Discrepancies in earlier results reported for these materials are resolved.

In a third set of preliminary experiments, a simple terahertz spectrometer is demonstrated. Two, crossed femtosecond pulses drive a tunable, terahertz frequency, polariton response in a ferroelectric crystal. The polariton is detected in a second crystal following propagation through a liquid sample layer.

Finally, heterodyne ISRS is used to study phonon-polariton responses in thin lithium tantalate crystals. Multiple polariton response frequencies are observed across a range of wavevectors as the polariton wavelength approaches the crystal thickness. These beating patterns are tentatively assigned to waveguide effects.

Thesis Supervisor: Keith A. Nelson
Title: Professor of Chemistry

Acknowledgements

I would like to begin by thanking my advisor, Keith Nelson. I have tremendous respect for his energy, enthusiasm, and passion for understanding; I try to emulate these qualities in my own approach to science.

In my years here at MIT, I've been lucky to stand on some immensely broad shoulders. First and foremost, I've had the incredibly good fortune of working with Alex Maznev over the course of several years. I consider Alex both a true friend and mentor. I could not possibly overstate his contributions to this thesis and to my development as a scientist. I am deeply indebted to Jianping Zhou for leaving us with a world-class laser system, for reinventing the way that we build with ultrafast optics, for countless hours of telephone technical support, and for his friendship. Ciaran Brennan provided me with a deep background in both scientific and experimental methods, as well as naming me the heir to an expertly designed transient grating instrument. I thank Gregor Diezemann for expanding my way of thinking about science and the world, and for many calamari excursions to the North End. I thank Marc Wefers for an introduction to pulse shaping and the world of ultrafast lasers. Greg Wakeham and Richard Koehl have been remarkable colleagues to share a lab with during my tenure here at MIT. I thank them for years of advice, conversation, and friendship. I thank the many other past and present members of the Nelson group that I've had the privilege of working with: Dutch, Dora, Rebecca, Mike, Nikolay, Peter, Dave, Jaime, Christ, O.V., and the many other post-docs and visiting scientists who have spent time in the Nelson group. Finally, I would like to thank Bill Behring, my high school chemistry teacher and George Leroi, my research advisor at Michigan State University for their guidance and for spreading their fondness for science to me.

I could never have stayed sane without venting my tirades to the gallery at 148 Spring St.: Jason, Geoff, Greg, Richard and Joe. From Red Sox games with Geoff to trips, projects, and ribs with Joe, we've always managed to keep it interesting. Michelle, I thank you so much for your love and support over the past couple of years. You have stood by my and encouraged me throughout and I am tremendously grateful.

The nature versus nurture debate may continue on, but in my case, there is no question. I owe my family a priceless debt of gratitude; they have played a critical role in making me who I am today. I thank them for instilling in me an unabashed commitment to excellence and for sharing science with me from an early age, as reading the pH of fish tank water and growing sugar crystals in the kitchen remain some of my earliest childhood memories. My mother and father deserve a great deal of credit for what we've been able to accomplished here, and it is to them that I dedicate this thesis.

To Mom and Dad

Table of Contents

Chapter 1. Introduction

Physics is often defined as the study of nature using math. More generally, the scientist seeks to explain and understand nature in a quantitative way. Probing the manner in which matter interacts with light has long served as a means to this end, beginning with simple measurements of absorption spectra and extending to complicated, non-linear optical experiments performed with multiple beams and perhaps even very short pulses of light. The results from these experiments have played an important role in the development of our understanding of nature, in everything from the formulation of quantum mechanics to the search for the causes of the hole in the ozone layer.

In this thesis work, ultrashort pulses of light (~25 femtosecond duration) will be used to characterize the optical properties of a variety of materials (loosely defined as substances with useful properties). Our general approach will be to use a first, short pulse of light to drive an excitation (such as vibrations of molecules in a lattice) in a material, and then to characterize the sample's response in the time domain (i.e., to "watch" the behavior of the excited sample as time passes) via a second pulse of light. For a vibrational response, the molecules in the sample may be thought of as a ball attached to a spring. The first pulse of light acts like a hammer, causing the molecules to oscillate as a ball attached to a spring might be caused to do. A probe pulse would then "watch" the molecules vibrate up and down, just as one might imagine watching the ball bounce up and down at the end of a spring. Returning to the general case, the sample's response may be used as a guide in developing models (quantitative explanations) with the power to correctly predict sample behavior, much as the frequency of a bouncing ball can be used to determine the mass of the ball and the stiffness of the spring. It is from this process that

we hope to glean a fundamental understanding of the interactions in the materials that we study.

For many different types of responses, a single excitation pulse, which is roughly uniform across its spatial profile, will produce a response that is fairly simple to model. However, some classes of material responses are dispersive (the material's behavior at one point in space is a sensitive function of its behavior at a different point that is a macroscopic distance away). Examples of these types of responses include surface waves on water, acoustic (sound) waves, and phonons (lattice waves) in ionic crystals. In these cases, a spatially uniform excitation pulse may not be the simplest approach to the problem. Imagine trying to develop an explanation for surface waves on water using two different methods: first by dropping a large rock in the center of a lake and then observing the wave pattern and second by observing the lake during many different wind and wave conditions in which a variety of different wavelengths can be monitored. One can imagine that, in order to develop a complete understanding of the water waves, it may well be desirable to observe, say, the speed of many different wavelengths of surface waves (or, in the parlance used throughout this work, to measure the dispersion curve of the surface waves). To generalize, the behavior of a system is often much simpler when a response with a specific, well-defined wavelength can be excited. In order to excite a response whose wavelength can be changed in a controllable fashion, two pulses of light can be crossed at an angle. The interference pattern, which results from the overlap between these two beams, will have wavelength that can be controlled by adjusting the angle between the two beams! In other words, by using two, crossed excitation pulses in place

of a single pulse, the material's behavior can be studied under a broad, controllable range of "wave conditions".

The optical properties of an excited material are typically a sensitive function of the amplitude of the excitation. For example, the index of refraction of a crystal whose molecules have been driven by a pair of crossed excitation pulses will vary with time as the molecules vibrate in the crystal. Because a crossed pair of pulses was used, the displacement of the molecules will vary not only in time but also in space; for instance the molecules that were positioned in the peaks of the interference pattern produced by the excitation pulses will be oscillating at a relatively large amplitude while those positioned in the nulls of the interference pattern will not be vibrating at all. This spatially periodic variation in the crystal's refractive index (optical properties) can act as an optical grating, diffracting a pulse that passes through it. This is, in fact, how the material's response to the crossed excitation pulses is measured in general. A probe beam is diffracted off of the transient grating (spatially periodic variation in the crystal's refractive index which varies in time, hence the modifier transient), and the intensity of the diffracted probe pulse is measured as a function of time in order to map out the response of the sample to the two, crossed excitation pulses.

The primary impediment to the more widespread application of this technique is that the intensity of the diffracted beam is proportional to the square of the amplitude of the material response, as shown for a variety of different cases in Chapters 2, 3, and 5. This makes it very difficult to characterize samples that have weak or complicated responses, as illustrated in Chapters 3 and 4. In Chapter 3, the transient grating technique is used to drive and detect acoustic pulses in metal films, a metrology method that can be

used to measure things like the physical properties of individual films in a multi-layered film stack and the orientation of crystallites in a thin metal film. These experiments come close to the weak-sample limits of the transient grating technique.

The transient grating technique can be significantly advanced and extended if the diffracted pulse is mixed with another pulse of light. Called heterodyne detection, this is the same method used in most FM radio receivers to decode the audio signal. Chapter 4 presents a heterodyne detection system consisting of an optical apparatus with a diffractive optic as its distinguishing element and detection electronics, for the heterodyne detection of transient gratings on a femtosecond timescale. This apparatus is shown to produce results which are substantially better than those recorded from diffraction alone. This apparatus is also shown to have improved resolution and to be quite easy to align.

In Chapter 5, the heterodyne transient grating technique is applied to the study of lattice waves in the ferroelectric crystals. Ferroelectric materials have a permanent, electric dipole moment (much like ferromagnetic materials have a permanent magnetic dipole), as entire planes of ions in the lattice are displaced from their central positions. Crossed laser pulses are used to drive and detect oscillations of these planes of ions, through a process called impulsive stimulated Raman scattering. As the planes of ions vibrate, they act as antennae, emitting radiation that, for certain spatial wavelengths (for certain angles between the two, crossed pulses) will constructively interfere throughout the crystal. As a result, the lattice wave couples to a light wave, and this mixed excitation is called a phonon-polariton, as explained in Chapter 5. The dispersion curve for these phonon-polaritons is very sensitive to the forces acting on these planes of ions, and consequently to the interactions that lead to the material's ferroelectricity. In Chapter 5,

the heterodyne technique is used to clarify contradictory results from past literature, lending credence to a specific model for the lattice dynamics containing a two-well potential energy surface for the motion of the ions. The heterodyne detection of propagating waves is developed both theoretically and experimentally and features of the damping properties of the phonons-polaritons are explained. Finally, lattice waves at many different frequencies are resolved all at the same time, further illustrating the power of the heterodyne technique to characterize complicated responses.

Chapter 6 showcases preliminary experimental results from two promising future applications of the heterodyne transient grating technique. First, a new spectroscopic application of phonon-polariton excitation and detection, going beyond the study of the phonon-polaritons, is made possible by the phase sensitivity of heterodyne detection. A phonon-polariton is excited in one ferroelectric crystal, after which it is allowed to propagate out of the crystal, into a liquid sample, and then back into another crystal where it is detected in the usual manner. This can be used to learn about the optical behavior of the liquid sample in the terahertz region of the frequency spectrum, which is difficult to study by other means. Second, the improvements that heterodyne detection provides permit an extension of the sample range to include ferroelectric thin films. Data are shown from thin ferroelectric crystals showing clear waveguide effects.

The femtosecond time-scale, heterodyne detection of transient gratings is shown to be a powerful tool for the characterization of ultrahigh frequency material responses. The technique is applied here to the study of a broad range of complex materials, yielding insights into the lattice dynamics of lithium tantalate and lithium niobate, the behavior of propagating responses, and the terahertz frequency dielectric response of glycerol.

Chapter 2. Classical Description of Stimulated Raman Scattering

Theoretical descriptions of one type of ISS, impulsive stimulated Raman scattering (ISRS), will be presented in this chapter. In this section, ISRS will be described using the framework developed for frequency domain nonlinear optics. The purpose of this section is to facilitate a mapping between nonlinear optics in the frequency domain, where an abundance of accessible introductory texts and literature exists, to nonlinear spectroscopy in the time domain, where, in this author's opinion, there exists a marked dearth of introductory material. In Chapter 3, a theoretical description of impulsive stimulated thermal scattering (ISTS) in a transient grating configuration will be presented. In Chapters 4 and 5, heterodyne transient grating ISRS experiments will be.

The theoretical descriptions, especially those in later chapters, will focus upon the relationship between the observables measured in ISS experiments and the behavior of the physical properties of the material under study. This approach will culminate in a description in which the act of probing the material response will be modeled as the action of a filter upon the true material response. Well designed experiments lead to a nearly transparent filter, while in other cases more substantial distortions can occur.

The objective of this section is to derive through classical mechanics an expression for the electric field produced by impulsive stimulated Raman scattering from a collection of polarizable harmonic oscillators. The strategy will be to first derive expressions for continuous-wave (CW) excitation and probing, i.e., frequency domain stimulated Raman scattering, following the treatment of Yariv [1], and then to convert these expressions to those for the case of temporally impulsive pumping and probing. This somewhat circuitous route will be taken for two reasons: to draw upon intuition about traditional,

frequency-domain Raman scattering and to stress the connection between the time-domain and frequency-domain treatments and information contents.

In a Raman scattering experiment, an electromagnetic wave at frequency ω_1 is scattered by thermally excited vibrations of a sample. The scattered light is frequency-shifted by the natural vibrational frequency, yielding signal that is detected at the Stokes and anti-Stokes scattered frequencies $\omega_2^S = \omega_1 - \omega_0$ and $\omega_2^{AS} = \omega_1 + \omega_0$. Raman scattering is defined as spontaneous when no light at frequency ω_2 is present initially. The amplitude of the scattered field at frequency ω_2 is linearly proportional to that of the input field at frequency ω_1.

In stimulated Raman scattering, both ω_1 and ω_2 frequency components are initially present in the excitation light field. Usually this is achieved through the use of two distinct laser beams at the two frequencies. These two components exert a force on Raman-active vibrational modes at the difference frequency $\omega_1-\omega_2=\omega$, resulting in coherent vibrational oscillations driven at that frequency. The coherent vibrational response can then scatter a third, probe light beam in a fashion similar to the scattering of light by thermal excitations in spontaneous Raman scattering. However, in this case the vibrations are coherent, with the same spatial and temporal characteristics, so the scattering can be thought of as "diffraction" and the scattered light is a coherent beam that leaves the sample in a well defined direction.

Note that spontaneous and stimulated scattering processes involve change in the light wavevector as well as frequency. The beams at frequency ω_1 and ω_2 are specified also by their corresponding wavevectors $\vec{k}_1$ and $\vec{k}_2$, and the scattering process involves a

vibrational excitation at the difference wavevector $\vec{q} = \vec{k}_1 - \vec{k}_2$ as well as the difference frequency ω.

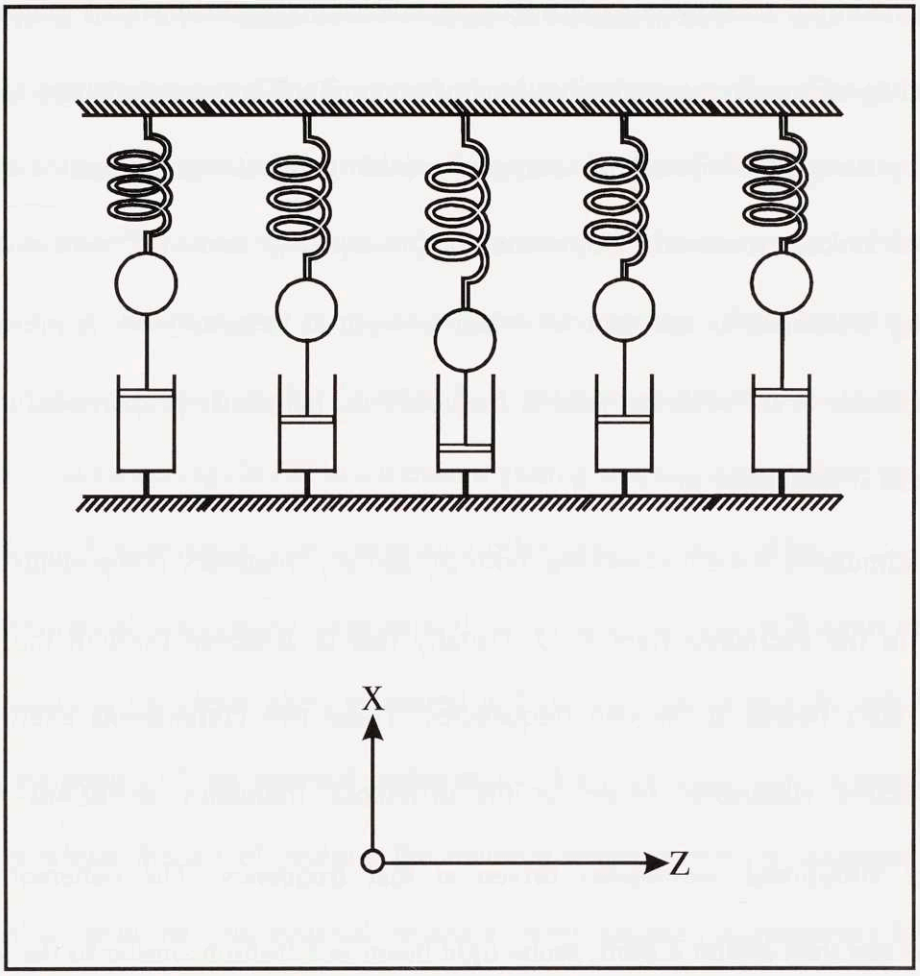

Figure 2.1. A condensed phase system is modeled as a collection of damped, harmonic oscillators in the derivation of the ISRS response.

The material will be modeled as a collection of N independent, polarizable harmonic oscillators. This model can be used to accurately represent excitations like phonons and molecular vibrations (and polaritons with several additional considerations). The analysis will be two dimensional, with each oscillator being described by its position x, z and normal vibrational coordinate $Q(t,\vec{r})$, see figure 2.1. The equation of motion for a single oscillator is :

$$\frac{dQ}{dt^2} + \gamma \frac{dQ}{dt} + \omega_0^2 Q = \frac{F(t,\vec{r})}{m} \tag{2.1}$$

Here ω_0 is the natural frequency of the oscillator, γ is the damping constant, $F(t,\vec{r})$ is the driving force and m is the mass or reduced mass of the oscillator.

First, expressions for the response of the oscillators to a CW optical field with two frequency components ω_1 and ω_2 will be found, ignoring all effects of the field except those which will be called the Raman force. The vibrational response to a temporally impulsive optical field will then be derived, and finally the prescription for treating pump pulses with an arbitrary electric field profile (e.g. femtosecond pulse sequences) will be described. Second, the time dependent polarization resulting from the interaction of a CW probe beam with the excited material will be found and used to derive the results for a temporally impulsive probe. Again, the prescription for generalization of these results to arbitrary probe electric field profiles will be laid out. Finally, the optical field produced by this time-dependent polarization, the ISRS signal field, will be found.

The optical driving force produced by the pump beam will be derived by considering the electrostatic stored energy density W in the oscillators:

$$W = \frac{1}{2}\varepsilon(Q)\vec{E}\cdot\vec{E} \tag{2.2}$$

The $Q(t,\vec{r})$ dependence of the dielectric constant ε will be treated by writing the dielectric constant in terms of the polarizibility α which can be expanded around $Q(t,\vec{r}) = 0$, keeping only terms up to first order in $Q(t,\vec{r})$:

$$\varepsilon = \varepsilon_0(1 + N\alpha(Q)) \cong \varepsilon_0\left\{1 + N\left[\alpha_0 + \left(\frac{\partial\alpha}{\partial Q}\right)_0 Q\right]\right\} \tag{2.3}$$

The force is now given by

$$F(t,\vec{r}) = \frac{\partial W}{\partial Q} = \frac{1}{2}\varepsilon_0 N\left(\frac{\partial \alpha}{\partial Q}\right)_0 \vec{E}\cdot\vec{E} \tag{2.4}$$

This force on the oscillators, proportional to the differential polarizability $(\partial\alpha/\partial Q)_0$ (a purely phenomenological quantity in this classical treatment) will be referred to as the Raman force.

In CW stimulated Raman scattering, the initial electromagnetic field contains two optical frequencies ω_1 and ω_2:

$$\vec{E}(t,\vec{r}) = \frac{1}{2}\hat{e}_1 E_e e^{i\left(\omega_1 t - \vec{k}_1\cdot\vec{r}\right)} + \frac{1}{2}\hat{e}_2 E_e e^{i\left(\omega_2 t - \vec{k}_2\cdot\vec{r}\right)} + c.c. \tag{2.5}$$

For simplicity, the two components of the electric field will be assumed to be polarized in the x direction (i.e., along the direction of the displacement of the oscillators), reducing the problem to a scalar one. It can be assumed without loss of generality that $\omega_1 > \omega_2$. The driving force is proportional to the square of this field, which contains sum and difference frequency components. The natural frequencies ω_0 of the oscillators, i.e., of the Raman-active molecular or lattice vibrational modes, are much less than the optical frequencies i.e., $\omega_0 << \omega_1, \omega_2$. Consequently, only the components of the Raman force at the difference frequency $\omega_1 - \omega_2$ may be near resonance with the vibrational frequencies, and only these terms may drive significant vibrational responses. Neglecting other components, the Raman driving force is given by:

$$F(t,\vec{r}) = \frac{N\varepsilon_0}{2}\left(\frac{\partial \alpha}{\partial Q}\right)_0 \left|E_e\right|^2 e^{i(\omega_1-\omega_2)t} e^{-i(\vec{k}_1-\vec{k}_2)\cdot\vec{r}} + c.c. \tag{2.6}$$

The problem is simply that of a driven harmonic oscillator, with traveling wave solutions of the form:

$$Q_{CW}(t,\vec{r}) = Q_{CW} e^{i(\omega_1-\omega_2)t} e^{-i(\vec{k}_1-\vec{k}_2)\cdot\vec{r}} + c.c. \tag{2.7}$$

given by insertion of (2.6) into (2.5). The coherent vibrational amplitude is:

$$Q_{CW} = \frac{N\varepsilon_0\left(\frac{\partial\alpha}{\partial Q}\right)_0 |E_e|^2}{2m\left(\omega_0^2 - (\omega_1-\omega_2)^2 + i\gamma(\omega_1-\omega_2)\right)} \tag{2.8}$$

Thus coherent vibrational oscillations at the difference frequency $\omega_1 - \omega_2$ are driven by the two field components through stimulated Raman scattering. The largest vibrational amplitude occurs when the oscillator is driven on resonance, i.e., $\omega_1 - \omega_2 = \omega_0$. The vibrational energy imparted to the oscillator, i.e., the average power P absorbed from the field, is given by the average of the force $F(t,\vec{r})$ times the velocity dQ_{CW}/dt and is described in the usual limit $\gamma << \omega_0$ by a Lorentzian function:

$$\langle P \rangle \propto \frac{1}{\omega_0^2 - \Delta\omega^2 + i\gamma\Delta\omega} \tag{2.9}$$

In "stimulated Raman gain" measurements, the intensity of light at frequency ω_2 is measured as frequency ω_1, and thus $\Delta\omega$, is scanned, revealing the Lorentzian response with its maximum at the vibrational resonance frequency[2]. Through the stimulated Raman scattering process, vibrational energy is produced as incident light at the higher frequency ω_1 is converted into scattered light at the lower frequency ω_2.

These expressions describe the dynamics of the coherent vibrational response $Q_{CW}(t,\vec{r})$ for the case of CW excitation. In impulsive stimulated scattering the excitation

field is that of an ultrashort laser pulse. For this purpose it will be useful to describe the response in terms of a vibrational susceptibility χ:

$$Q_{CW}(t,\vec{r}) = \frac{N\varepsilon_0\left(\frac{\partial\alpha}{\partial Q}\right)_0}{2}\chi(\omega_1,\omega_2)\left|E_e\right|^2\left[e^{i(\omega_1-\omega_2)t-i\vec{q}\cdot\vec{r}}\right]+c.c. \tag{2.10}$$

From (2.10), it is clear that:

$$\chi(\omega_1,\omega_2) = \frac{1}{m\left(\omega_0^2-(\omega_1-\omega_2)^2+i\gamma(\omega_1-\omega_2)\right)} \tag{2.11}$$

The spatial dependence of the response is described by the wavevector of the excitation force $\vec{q} = \vec{k}_1 - \vec{k}_2$. We have assumed the susceptibility itself does not have any explicit spatial dependence in the limit of optical wavelengths. Note that this assumption is valid for molecular vibrations and most optic phonons, but not for acoustic waves or polaritons whose resonance frequencies ω_0 and dephasing or damping rates γ are wavevector-dependent.

Equation (2.8) describes the vibrational amplitude resulting from a driving force that oscillates at any particular frequency $\omega = \omega_1 - \omega_2$. An impulsive (i.e., delta-function) driving force contains equal contributions from all frequencies, i.e., a "white" frequency spectrum. In order to find the response to impulsive excitation, the response to each frequency is found using equations (2.10) and (2.11) and the contributions are summed:

$$Q_\delta(t,\vec{r}) = \frac{N\varepsilon_0\left(\frac{\partial\alpha}{\partial Q}\right)_0}{2}\int_{-\infty}^{\infty}\chi(\omega_1-\omega_2)\left|E_e\right|^2 e^{i(\omega_1-\omega_2)t}e^{-i\left(\vec{k}_1-\vec{k}_2\right)\cdot\vec{r}}d\left(\omega_1-\omega_2\right)+c.c. \tag{2.12}$$

Note that a femtosecond pulse is a moving "pancake" of light whose thickness is given by the pulse duration times the speed of light. For example, a 33-fs pulse is just 10

microns thick, even though the spot size (i.e. the transverse dimensions) may be much larger. In the limit of a true delta function excitation pulse, the pulse is infinitely thin! In this limit, two crossed pulses only overlap at any time along a single line, regardless of the spot sizes, as the pulses move forward so does the position of the line of overlap. With a finite pulse duration, the pulses overlap and form an optical interference or "grating" pattern across a region of space with finite width in the transverse dimension, usually still much smaller than the spot sizes. The use of diffractive optics to produce the two pulses and an appropriate imaging system to cross them [3] results in a large region of overlap, essentially equal to the spot sizes, and therefore produces many interference fringes, as will be described in Chapter 4. Here we will assume that an interference pattern is formed in this manner, and we will not consider any effects of finite transverse dimension of the interference region. This arrangement also allows us to assume that the interference fringe spacing, or grating (or stimulated scattering) wavevector, is independent of the frequency of any component of the pulse. This facilitates our use of superposition to calculate the total vibrational response. This approach can be used because the vibrational response, although a nonlinear function of the optical field, is linear in the Raman force. Defining the fourier transform of $\chi(\omega_1 - \omega_2)$ as $G(t)$, equation (2.12) can be written:

$$Q_\delta(t) = G(t)F_\delta(t) \tag{2.13}$$

From this, it is clear that $G(t)$ is the impulse response of the system to the impulsive Raman force. The response function to an impulse at *t=0*, hereafter referred to as the impulse response function, is given by the fourier transform of (2.11):

$$G(t)=\begin{cases}\dfrac{2}{m}e^{-\gamma t/2}\sin(\omega_v t), & t>0\\ 0, & t<0\end{cases} \tag{2.14}$$

writing the underdamped frequency as $\omega_v=\sqrt{\omega_0^2-\gamma^2/4}$. This gives the response of the material to temporally impulsive excitation.

The material response to a general time-dependent pump electric field profile is given by the convolution of the corresponding time-dependent Raman force $F(t,\vec{r})$ produced by the field profiles with:

$$Q_F(t,\vec{r})=\int_{-\infty}^{\infty}G(t')\cdot F(t-t',\vec{r})dt', \tag{2.15}$$

Having derived the vibrational response driven through stimulated Raman scattering, we now turn our attention to coherent scattering of probe light by this response. The polarizability α of the oscillators depends on vibrational displacement $Q(t,\vec{r})$ as expressed in equation (2.3) through the differential polarizability $(\partial\alpha/\partial Q)_0$, and therefore the coherent vibrational oscillations of the sample produce coherent oscillations in the polarizability with the same spatial and temporal dependence as the vibrational displacement. The induced polarization is given by the product of the polarizability and the probe field:

$$P(t,\vec{r})=\varepsilon_0 N\alpha(Q)E_p(t,\vec{r})=\varepsilon_0 N\left[\alpha_0+\left(\frac{\partial\alpha}{\partial Q}\right)_0 Q(t,\vec{r})\right]E_p(t,\vec{r}) \tag{2.16}$$

This macroscopic polarization radiates the scattered field. The probe field $E_p(t,\vec{r})=(1/2)E_p e^{i(\omega_p t-\vec{k}_p\cdot\vec{r})}+c.c.$ is assumed to be weak (i.e., it does not significantly excite any new vibrations). For simplicity, only the polarization induced by the Raman

force, or the term in equation (2.16) proportional to the differential polarizability, will be considered. Assuming impulsive pump beams and assuming $\omega_0 >> \gamma$ for simplicity, equations (2.13) and (2.14) can be combined with equation (2.16) to give the following expression for the Raman polarization driven by the Raman force and a CW probe:

$$\begin{aligned} P_R(t,\vec{r}) &= \frac{\varepsilon_0^2 \pi N^2 |E_e|^2 \left(\frac{\partial \alpha}{\partial Q}\right)_0^2}{m\omega_v} e^{-\gamma t/2} \sin(\omega_v t)\cdot\cos(qz)\times\left[E_p e^{i(\omega_p\cdot(t-t_p)-\vec{k}_p\cdot\vec{r})} + c.c.\right] \\ &= \frac{\varepsilon_0^2 \pi N^2 |E_e|^2 \left(\frac{\partial \alpha}{\partial Q}\right)_0^2}{\omega_v} G(t)|E_e|^2 e^{-i(\vec{k}_1-\vec{k}_2)\cdot\vec{r}} E_p \times\left[e^{i(\omega_p\cdot(t-t_p)-\vec{k}_p\cdot\vec{r})} + c.c.\right] \end{aligned} \tag{2.17}$$

Expanding this result illustrates the new frequency and wavevector components in the Raman polarization:

$$\begin{aligned} P_R(t,\vec{r}) = {} & \frac{-\varepsilon_0^2 \pi N^2 E_p |E|^2 \left(\frac{\partial \alpha}{\partial Y}\right)_0^2}{4im\omega_v} e^{-\gamma t/2} e^{-i\omega_p t_p} \\ & \left\{\exp\left[i(\omega_p+\omega_v)t - i\left(\frac{\omega_v\cos\theta}{c}+k_{px}\right)x - i(k_{pz}+q)z\right]\right. \\ & +\exp\left[i(\omega_p+\omega_v)t - i\left(\frac{\omega_v\cos\theta}{c}+k_{px}\right)x - i(k_{pz}-q)z\right] \\ & -\exp\left[i(\omega_p-\omega_v)t - i\left(-\frac{\omega_v\cos\theta}{c}+k_{px}\right)x - i(k_{pz}+q)z\right] \\ & \left.-\exp\left[i(\omega_p-\omega_v)t - i\left(-\frac{\omega_v\cos\theta}{c}+k_{px}\right)x - i(k_{pz}-q)z\right] + c.c.\right\} \end{aligned} \tag{2.18}$$

It will be shown that this polarization radiates an electromagnetic field which is the ISRS signal. The optical dispersion relation $\omega = |k|c$ requires that the Stokes scattered signal at frequency $\omega_S = \omega_p - \omega_v$ have wavevector $|\vec{k}_p - \vec{q}| = \frac{\omega_S}{c}$. For crossed excitation pulses

that form a grating pattern, the probe beam can, at best, be incident at the "Bragg" diffraction angle, i.e., phase matched, such that half of the terms in (2.18) obey this condition. Once a choice is made from which side the probe beam will enter, only two of the forms, e.g. the first and fourth terms in (2.18) meet this condition and radiate a signal field; the other two would give equivalent results with the probe beam incident from the other side. This polarization will radiate a signal at new signal frequencies $\omega_s = \omega_p - \omega_v$ and $\omega_{AS} = \omega_p + \omega_v$ in a direction given by the "diffracted" signal wavevector. The time-dependence of the signal field reveals the material response function $G(t)$ whose elucidation is the usual objective of an ISRS experiment.

In principle, the ISRS measurement might be conducted using ultrashort (impulsive) excitation and a CW probe beam to produce the scattered field whose time dependence would be analyzed by a fast photodetector and digitizing electronics. In practice, this would require femtosecond time resolution in the detection system, and this is not conventionally available. Consequently, the experiment is carried out with an ultrashort probe pulse that is delayed by a specified time period t_p following excitation, and the signal generated from this probe pulse is used to measure the material response at just the single time that is probed. Then the excitation-probe sequence is repeated with a different time delay, and then with another, and so on, until the entire time-dependent sample response is determined in a point-by-point fashion along the time axis. What is measured at each time delay is the total amount of coherently scattered light i.e., time-integrated intensity of the signal field is measured by a slow detector. In order to describe this, the polarization produced by a temporally impulsive probe pulse will be found and used to find the polarization response to an arbitrary pulse shape.

The polarization produced by an impulsive probe field E_p^{δ} is found by integrating over all possible probe frequencies ω_p:

$$P_R^{\delta}(t-t_p) = G(t)E_p^{\delta}|E_e|^2\,\delta(t-t_p) \tag{2.19}$$

The response of the polarization to an impulsive probe at t_p is an impulse at t_p, with an amplitude proportional to the product of the electric field strengths and the time dependent response evaluated at t_p. The response of the polarization to a general probe temporal profile can be found by convolving the probe field with the response function:

$$P_R^{\delta}(t,t_p) = \int_{-\infty}^{\infty} G(t')E_p(t')|E_e|^2\,\delta(t-t'-t_p)dt' \tag{2.20}$$

Carrying out the integration gives:

$$P_R^{\delta}(t,t_p) = G(t_p)E_p(t-t_p)|E_e|^2 \tag{2.21}$$

Finally, the ISRS electric field can be found by entering the time dependent Raman polarization into Maxwell's equations as a source term:

$$\frac{\partial^2 E_y(t,\vec{r})}{\partial x^2} + \frac{\partial^2 E_y(t,\vec{r})}{\partial z^2} = \mu\varepsilon\frac{\partial^2 E_y(t,\vec{r})}{\partial t^2} + \mu\frac{\partial^2 (P_R)_y}{\partial t^2} \tag{2.22}$$

Making the usual slowly varying envelope approximation, i.e., $\frac{\partial^2 E_y(t,\vec{r})}{\partial z^2}, \frac{\partial^2 E_y(t,\vec{r})}{\partial x^2} << c^2\frac{\partial^2 E_y(t,\vec{r})}{\partial t^2}$, the ISRS field is given by:

$$E_y^{ISRS}(t,\vec{r}) = \frac{1}{\varepsilon}(P_R)_y \tag{2.23}$$

As explained above, the response function is typically recovered by repeatedly performing the ISRS experiment as incremental variations in the probe delay t_p are made.

For each t_p value, the intensity of the electric field produced by $P_R(t,\vec{r})$ is integrated by a slow detector:

$$S_{ISRS}(t_p) = \int_{-\infty}^{\infty} \left| G(t_p) E_p(t - t_p) F_\delta(t,\vec{r}) \right|^2 dt \tag{2.24}$$

In other words, the signal recovered in a typical ISRS experiment is the convolution of the system's response following excitation by the Raman force with the probe electric field temporal profile. If the probe pulse as well as the excitation pulses are short enough to be considered "impulsive" i.e., if no significant vibrational motion occurs during the pump and probe pulses, then the result can be simplified to:

$$S_{ISRS}(t_p) = \left| G(t_p) \right|^2 I_p \left| F_\delta(t_p) \right|^2 \tag{2.25}$$

In this case the signal directly gives the impulse response function. The signal is proportional to the probe intensity and the square of excitation intensity.

Note that heterodyne methods, which will be described in Chapter 4, have been demonstrated recently in which a strong reference beam propagates collinear and in phase with the signal beam. In this case the signal and reference fields add constructively, and the measured intensity is dominated by their product which is linear in the response function and the excitation intensity, as well as the probe intensity.

Most of the present discussion has emphasized the transient grating geometry in which crossed femtosecond excitation pulses are used and signal is produced by coherent scattering, or diffraction, of probe light. However, in general ISRS excitation occurs even when a single excitation pulse is incident on a Raman-active sample. Stimulated scattering occurs in the forward direction, with higher-frequency components of the incident pulse scattered into lower-frequency components still contained within the pulse

bandwidth. The probe pulse is collinear (or in practice, nearly collinear) with the excitation pulse and the signal is still derived from Equation (2.18) with $\theta = 0$ and $k_{pz} = 0$. Whether the coherently scattered probe light is Stokes or anti-Stokes shifted, i.e. which of the terms in Equation (2.18) dominates, depends on the probe delay relative to the excitation pulse. The results can be understood by considering the impulsive force exerted by the probe pulse, which unlike the excitation pulse encounters the sample already undergoing coherent vibrational oscillations. If the probe pulse arrives at the sample after an integral multiple of vibrational periods, then it drives vibrational motion in phase with that already under way, resulting in an increased vibrational amplitude. Therefore the probe pulse imparts vibrational energy to the system and emerges red-shifted. If the probe pulse arrives after, say, one-half the vibrational period, then the force it exerts opposes the motion already under way and the vibrational amplitude is decreased. The probe pulse takes vibrational energy away from the system and emerges blue-shifted. Thus the spectrum of the transmitted probe pulse "wags" back and forth from red to blue at the vibrational frequency. As we shall see, these time-dependent spectral shifts can be detected readily, and represent just one of several observables through which the results of ISRS excitation with a single pulse can be monitored.

1 A. Yariv, *Quantum Electronics* (John Wiley & Sons, New York, 1989).

2 Y. R. Shen, *Principles of nonlinear Optics* (Wiley, 1984).

3 A. A. Maznev, T. F. Crimmins, and K. A. Nelson, Opt. Lett. **23**, 1319 (1998).

Chapter III. Transient Grating Detection of Picosecond Acoustic Pulses in Metal Films

I. Introduction

A variety of methods have evolved for optical generation and detection of acoustic waves in bulk materials and thin films. Transient grating methods have been used extensively in transmission and reflection modes to examine acoustic waves in roughly the 10 MHz - 10 GHz frequency range [1-4]. As shown in Fig. 3.1 for the case of a thin film sample, two excitation pulses are crossed to produce an optical interference pattern with fringe spacing Λ. Optical absorption and sudden heating at the interference maxima (the transient grating "peaks") gives rise to thermal expansion which launches acoustic waves of wavelength Λ that propagate in the plane of the film. The excitation pulse duration must be short compared to the acoustic oscillation period to drive the transient acoustic response, and is typically in the 100 ps range. The acoustic response is usually monitored through time-resolved diffraction of probe light which occurs due to modulation or "ripple" of the film surface. This method has been used to examine properties of thin films including elastic modulii and thickness.

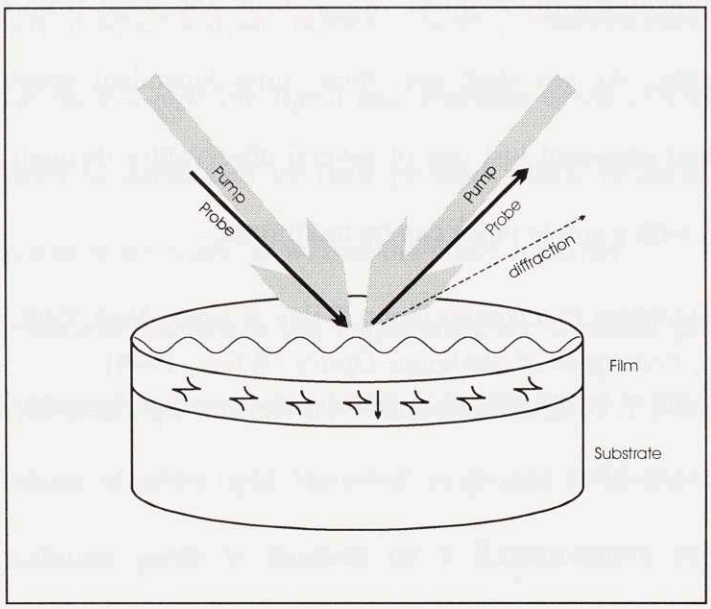

Fig. 3.1 Schematic diagram of the transient grating experimental technique for generation and detection of picosecond acoustic pulses.

Alternate methods have been used to examine acoustic responses that propagate normal to the plane of a thin film [5-8]. In this case, a single excitation pulse has been used to produce sudden heating at the film surface. Thermal expansion into the film launches an acoustic wavepacket that propagates through the film and that may undergo partial reflection back toward the surface upon reaching an interface. The wavepacket contains many wavevector components, up to roughly the inverse of the film thickness or light penetration depth into the sample. Typically, this yields corresponding acoustic frequency components up to several hundred GHz. The excitation pulse duration must be short compared to this high-frequency acoustic oscillation period to excite the full available acoustic bandwidth, and typically is on the order of 100 fs. The return of the acoustic wavepacket to the film surface is detected by a probe laser pulse, either through a strain-induced change in reflectivity [5-7] or via probe beam deflection resulting from surface displacement [8].

The use of transient grating methods to monitor through-plane as well as in-plane acoustic propagation has been suggested[9]. In this case the through-plane acoustic response is not localized at a single spot but is distributed throughout the grating pattern, with maxima in acoustic intensity at the grating peaks. Picosecond pulse durations used in thin-film grating measurements reported to date have proved too long to clearly resolve any through-plane acoustic response. Femtosecond time-resolved grating measurements in which both in-plane and through-plane acoustic propagation are monitored are reported in this chapter. The transient reflection grating (TRG) technique offers two main advantages: improved signal-to noise ratios and the ability to obtain through and in-plane information simultaneously.

II. Experimental

Because these experiments were performed prior to the development of the experimental detection system introduced in subsequent chapters, the experimental apparatus and detection electronics used here will be described in some detail. The apparatus is depicted

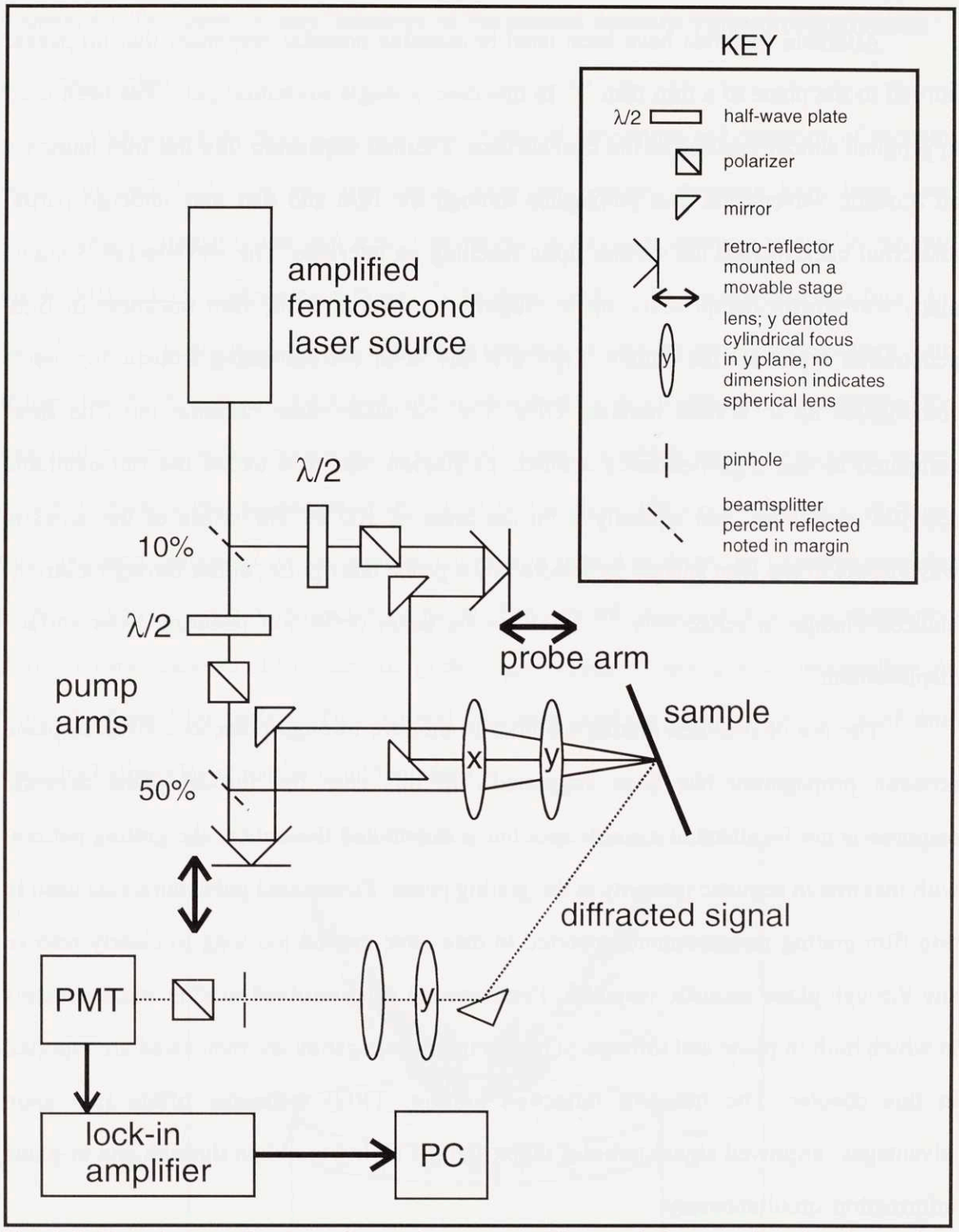

Fig. 3.3 Transient grating experimental apparatus. The y axis is normal to the plane of the page; the x axis is in the plane. The incident beam is separated, using a beamsplitter, into the pump (90%) and probe (10%) arms. The pump arm is further split by a 50% beamsplitter. The pump and probe beams are overlapped spatially and temporally at the sample.

schematically in figure 3.2. An amplified Ti:sapphire laser system producing 30-fs pulses (wavelength 800 nm, energy 10 μJ, repetition rate 1 KHz) was used. Two excitation pulses, each of ~5 μJ energy, were overlapped spatially and temporally at the sample surface at an angle of roughly 10°. The ~1 μJ probe pulse was variably delayed along a stepping-motorized delay line and focused at the excitation region, making an angle of ~2° to the film plane normal. The incident probe angle was chosen to maximize the diffraction efficiency, which falls off like $\cos\theta$ with deviation from normal incidence, while providing adequate spatial separation between the diffracted probe and the reflected pump and probe beams. The excitation pulses were polarized vertically (i.e., perpendicular to the grating wavevector) and the probe pulse horizontally, and the spot sizes were several hundred microns. The polarization of the probe pulse was chosen to maximize scattered pump rejection at the photodetector. A wavevector filter, consisting of a 10 cm focal length spherical lens with a pinhole (10-25 μm) in the front focal plane, was also used to prevent scattered light from reaching the detector. One of the excitation beams was synchronously chopped at half the laser repetition rate for phase-sensitive detection of the (horizontally polarized) diffracted signal. The signal was detected with a photomultiplier (PMT) tube whose output was averaged, amplified with a lock-in amplifier, digitized and then recorded on a PC for each mechanical delay line position, with typical delay line steps of 100-200 μm. A PMT was selected because of its high sensitivity, however an amplified photodiode provides similar sensitivity with considerably less noise, and was used exclusively in future experiments. A variably delayed probe pulse was used to detect responses on a picosecond time scale, with the total temporal range limited to less than 1 ns by the length of the mechanical delay line.

To monitor acoustic responses at longer times, a separate probe beam from a CW diode laser (λ=830 nm) was used. The diffracted signal from this probe beam was monitored in real time with a 1 GHz bandwidth photodiode and digital oscilloscope, yielding the entire slow part of the acoustic response with each excitation laser shot. The slow responses were averaged and recorded. Signals were recorded using these methods with diffraction efficiencies as low as 10^{-8}.

The apparatus was typically aligned using the electronic response from a titanium-nitride metal alloy film, because extremely high (several percent) changes in reflectivity were observed in these materials following short-pulse excitation. This resulted in diffraction efficiencies of 10^{-3} which produced signal beams which could be observed using an IR viewer. These bright beams could be easily aligned through the wavevector filter and into the detector; optimization of the optical apparatus was also simplified by these strong signals. A pump beam that had reflected off the titanium nitride sample was propagated over a distance of several meters and its position was carefully marked. The titanium nitride sample, which was held in a mount with two dimensional tilt control, was removed and the desired sample was loaded onto the mount. The mount was adjusted until the pump beam reflecting off the new sample returned to the previously marked spot, thereby ensuring correct alignment of the detector pinhole (see figure 3.2). It was also found to be extremely critical that stray light entering the detector be kept at an absolute minimum. In addition to the horizontal polarizer and the wavevector filter, this was typically achieved by draping a thick felt sheet from the PMT to the spherical lens of the wavevector filter and taping up all gaps in the felt.

III. Theory

The theoretical description of strain generation via impulsive light absorption in a transient grating experiment has been presented [3,9]. While this formalism yields the full description of acoustic responses in a film/substrate system, in the limit that the optical skin depth ζ of the metal film layer is much smaller than the transient grating fringe spacing Λ, it is more instructive to treat the generation of in-plane propagating surface acoustic waves (SAWs) and through-plane propagating longitudinal wavepackets separately. The SAWs are standing waves which give rise to modulation or "ripple" of the film surface, with the depth of modulation undergoing time-dependent oscillations at the standing-wave frequency. This frequency depends on the grating period as well as the film thickness and mechanical properties [3]. The longitudinal waves result in modulation of the film surface each time they return to the surface following partial reflection at an interface. The timing of the arrival of partial reflections at the surface is influenced by the film thickness and mechanical properties, but to first order not by the grating spacing. Both the SAW and longitudinal acoustic wavepacket responses may be monitored through diffraction of probe light.

In the limit $\zeta << \Lambda$, longitudinal wavepacket generation can be considered within a one-dimensional model [5]. The time and depth dependent strain is given by

$$\eta_{33}(z,t) = \frac{(1-R)Q\beta}{2\zeta C}\frac{1+\nu}{1-\nu}\left\{ e^{\frac{-z}{\zeta}} + \frac{1}{2}e^{\frac{-|z-v_l t|}{\zeta}}\,\mathrm{sgn}(z-v_l t)\right\} \tag{3.1}$$

where R is reflectivity, Q is pulse fluence, β is the thermal expansion coefficient, C is the specific heat per unit volume, ν is Poisson's ratio, and v_l is the longitudinal sound velocity in the film. The z coordinate is taken to be normal to the film plane, zero at the film surface, and increasing positively into the film. The first term describes the static strain (neglecting thermal diffusion) resulting from the density change due to the steady-

state temperature rise near the film surface. The second term describes the bipolar strain pulse propagating normal to the film plane with longitudinal acoustic velocity v_l which is caused by the density overshoot produced during impulsive heating.

Assuming no diffraction of the acoustic pulses, a z-propagating longitudinal wavepacket with an initial periodicity in the x-direction will retain this form, giving:

$$\eta_{33}(z,t,x) = \eta_{33}(z,t)\cos\left(\frac{2\pi x}{\Lambda}\right), \tag{3.2}$$

The diffraction of a variably delayed probe pulse off this periodic structure is used to interrogate $\eta_{33}(z,t)$ for z close to the film surface. The strain pulse causes diffraction of the probe through surface ripple, as discussed above, and also, in principle, via photoelastic coupling through which the acoustic response gives rise to spatially periodic changes in the sample reflectivity. The normalized diffracted signal intensity from the surface, assuming $\Lambda >> \lambda$, is given by the following expression:

$$\frac{I_d}{I_0} = \left| iRk_z h_0(t) + \frac{\delta R(t)}{2} \right|^2, \tag{3.3}$$

where k_z is the z component of the probe wavevector, $h_0(t)$ is the surface displacement, R is the complex reflectivity of the unstrained film and δR(t) is its strain-induced variation.

The two diffraction mechanisms have different dependencies on $\eta_{33}(z,t)$. The time-dependence of the diffracted signal from the "ripple" diffraction mechanism is given by ripple depth:

$$h_0(t) = \int_0^\infty \eta_{33}(z,t)dz \ . \tag{3.4}$$

To calculate the time-dependence of the signal from the photoelastic diffraction mechanism, finite probe light penetration depth into the sample must be considered. It

can be shown [5] that the change in the reflection coefficient for light incident on a film with z dependent strain is given by :

$$\delta R(t) \propto \int_0^\infty e^{i2k_z z - \frac{2z}{\zeta}} \frac{k_{23}\eta_{33}(z,t)dz}{4\varepsilon}, \tag{3.5}$$

where k_{23} is the complex photoelastic constant of the metal (see Appendix 3A for derivation).

IV. Results

Typical data from a nickel film are shown in Fig. 3.3. The solid curve in the main figure shows data at short times recorded with the femtosecond probe pulse and delay line, while the inset shows signal recorded with the cw probe at longer times. Focusing first on the solid curve in the main figure, two prominent dips at 75 and 153 ps, corresponding to the return of the longitudinal wavepacket to the surface following reflections from the film-substrate interface, are observed. The overlaid dashed line is a plot of surface displacement squared $|h_0(t)|^2$ as given by Eq. (3.4), while the raised dashed curve is a plot of $|\delta R(t)|^2$ as given by Eq. (3.5), in both cases with only the acoustic

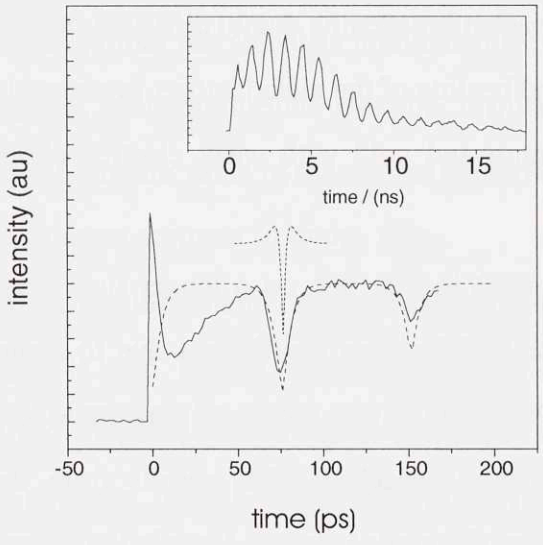

Fig. 3.2 Transient grating measurements of picosecond acoustic pulses in a 2500 Å nickel film. Dashed curves show calculated signals for "ripple" (overlaid curve) and photoelastic (raised curve) diffraction mechanisms. Nanosecond time scales presented in the inset show oscillations due to surface acoustic waves.

velocity and a multiplicative scaling factor as free parameters. The simulation does not consider the thermoreflectance contribution to the signal, resulting in disagreement with experiment at early times when the sample surface is at elevated temperature. Based upon the excellent agreement between the form of the experimental data and the simulation of $|h_0(t)|^2$, it is concluded that surface ripple is the dominant mechanism for signal generation. This is consistent with an analysis of Brillouin scattering mechanisms for Ni and Al [10]. It should be also mentioned that in transient reflectivity measurements on metal films such as Ni [5,7], acoustic pulses yield much smaller signals than the thermoreflectance response. In our experiment, acoustic pulse contributions are comparable to the dc component of the signal which, again, is consistent with simulations assuming the ripple diffraction mechanism. Note that the acoustic wavepacket duration in the simulations is not a free parameter but is determined from the optical penetration depth, i.e., by the depth into the film that was heated by the excitation pulses to initiate thermal expansion. Agreement between experiment and simulation shows that there is no significant acoustic wavepacket broadening due to diffusion of optically excited electrons prior to their relaxation and heating of the nickel lattice, in contrast to the results observed in metals such as aluminum and gold with weak electron-phonon coupling and high electron mobility [11,12].

As shown by the inset in Fig. 3.3, on a longer time scale the dynamics of the diffracted signal are dominated by slow oscillations due to counterpropagating SAWs. The SAW frequency of 980 MHz is two orders of magnitude lower than the frequency components of longitudinal wavepackets. This results from the fact that the SAW wavelength is determined by the grating period Λ while the characteristic wavelength of the longitudinal acoustic pulses is determined by the optical skin depth.

Fig. 3.4 shows examples of data taken from Al/TiW/Si multilayer film structures along with simulations assuming a surface ripple diffraction mechanism(see appendix 3B for simulation methodology). The simulations had to be run with several estimated

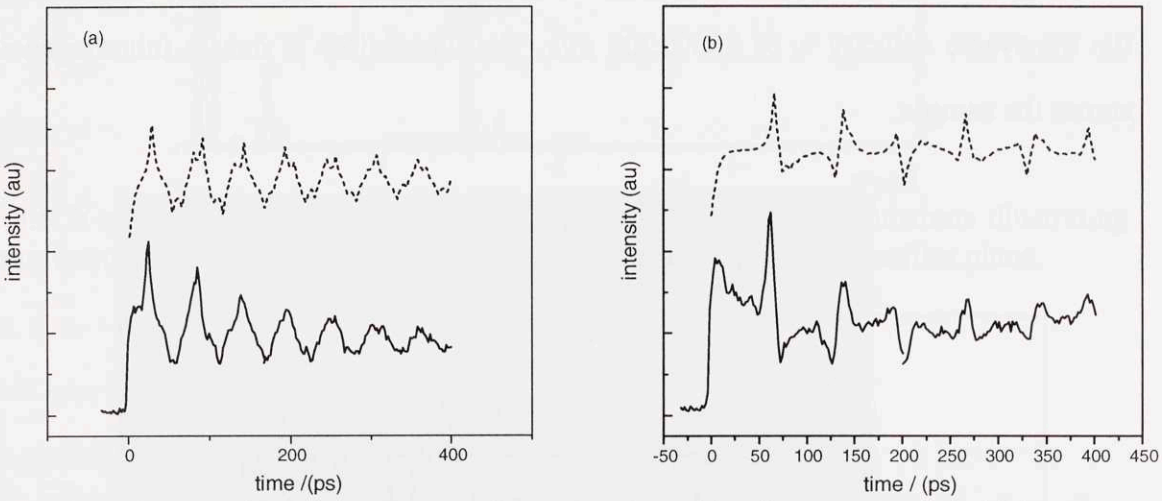

Fig. 3.4 Transient grating measurements from aluminum/titanium:tungsten multi-layer film structures. Experimental (solid) and simulated (dashed) acoustic response from (a) Al(1000 Å)/TiW(750 Å)/Si and (b) Al(2000 Å)/TiW(250 Å)/Si bi-layer films.

parameters since the layer thicknesses and mechanical properties of TiW layer were not known with a sufficient degree of accuracy. Reasonable agreement between measured and simulated data again indicates that the signal is dominated by the surface displacement contribution. Unlike nickel, non-equilibrium electron diffusion is not negligible in aluminum[11]. Therefore the literature value of the optical penetration depth was doubled in the simulation to provide a more accurate fit to the data.

An enhancement of the information content due to the ability to measure both longitudinal acoustic pulses and SAWs simultaneously is an important advantage compared to time-resolved transient reflectivity or deflection methods. To demonstrate this, we used the data obtained from a nickel film of 0.71 ± 0.04 μm thickness (as measured by scanning electron microscopy, see figure 3.5) on silicon ((001) surface) to determine both longitudinal and transverse acoustic velocities in the film. Short time TRG data from this sample were used to calculate a longitudinal acoustic velocity of

6100 ± 340 m/s. The SAW frequency measured from the nanosecond time-scale data was 795 MHz, yielding a SAW phase velocity of 3395 m/s. This value is determined by the elastic properties of the film and substrate and the film thickness. Using literature values for the elastic moduli of Si and the measured value of v_l, the SAW data yielded a value of the transverse velocity v_t of 3300±200 m/s. The uncertainty is due to inhomogeneities across the sample.

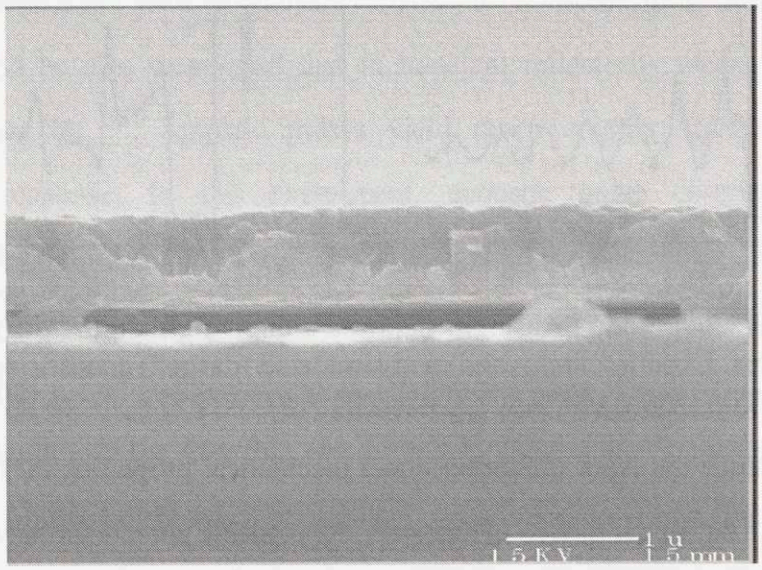

Fig. 3.5. SEM image of a nominally 1μm nickel film on a silicon substrate.

The measured velocities are not consistent with the literature values for polycrystalline nickel [14], v_l=5630 m/s, v_t=2960 m/s. To elucidate the reason for this inconsistency, we performed an X-ray diffraction analysis of the sample (see figure 3.6), which indicated a [111] preferential orientation of the nickel crystallites normal to the film plane. The longitudinal acoustic velocity along the [111] direction of crystalline nickel is 6240 m/s [14], consistent with experimental results. This illustrates the applicability of this technique for assessment of film morphology.

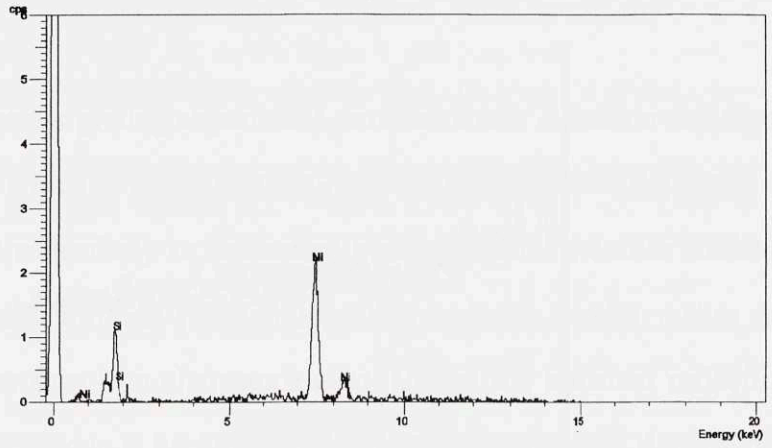

Fig. 3.6. X-ray diffraction analysis of a nickel film on a silicon (001) substrate illustrating the preferential [111] orientation of the nickel crystallites normal to the film plane.

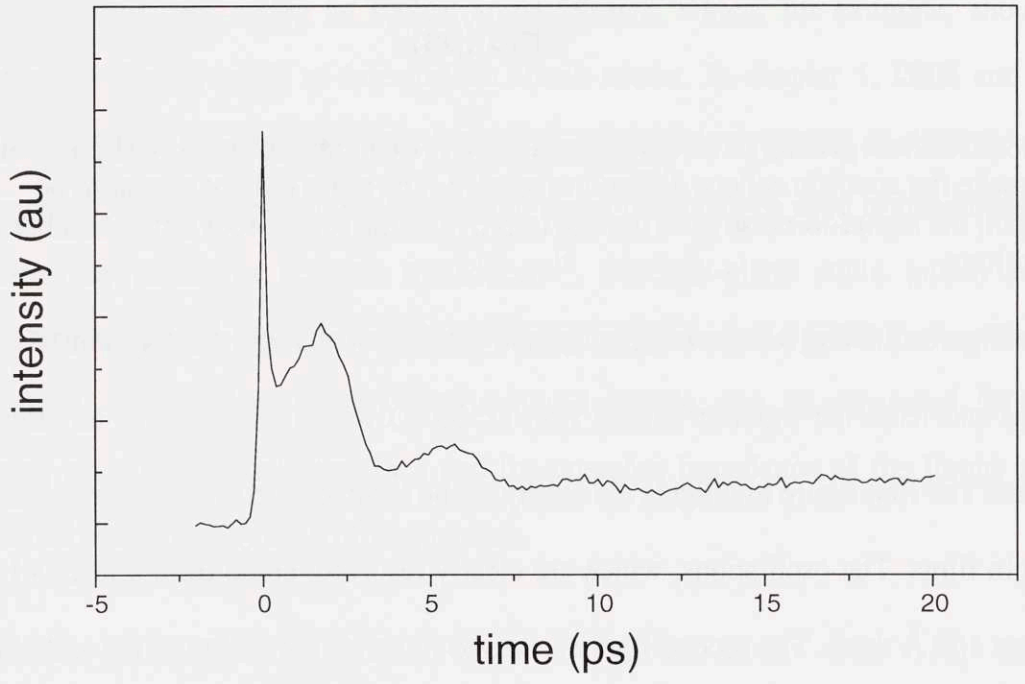

Fig. 3.7. Short time, ISTS data from nominal TiN(250 Å)/Ti(250 Å)/Al(1 mm)/TiN(500 Å) film on silicon substrate. The transient grating technique is seen to easily resolve oscillations from a sub-100 Å film.

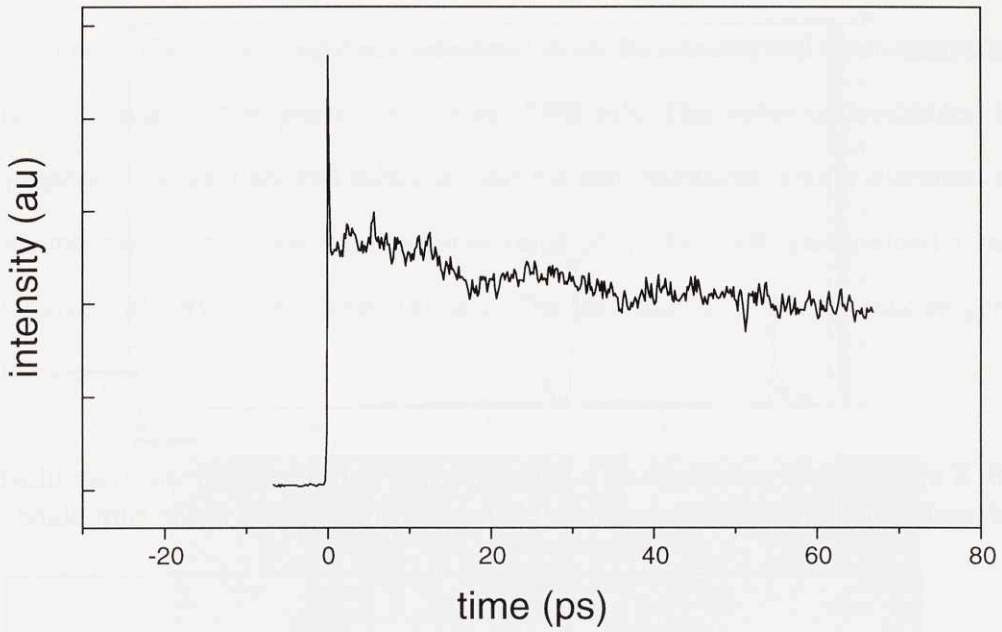

Fig. 3.8. Transient grating ISTS data from a 2500 Å titanium nitride film. High levels of noise make the acoustic echoes difficult to resolve. The noise did not appear to be Guassian; the signal-to-noise ratio did not improve as the square root of the number of acquisitions.

Figures 3.7 and 3.8 show signal from a TiN(250 Å)/Ti(250 Å)/Al(1 mm)/TiN(500 Å) film and from the titanium nitride film (2500 Å) which was used as an alignment standard. The first figure highlights the ability of the technique to monitor responses from very thin films. The oscillations, which are clearly resolved, come from a layer which is less than 100 Å thick. The second figure serves to illustrate the ability of the technique to measure weak acoustic reflections, but also to highlight a persistent noise problem which plagued experiments with this apparatus. The high levels of noise shown in fig. 3.8 were not reduced by extensive averaging. The reasons for this, and the solution to the problem, will be the subject of Chapter 4.

V. Conclusions

The transient grating experiment provides a new detection technique for ultrashort acoustic pulses which is based on time-resolved diffraction of the probe light in contrast to the transient reflectivity or deflection methods used in earlier studies. Sensitivity to both in plane and through plane propagating acoustic modes makes this technique a valuable tool for thin film characterization. Unlike the transient reflection or deflection methods, this technique is background-free in the sense that in the absence of excitation, there is no probe light incident on the detector. Consequently, the signal can be detected on a single-shot basis using an optical streak-camera, which, for example, should be advantageous for the study of laser-driven shock waves. In chapter 1, ISTS and ISBS were championed for their ability to measure relaxation dynamics in liquids, up to frequencies of roughly several gigahertz. Thin metal films can be used to overcome these limitations by acting as acoustic transducers[16]. Through-plane strain pulses contain signnificant bandwidth up to several hundred gigahertz. Acoustic pulses in free-standing metal films, brought into contact with a liquid sample, can be measured following reflection off a metal-liquid interface and the complex impedance of the liquid can be determined over a broad range of frequencies.

References

1. M.D. Fayer, IEEE J. Quant. Electron. **QE-22**, 1437 (1986).
2. T. Sawada and A. Harata, Appl. Phys. **A61**, 263(1995).
3. A.R. Duggal, J.A. Rogers and K.A. Nelson, J. Appl. Phys. **72**, 2823 (1992); J.A. Rogers, L. Dhar and K.A. Nelson, Appl. Phys. Lett. **65**, 312 (1994).
4. J. J. Kasinski, L. Gomez-Jahn, K. J. Leong, S. M. Gracewski, R. J. D. Miller, Opt. Lett. **13**, 710 (1988).
5. C. Thomsen, H. T. Grahn, H. J. Maris, and J. Tauc, Phys. Rev. B **34,** 4129 (1986).
6. H. T. Grahn, H. J. Maris, and J. Tauc, IEEE J. Quant. Electron. **25,** 2562 (1989).
7. O. B. Wright and K. Kawashima, Phys. Rev. Lett. **69,** 1668 (1992).

8. G.L. Eesley, B.M. Clemens and C.A. Paddock, Appl. Phys. Lett. **50**, 717 (1987).
9. Q. Shen, A. Harata, and T. Sawada, Jpn. J. Appl. Phys. **35**, 2339 (1996).
10. B. A. Auld, *Acoustic Fields and Waves in Solids; Vol. 1*, (John Wiley & Sons, Inc., New York, 1973).
11. R. Loudon, Phys. Rev. Lett. **40,** 581 (1978).
12. O. B. Wright, Phys. Rev. B **49**, 9985 (1994); V.E. Gusev and O.B. Wright, Phys. Rev. B **57**, 2878 (1998).
13. G. Tas and H.J. Maris, Phys. Rev. B **49**, 15046 (1994).
14. *Handbook of Physical Quantities*; *Vol. 1*, edited by I. S. Grigoriev and E. Z. Meilikhov (CRC Press, Boca Raton, 1995).
15. B. Ghebouli, A. Layadi, and L. Kerkache, Europ. Phys. J. Appl. Phys. **3**, 35 (1998).
16. G. Tas and H.J. Maris, Phys. Rev. B **55**, 1852 (1997).

Appendix 3A

First, consider the diffraction of a transverse magnetic (TM) plane wave from a sinusoidal, corrugated surface with a sinusoidal complex index of refraction modulation caused by a propagation strain pulse. The following treatment of diffraction from a thin grating follows closely that of Haus[1]. The surface is described by:

$$h(z,t) = h_0(t)\cos\left(\frac{2\pi x}{\Lambda}\right) \tag{A.1}$$

Where $h_0(t)$ is given by the integral of the strain pulse at $z=0$. The index of refraction variation is given by:

$$\Delta n(z,t,x) = \frac{\partial \eta}{\partial \eta_{33}}\eta_{33}(z,t)\cos\left(\frac{2\pi x}{\Lambda}\right) \tag{A.2}$$

$$\Delta \kappa(z,t,x) = \frac{\partial \kappa}{\partial \eta_{33}}\eta_{33}(z,t)\cos\left(\frac{2\pi x}{\Lambda}\right) \tag{A.3}$$

This can also be expressed as a complex dielectric constant:

$$\begin{aligned}\varepsilon &= (n+\Delta n+i\kappa+i\Delta\kappa)^2 \approx \varepsilon+(n+i\kappa)\Delta n+(in-\kappa)\Delta\kappa \\ &\equiv \varepsilon+\Delta\in\end{aligned} \tag{A.4}$$

This can be tied in with literature values of the photoelastic constant through the expression:

$$\Delta\in(z,t) = k_{23}\eta_{33}(z,t) \tag{A.5}$$

First, the change in the magnetic reflectivity of the film induced by the strain pulse must be considered. Ideally, an expression for magnetic reflectivity should be found to solve the diffraction problem, so the goal of this section is to find :

$$\Gamma_H(t) \equiv \frac{H_-^{(1)} + H_-^{(1')}}{H_+^{(1)}} \tag{A.6}$$

Begin with a three layer model which contains on air-metal interface and one metal-metal interface at depth z'. The strategy will be to determine the magnetic reflection coefficient

Begin with a three layer model which contains on air-metal interface and one metal-metal interface at depth z'. The strategy will be to determine the magnetic reflection coefficient for this problem and then to sum up and coherently add the reflections in an integral for each infinitesimal "interface" in the continuous strain pulse. The simple model is illustrated below in figure 3A.1:

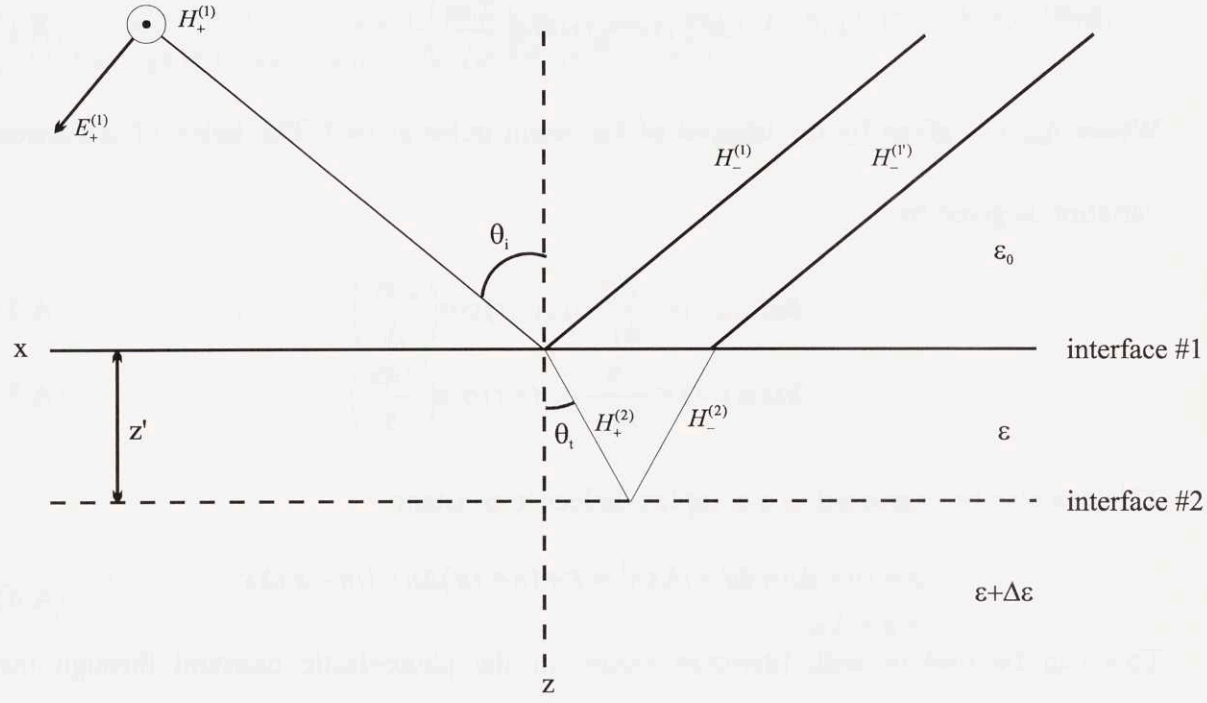

Fig. 3A.1: Model for the determination of the magnetic susceptibility of a metal film with an abrupt discontinuity in the dielectric constant at depth z'.

The reflection coefficient for a TM wave at the interface between materials with two different dielectric constants is well know. For interface #1 in the case under consideration:

$$\Gamma_H^{(1)} = \frac{Z_0^{(1)} - Z_0^{(2)}}{Z_0^{(1)} + Z_0^{(2)}} = \frac{\sqrt{1-\sin^2\theta_i} - \sqrt{1-\sin^2\theta_i \frac{\epsilon_0}{\epsilon}}\sqrt{\frac{\epsilon_0}{\epsilon}}}{\sqrt{1-\sin^2\theta_i} + \sqrt{1-\sin^2\theta_i \frac{\epsilon_0}{\epsilon}}\sqrt{\frac{\epsilon_0}{\epsilon}}} \qquad \text{(A.7)}$$

Now consider interface #2. The objective will be to find an expression similar to (A.7) and then linearize it with respect to $\Delta\in$ which is assumed to be small. The angle of the transmitted probe beam is given by Snell's law:

$$\theta_t = \sin^{-1}\left(\sqrt{\frac{\in_0}{\in}}\sin\theta_i\right) \tag{A.9}$$

The reflection coefficient can be written in terms of the z-component of the wavevector in medium 2:

$$\Gamma_H^{(2)} = \frac{\dfrac{k_z^{(1)}}{\in} - \dfrac{k_z^{(2)}}{\in+\Delta\in}}{\dfrac{k_z^{(1)}}{\in} + \dfrac{k_z^{(2)}}{\in+\Delta\in}} \tag{A.10}$$

where $\Gamma_H^{(2)} = \dfrac{H_-^{(2)}}{H_+^{(2)}}$. The wavevectors can be written in terms of the dielectric constant and the z-component of the frequency:

$$\left[k_z^{(1)}\right]^2 = \left(\omega_z^{(2)}\right)^2 \mu_0 \in \tag{A.11}$$

$$\left[k_z^{(2)}\right]^2 = \left(\omega_z^{(3)}\right)^2 \mu_0(\in+\Delta\in) \cong \left(\omega_z^{(2)}\right)^2 \mu_0(\in+\Delta\in) \tag{A.12}$$

$$k_z^{(1)} = \omega_z^{(2)}\sqrt{\mu_0 \in} \tag{A.13}$$

$$k_z^{(2)} = \omega_z^{(2)}\sqrt{\mu_0(\in+\Delta\in)} \cong \omega_z^{(2)}\sqrt{\mu_0 \in} + \frac{\omega_z^{(2)}\mu_0\Delta\in}{2\sqrt{\mu_0 \in}} \tag{A.14}$$

In (A.14), the second equality is correct to first order in $\Delta\in$. (A.10) can now be written :

$$\Gamma_H^{(2)} = \frac{\dfrac{\omega_z^{(2)}\sqrt{\mu_0 \in}}{\varepsilon} - \dfrac{\omega_z^{(2)}\sqrt{\mu_0 \in}}{\in+\Delta\in} - \dfrac{\omega_z^{(2)}\mu_0\Delta\in}{2\sqrt{\mu_0 \in}(\in+\Delta\in)}}{\dfrac{\omega_z^{(2)}\sqrt{\mu_0 \in}}{\in} + \dfrac{\omega_z^{(2)}\sqrt{\mu_0 \in}}{(\in+\Delta\in)} + \dfrac{\omega_z^{(2)}\mu_0\Delta\in}{2\sqrt{\mu_0 \in}(\in+\Delta\in)}} \tag{A.15}$$

$$\Gamma_H^{(2)} = \frac{\omega_z^{(2)}\mu_0 \in(\in+\Delta\in)\left[2(\in+\Delta\in) - 2\in-\Delta\in\right]}{\omega_z^{(2)}\mu_0 \in(\in+\Delta\in)\left[2(\in+\Delta\in) + 2\in+\Delta\in\right]} \tag{A.16}$$

$$\Gamma_H^{(2)} = \frac{2\in+2\Delta\in-2\in-\Delta\in}{2\in+2\Delta\in+2\in+\Delta\in} = \frac{\Delta\in}{4\in+3\Delta\in} \tag{A.17}$$

$$\Gamma_H^{(2)} = \frac{\omega_z^{(2)}\mu_0 \in (\in +\Delta\in)\left[2(\in +\Delta\in) - 2\in -\Delta\in\right]}{\omega_z^{(2)}\mu_0 \in (\in +\Delta\in)\left[2(\in +\Delta\in) + 2\in +\Delta\in\right]} \tag{A.16}$$

$$\Gamma_H^{(2)} = \frac{2\in +2\Delta\in -2\in -\Delta\in}{2\in +2\Delta\in +2\in +\Delta\in} = \frac{\Delta\in}{4\in +3\Delta\in} \tag{A.17}$$

which is, again correct to first order in $\Delta\in$. The final magnetic reflection coefficient that is desired from the simple case is $\Gamma_H^{(2')} = \frac{H_-^{(1')}}{H_+^{(1)}}$. This can be found by determining the transmission coefficient across interface #1 from both directions and by adding a phase term and a damping term to account for the propagation of the light:

$$\Gamma_H^{(2')} = \frac{\omega_z \mu_0 \Delta\in}{4k_z^{(1)}\sqrt{\mu_0 \in}} \exp(-\zeta z')\exp(i2z'k_z^{(2)})\sqrt{1-\left(\Gamma_H^{(1)}\right)^2}\sqrt{1-\left(\tilde{\Gamma}_H^{(1)}\right)^2} \tag{A.18}$$

where $\tilde{\Gamma}_H^{(1)}$ is given by (A.7) with θ_t replacing θ_i and swapping ε_0 with ε and vice versus. In the more general case, $\Delta\in$ is a function of space (and time), in which case (A.18) can be written :

$$\Gamma_H^{(2')}(t,x) = \sqrt{1-\left(\Gamma_H^{(1)}\right)^2}\sqrt{1-\left(\tilde{\Gamma}_H^{(1)}\right)^2}\int_0^\infty \frac{\omega_z \mu_0 \Delta\in(z,t,x)}{4k_z^{(1)}\sqrt{\mu_0 \in}} \exp(-\zeta z')\exp(i2z'k_z^{(2)})dz' \tag{A.19}$$

It is assumed in this integration that the light is sampling the strain at a single point in the x dimension because of the small incident angle. The magnetic field produced by reflection from the strain pulse is then given by:

$$H_-^{(1')} = \Gamma_H^{(2)}(t)H_+^{(1)} \tag{A.20}$$

Now the complete reflected field is given by:

$$H_-^{(1)} + H_-^{(1')} = \left[\Gamma_H^{(1)} + \Gamma_H^{(2)}(t)\right]H_+^{(1)} \tag{A.21}$$

From (A.6), we now have the final result:

$$\Gamma_H(t) = \Gamma_H^{(1)} + \Gamma_H^{(2)}(t) \tag{A.22}$$

When the acoustic pulse is generated with crossed excitation pulses, the temporal and spatial dependence of the magnetic reflectivity is given by:

$$\Gamma_H(x,t) = \Gamma_H(t)\cos\left(\frac{2\pi x}{\Lambda}\right) \tag{A.23}$$

With this, the diffraction caused by the acoustic pulse can be determined. The input field can be described:

$$\vec{H} = \hat{y}H_i e^{\left[-(ik_{ix}x + ik_{iz}z)\right]} \tag{A.24}$$

The boundary conditions impose the following conditions:

$$H_i e^{\left[-(ik_{ix}x + ik_{iz}z)\right]}\Big|_{z=h(x)} + H_R(x,z)\Big|_{z=h(x)} = 0 \tag{A.25}$$

The first term on the left is the field generated by the input field at the corrugated surface of the film. The second term is the reflected field which must cancel the input field at the film surface. The strategy will be to used this condition to find the reflected field. It will be seen that the following expansion can be used to describe the reflected field:

$$H_R(x,z) = e^{-ik_{ix}x}\sum_{m=0}^{\infty} R_m e^{ik_{Rz}^{(m)}z} e^{\frac{-i2\pi mx}{\Lambda}} \tag{A.26}$$

To begin with, the corrugation and the x dependence of the reflectivity will be ignored. The incident plus reflected field is given by:

$$H = H_i e^{-ik_{ix}x}\left[e^{-ik_{iz}z} - \Gamma_H(t)e^{ik_{iz}z}\right] \tag{A.27}$$

The incident plus reflected field at the corrugated surface will now be considered, including the spatial dependence of the reflectivity:

$$H(z=h(x))=H_i e^{-ik_{ix}x}\left[e^{-ik_{iz}h_0(t)\cos\left(\frac{2\pi x}{\Lambda}\right)}-\Gamma_H(t)\cos\left(\frac{2\pi x}{\Lambda}\right)e^{ik_{iz}h_0(t)\cos\left(\frac{2\pi x}{\Lambda}\right)}\right] \quad \text{(A.28)}$$

This can be expanded around $h_0(t)=0$:

note:

$$e^{-iax}\cong e^{-iax}\Big|_0-iae^{-iax}\Big|_0 x=1-iax$$

$$H=H_i e^{-ik_{ix}x}\left[1-ik_{iz}h_0(t)\cos\left(\frac{2\pi x}{\Lambda}\right)-\Gamma_H(t)\cos\left(\frac{2\pi x}{\Lambda}\right)-ik_{iz}h_0(t)\Gamma_H(t)\cos^2\left(\frac{2\pi x}{\Lambda}\right)\right] \quad \text{(A.29)}$$

note:

$$\cos(2\theta)=2\cos^2\theta-1$$

which simplifies to:

$$H=H_i e^{-ik_{ix}x}\left\{1-\frac{ik_{iz}h_0(t)\Gamma_H(t)}{2}-\left[\ ik_{iz}h_0(t)+\Gamma_H(t)\ \right]\cos\left(\frac{2\pi x}{\Lambda}\right)-\frac{ik_{iz}h_0(t)\Gamma_H(t)}{2}\cos\left(\frac{4\pi x}{\Lambda}\right)\right\} \quad \text{(A.30)}$$

which can be expanded to:

$$H=H_i e^{-ik_{ix}x}\left\{1-\frac{ik_{iz}h_0(t)\Gamma_H(t)}{2}-\frac{\left[ik_{iz}h_0(t)+\Gamma_H(t)\right]}{2}\left[e^{\frac{i2\pi x}{\Lambda}}+e^{\frac{-i2\pi x}{\Lambda}}\right]-\frac{ik_{iz}h_0(t)\Gamma_H(t)}{4}\left[e^{\frac{i4\pi x}{\Lambda}}+e^{\frac{-i4\pi x}{\Lambda}}\right]\right\} \quad \text{(A.31)}$$

This entire field must be canceled by higher order diffraction. We are only interested in first order diffraction, so combining (A.31) and (A.26) and neglecting all but the first order terms gives the following expression:

$$-H_i e^{-ik_{ix}x}\frac{\left[ik_{iz}h_0(t)+\Gamma_H(t)\right]}{2}\left[e^{\frac{i2\pi x}{\Lambda}}+e^{\frac{-i2\pi x}{\Lambda}}\right]+R_1 e^{\frac{-i2\pi x}{\Lambda}}e^{-ik_{ix}x}+R_{-1}e^{\frac{i2\pi x}{\Lambda}}e^{-ik_{ix}x}=0 \quad \text{(A.32)}$$

From this, it immediately follows that:

$$R_1 = R_{-1} = \frac{H_i\left[ik_{iz}h_0(t) + \Gamma_H(t)\right]}{2} \tag{A.33}$$

The final magnetic field can be written:

$$H_R^{(1)} = \hat{y}e^{-ik_{ix}x}e^{ik_{Rz}^{(1)}z}e^{\frac{-i2\pi x}{\Lambda}}e^{i\omega t}\frac{\left(ik_{iz}h_0(t) + \Gamma_H(t)\right)}{2} \tag{A.34}$$

The electric field can be found from Maxwell's equations:

$$\vec{\nabla} \times \vec{H} = i\omega \in \vec{E} \tag{A.35}$$

$$\vec{\nabla} \times \hat{y}H_y = -\hat{x}\frac{\partial}{\partial z}H_y + \hat{y}\frac{\partial}{\partial x}H_y \tag{A.36}$$

$$\vec{E} = \frac{1}{i\omega \in}\left(ik_{Rz}^{(1)}\hat{x} - ik_{ix}\hat{z} - \frac{i2\pi z}{\Lambda}\right)H_y = \left(\frac{k_{Rz}^{(1)}\hat{x}}{\omega \in} - \frac{k_{ix}\hat{z}}{\omega \in} - \frac{2\pi\hat{z}}{\omega \in \Lambda}\right)H_y \tag{A.37}$$

The measured intensity is given as:

$$I = |E|^2 = \left(\frac{k_{Rz}^{(1)}\hat{x}}{\omega \in} - \frac{k_{ix}\hat{z}}{\omega \in} - \frac{2\pi\hat{z}}{\omega \in \Lambda}\right)^2 \frac{\left|ik_{iz}h_0(t) + \Gamma_H(t)\right|^2}{4} \tag{A.38}$$

or, alternatively :

$$I = |E|^2 = \left(\frac{k_{Rz}^{(1)}\hat{x}}{\omega \in} - \frac{k_{ix}\hat{z}}{\omega \in} - \frac{2\pi\hat{z}}{\omega \in \Lambda}\right)^2 \frac{\left(k_{iz}\right)^2 h_0^2(t) + \left|\Gamma_H(t)\right|^2 + 2k_{iz}h_0(t)\text{imag}\left(\Gamma_H(t)\right)}{4} \tag{A.39}$$

References

[1]H. A. Haus, *Waves and Fields in Optoeletronics* (Prentice-Hall, Inc., Englewood Cliffs, 1984).

Appendix 3B: Multilayer film ISTS data simulation

Following absorption of a short pulse by an opaque material, the time and depth dependent strain profile is given by[1]:

$$\begin{aligned} \eta_{33}(z,t) &= \exp\left(\frac{z_0 - vt}{\xi}\right) && \text{for } 0 < z_0 \le vt \\ &= \exp\left(\frac{-(z_0 - vt)}{\xi}\right) && \text{for } vt < z_0 < \infty \end{aligned} \tag{B.1}$$

where v is the acoustic velocity and ξ is the penetration depth of the hot electrons in the material. The time and depth dependent displacement is given by the integral of the strain:

$$\begin{aligned} u(z,t) &= \int_{-\infty}^{z} \exp\left(\frac{z_0 - vt}{\xi}\right) dz_0 && \text{for } 0 < z \le vt \\ &= \int_{-\infty}^{vt} \exp\left(\frac{z_0 - vt}{\xi}\right) dz_0 + \int_{vt}^{z} \exp\left(\frac{-(z_0 - vt)}{\xi}\right) dz_0 && \text{for } vt < z < \infty \end{aligned} \tag{B.2}$$

This simplifies to:

$$\begin{aligned} u(z,t) &= \xi \exp\left(\frac{z_0 - vt}{\xi}\right) && \text{for } 0 < z \le vt \\ &= \xi \exp\left(\frac{-(z_0 - vt)}{\xi}\right) && \text{for } vt < z < \infty \end{aligned} \tag{B.3}$$

In order to determine the contributions to the time dependent response of the surface displacement from acoustic pulses which have undergone partial reflections from interfaces and returned to the surface, the film structure will be modeled as depicted in figure 3B.1.

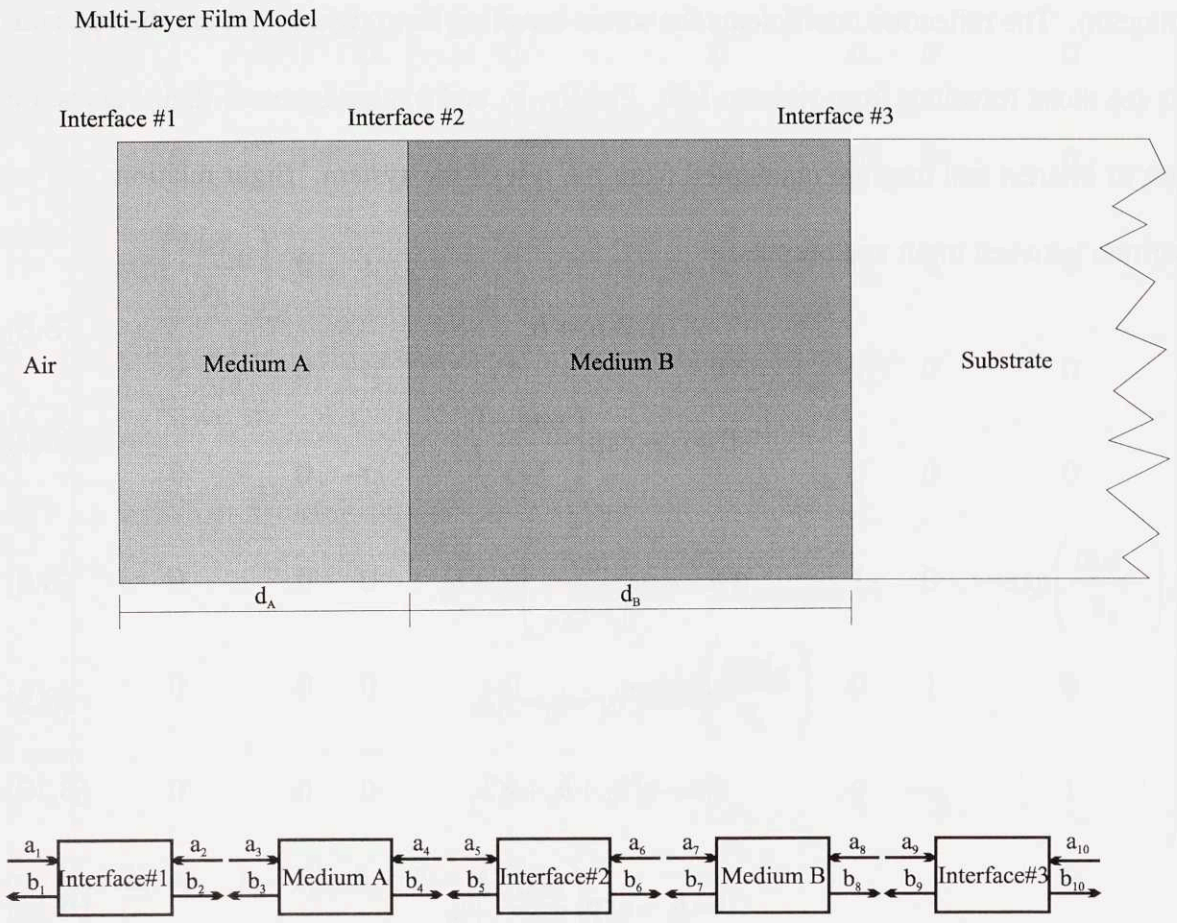

Figure 3B.1: A model for a multi-layer film structure.

Each interface and film will be treated as a four port terminal. Assuming that $\zeta << d_A$, the surface displacement pulse given by (B.3) can be fourier decomposed into plane waves:

$$u(\omega) = \frac{1}{\sqrt{2\pi}} \int_{-\infty}^{\infty} u(t) e^{i\omega t} dt \tag{B.4}$$

These $u(\omega)$ will be taken as the inputs to the model, i.e.,

$$a_1 = u(\omega) \tag{B.5}$$

The desired outputs will be b_2 and b_3. It will be assumed that t_1=1, r_1=-1 and that the reflection coefficients are for waves propagating from left to right in the above

diagram. The reflection coefficients for waves traveling from right to left are the opposite as for those traveling from right to left. Finally, b_1 and b_{10} are ignored; their values are not of interest and they are uncoupled from the rest of the system. Eight relations can be written between input and outputs:

$$a_1 = b_2 + b_3 \tag{B.6}$$

$$0 = b_3 - \exp\left(\frac{i\omega d_A}{v_A}\right) b_5 \tag{B.7}$$

$$0 = -\exp\left(\frac{i\omega d_A}{v_A}\right) b_2 + b_4 \tag{B.8}$$

$$0 = -r_2^f b_4 + b_5 - t_2^r b_7 \tag{B.9}$$

$$0 = -t_2^f b_4 + b_6 + r_2^r b_7 \tag{B.10}$$

$$0 = b_7 - \exp\left(\frac{i\omega d_B}{v_B}\right) b_9 \tag{B.11}$$

$$0 = -\exp\left(\frac{i\omega d_B}{v_B}\right) b_6 + b_8 \tag{B.12}$$

$$0 = -r_3 b_8 + b_9 \tag{B.13}$$

where r_n and t_n are the reflection and transmission coefficient for the nth interface and the f superscript on the reflection and transmission coefficients for the second interface denote that the coefficient if for a wave propagating from left to right in figure 3B.1 (forward), while the r superscript identifies the coefficient for waves traveling from right to left (reverse). Defining several matrices:

$$\hat{M} = \begin{pmatrix} 1 & 1 & 0 & 0 & 0 & 0 & 0 & 0 \\ 0 & 1 & 0 & -\exp\left(\frac{i\omega d_A}{v_A}\right) & 0 & 0 & 0 & 0 \\ -\exp\left(\frac{i\omega d_A}{v_A}\right) & 0 & 1 & 0 & 0 & 0 & 0 & 0 \\ 0 & 0 & -r_2^f & 1 & 0 & -t_2^r & 0 & 0 \\ 0 & 0 & -t_2^f & 0 & 1 & r_2^r & 0 & 0 \\ 0 & 0 & 0 & 0 & 0 & 1 & 0 & -\exp\left(\frac{i\omega d_B}{v_B}\right) \\ 0 & 0 & 0 & 0 & -\exp\left(\frac{i\omega d_B}{v_A}\right) & 0 & 1 & 0 \\ 0 & 0 & 0 & 0 & 0 & 0 & -r_3 & 1 \end{pmatrix}$$

$$\hat{b} = \begin{pmatrix} b_2 & b_3 & b_4 & b_5 & b_6 & b_7 & b_8 & b_9 \end{pmatrix}^{-1}$$

$$\hat{a} = \begin{pmatrix} a_1 & 0 & 0 & 0 & 0 & 0 & 0 & 0 \end{pmatrix}^{-1}$$

the eight expressions (B.6) to (B.13) can be recast in to a matrix form:

$$\hat{M}\hat{b} = \hat{a} \tag{B.14}$$

and $\hat{M}$ can be inverted to solve for b_2 and b_3 which will yield the contribution to the surface displacement from partially reflected waves which have returned to the surface:

$$b_1 = \frac{-a_1\left[r_3 r_2^r \exp\left(\frac{i2\omega d_B}{v_B}\right) - 1\right]}{C\exp\left[i2\omega\left(\frac{d_A}{v_A} + \frac{d_B}{v_B}\right)\right] + r_2^f \exp\left(\frac{i2\omega d_A}{v_A}\right) + r_2^r r_3 \exp\left(\frac{i2\omega d_B}{v_B}\right) - 1} \tag{B.15}$$

$$b_2 = \frac{-a_1 \exp\left(\frac{i2\omega d_A}{v_A}\right)\left[\left(r_2^f r_2^r r_3 - t_2^f t_2^r r_3\right)\exp\left(\frac{i2\omega d_B}{v_B}\right) - r_2\right]}{C\exp\left[i2\omega\left(\frac{d_A}{v_A}+\frac{d_B}{v_B}\right)\right] - r_2^f \exp\left(\frac{i2\omega d_A}{v_A}\right) - r_2^r r_3 \exp\left(\frac{i2\omega d_B}{v_B}\right) + 1} \tag{B.16}$$

where $C = r_2^f r_2^r r_3 + t_2^f t_2^r r_3$.

Finally, the values of the reflection and transmission coefficients must be determined. Consider two materials A and B with acoustic velocities v_A and v_B and densities ρ_A and ρ_B. Let there be a displacement wave source in material A. The displacement in A can be written as:

$$u_A = u\left(t - \frac{z}{v_A}\right) + ru\left(t + \frac{z}{v_A}\right) \tag{B.17}$$

while the displacement in B is given by:

$$u_B = tu\left(t - \frac{z}{v_B}\right) \tag{B.18}$$

where r and t are the reflection and transmission coefficients of the interface and u is a function which describes the displacement wave. The boundary conditions at the interface require continuity of displacement and stress[2]. The stress is related to the displacement by the expression:

$$\sigma_{33} = \rho \int \frac{\partial^2 u}{\partial t^2} dz \tag{B.19}$$

Let:

$$\xi = t - \frac{z}{v_A}$$
$$\xi' = t + \frac{z}{v_A} \tag{B.20}$$

The time and space derivatives of the displacement can be related by:

$$\frac{\partial u}{\partial t}=\frac{\partial u}{\partial \xi}\frac{\partial \xi}{\partial t}=\frac{\partial u}{\partial \xi}\Rightarrow\frac{\partial^2 u}{\partial t^2}=\frac{\partial^2 u}{\partial \xi^2} \tag{B.21}$$

and similarly:

$$\frac{\partial^2 u}{\partial t^2}=\frac{\partial^2 u}{\partial \xi'^2} \tag{B.22}$$

Also note that:

$$\begin{aligned} d\xi &= \frac{-1}{v_A}dx \\ d\xi' &= \frac{1}{v_A}dx \end{aligned} \tag{B.23}$$

Equation (B.19) can be written for the stress in material A:

$$\begin{aligned} \sigma_{33}^{A} &= -v_A\rho_A\int\frac{\partial^2 u(\xi)}{\partial^2 \xi}d\xi + rv_A\rho_A\int\frac{\partial^2 u(\xi')}{\partial^2 \xi'}d\xi' \\ &= -v_A\rho_A\frac{\partial u\left(t-\frac{z}{v_A}\right)}{\partial t}+rv_A\rho_A\frac{\partial u\left(t+\frac{z}{v_A}\right)}{\partial t} \end{aligned} \tag{B.24}$$

and for material B:

$$\sigma_{33}^{B}=-tv_B\rho_B\frac{\partial u\left(t-\frac{z}{v_A}\right)}{\partial t} \tag{B.25}$$

The boundary conditions require that (B.24) and (B.25) be equal at the interface (z=0). This implies that:

$$-v_A\rho_A+rv_A\rho_A=-v_B\rho_B t \tag{B.26}$$

Continuity of displacement requires that:

$$u\left(t-\frac{z}{v_A}\right)+ru\left(t+\frac{z}{v_A}\right)u\left(t-\frac{z}{v_A}\right)+ru\left(t+\frac{z}{v_A}\right)\Bigg|_{z=0}=tu\left(t+\frac{z}{v_B}\right)\Bigg|_{z=0} \tag{B.27}$$

which simplifies to:

$$t=r+1 \tag{B.28}$$

Combining (B.26) and (B.28) yields the reflection and transmission coefficients:

$$r=\frac{v_A\rho_A-v_B\rho_B}{v_A\rho_A+v_B\rho_B} \tag{B.29}$$

$$t=\frac{v_A\rho_A}{v_A\rho_A+v_B\rho_B} \tag{B.30}$$

The simulation approach is as follows. First, the penetration depth of the hot electrons is estimated to be equal to the optical penetration depth, which can be determined from the literature values of the imaginary part of the index of refraction of the materials at 800nm. The values for the acoustic velocities of pure metals were also taken directly from literature; values for alloys were estimated. The ISTS simulations were written as Matlab m-files and example code for an Al/TiW bilayer film mounted on a silicon substrate is presented in Appendix 3C. This is the code that was used to generate the simulation results in figure 3.4b. The first 29 lines of the program are used to generate properly spaced time arrays and to input the physical parameters of the film structure in the indicated units. Line 33-39 determine the forward and reverse reflection and transmission coefficients according to (B.29) and (B.30).

The displacement pulse represented by (B.3) is defined in lines 43-45. The form of the expression differs somewhat in the program because a quasi-static contribution to displacement from the thermal expansion of the film is included in the code to facilitate comparison between the simulation and the experimental results. In lines 50-57, the input

displacement pulse is fourier decomposed into plane waves. Lines 61-69 compute the *b1* and *b2* coefficients as described by (B.15) and (B.16). Lines 74-78 sum up the two coefficients and take the inverse fourier transform. This result is squared to determine the ISTS signal which is proportional to the square of the displacement as shown in Appendix 3A and the results are plotted.

It should be noted that the units on these plots, while in angstroms, do not represent the actual value of the film displacement because the simulation does not take into consideration the magnitude of the initial displacement caused by impulsive heating. This simply means that the results from these simulations are correct to within a scaling factor. Additionally, it should be noted that this was not the simulation approach which was used to calculate the shape of the reflectivity signal for nickel in figure 3.3. The program used to perform these simulations, also written as an m-file, computed the strain as a function of time and depth. Because this approach required much larger matrices to be stored, it was rejected in favor of the surface displacement treatment for general use. However, the treatment was quite similar to that presented above with minor modifications.

References

1 C. Thomsen, H. T. Grahn, H. J. Maris, and J. Tauc, Phys. Rev. B **34,** 4129-4138 (1986).

2 L. D. Landau and E. M. Lifshits, *Theory of Elasticity* (Permgamon Press; Addison-Wesley Pub. Co., London, Reading, Mass., 1959).

Appendix 3C: Matlab code for ISTS multi-layer film simulations in m-file format

```
clear M pulse b1 kA z t I signal;

%create the time row vector

tmin=-4095;  %minimum temporal extreme in ps
tmax=4096;   %maximum temporal extreme in ps
tstep=1;     %time steps in ps
ta1=tmin:tstep:0; %create time vector:units=ps
ta2=1:tstep:tmax;

%define constants and physical parameters

lamda=8000;  %wavelength of light in ang
kappa=4;  %imaginary part of the index of refraction of the
%top layer
si=lamda/(kappa*2*pi);   %1/e distance of the initial strain
%pulse
vA=6.260e3;  %acoustic velocity in dispersionless medium
%A:units=m/s
vA=vA/100;   %convert acoustic velocity to ang/ps
dA=2000;  %depth of layer A: units=angstroms
densityA=2.70; %density of medium A in g/cc
ZA=densityA*vA;   %acoustic impedance of medium A in
%g*ang/cm*ps
vB=6e3; %acoustic velocity in dispersionless medium
%B:units=m/s
vB=vB/100;     %convert acoustic velocity to ang/ps
dB=250; %depth of layer B: units=angstroms
densityB=15; %density of medium B in g/cc
ZB=densityB*vB;   %acoustic impedance of medium B in
%g*ang/cm*ps
vS=8.43e3;     %acoustic velocity in substrate:units=m/s
vS=vS/100;   %convert acoustic velocity units to ang/ps
densityS=2.42; %density of substrate in g/cm
ZS=densityS*vA;   %acoustic impedance of substrate in
%g*ang/cm*ps

%determine reflection and transmission coefficients for
displacement pulse

r1t=1;  %frequency independent reflection coefficient for
%interface 1
r2=(ZA-ZB)/(ZA+ZB); %frequency independent reflection
%coefficient for interface 2 (forward)
t2=1+r2;  %frequency independent transmission coefficient
%for interface 2 (forward)
r2t=(ZB-ZA)/(ZA+ZB);     %frequency independent reflection
%coefficient for interface 2 (reverse)
```

```
t2t=1+r2t;  %frequency independent transmission coefficient
%for interface 2 (reverse)
r3=(ZB-ZS)/(ZB+ZS); %frequency independent reflection
%coefficient for interface 3
t3=1+r3;  %frequency independent transmission coefficient
%for interface 3
%create displacement pulse vector:units=surface displacement
as a function of time in angstroms

pulse2=si-si*exp(-(vA.*ta2)/si)./2;
pulse1=si-si*exp((vA.*ta1)/si)./2;
pulse=cat(2,pulse1,pulse2);
t=cat(2,ta1,ta2);
tsize=size(t);

%take the temporal fourier transform of the surface
%displacement

pulse=fftshift(pulse);
pulse=fft(pulse);
pulse=fftshift(pulse);

%calculate the frequency row vector:units=1/ps=GHz

omega=-tsize(2)/2:tsize(2)/2-1;
omega=2*pi*omega/(tsize(2)*tstep);

%define the relevant output row vectors b1 and b2

term1=-pulse.*(r3*r2t*exp(i*2*omega*dB/vB)-1);
term2=-
r1t*exp(i*2*omega*dA/vA).*r3.*t2t.*exp(i*2*omega*dB/vB)*t2+r
1t*exp(i*2*omega*dA/vA).*r3.*r2t.*r2.*exp(i*2*omega*dB/vB);
term3=-r2*exp(i*2*omega*dA/vA)*r1t-
r3*r2t*exp(i*2*omega*dB/vB)+1;
b1=term1./(term2+term3);
term1=pulse.*(-1).*(-
r3*t2t*exp(i*2*omega*dB/vB)*t2+r3*r2t*r2*exp(i*2*omega*dB/vB
)-r2).*exp(i*2*omega*dA/vA);
term2=-
r1t*exp(i*2*omega*dA/vA).*r3.*t2t.*exp(i*2*omega*dB/vB)*t2+r
1t*exp(i*2*omega*dA/vA).*r3.*r2t.*r2.*exp(i*2*omega*dB/vB);
term3=-r2*exp(i*2*omega*dA/vA)*r1t-
r3*r2t*exp(i*2*omega*dB/vB)+1;
pulse=term1./(term2+term3);
clear term1 term2 term3;

%calculate inverse fourier transform of pulse+b1 to
%determine the time dependent
```

```
%surafce displacement following interaction with the
%interfaces

b1=fftshift(b1+pulse);
b1=ifft(b1);
pulse=fftshift(b1);
pulse=pulse(tsize(2)/2:tsize(2));
t=t(tsize(2)/2:tsize(2));

%compute ISTS signal
signal=abs(pulse).^2;

figure(1);plot(t,signal);
axis([-50 500 0 real(max(signal))+real(max(signal))*.5])
```

Chapter 4. Heterodyne Detection of Transient Gratings on a Femtosecond Timescale

I. Introduction

As mentioned at the end of chapter III and illustrated in figure 3.8, the noise in much of the transient grating ISTS data taken from metal films appeared to be highly non-Gaussian. It was clear from many experiments performed at this time that averaging n scans did not produce a signal-to-noise ratio improvement of $\sqrt{n}$, especially in samples of poor optical quality. It was hypothesized at that time that unstable phase control between the two pump beams in the optical apparatus depicted in figure 3.2 was responsible for this non-Gaussian noise profile. The two pump beams were propagated separately over distances of hundreds of centimeters and through and off of several optics before being recombined at the sample. Because no active stabilization was incorporated into the experimental apparatus, the optical path length traveled by the two beams was certainly not constant to within a fraction of the 800 nm wavelength of the light. This instability in optical paths resulted in an instability in the phase difference between the two pulses when they were recombined at the sample, and this resulted in an instability in the spatial phase of the transient grating produced by the sample's spatially periodic response. The phase of the portion of the probe field which diffracts off this transient grating is a function of the grating spatial phase, and consequently the temporal phase of the signal was also unstable.

The unstable grating phase, combined with excessive parasitic scattering, could lead to non-Gaussian noise. For all of the metal films studied, the ratio of the diffracted signal intensity to the intensity of parasitically scattered light was extremely low. Even following spatial filtering, wavevector filtering, and polarization filtering, the intensity of

parasitically scattered light, especially from the probe beam which could not be polarization filtered, was high compared with the intensity of the diffracted signal beam. Consequently, the electric fieled at the photodetector had contributions from multiple sources:

$$E_{total} = E_{scattered}^{pump} e^{i\varphi_{scattered}^{pump}} + E_{scattered}^{probe} e^{i\varphi_{scattered}^{probe}} + E_{diffracted} e^{i\varphi_{diffracted}} \quad (4.1)$$

All of these contributions interfere at the detector, which measures the intensity of the total field. Recalling that all of the pulses are extremely short in duration and that the experiments are carried out by repeatedly measuring the intensity of the total field at different pump-probe delays as explained in Chapter 2, it is seen that the pump pulse will only interfere with the probe and diffracted pulses at zero time delay between the pump and probe. Consequently, when expressing the intensity of the field given by (4.1), cross terms between the pump and both the probe and diffracted field will be neglected. The intensity, which is proportional to the signal measured by the photodetector, is given by:

$$I_{total} = I_{scattered}^{pump} + I_{scattered}^{probe} + I_{diffracted} + 2E_{diffracted} E_{scattered}^{probe} e^{i\Delta\varphi} \quad (4.2)$$

where $\Delta\varphi = \varphi_{diffracted} - \varphi_{scattered}^{probe}$. Contributions from the first two terms can be largely suppressed by appropriate modulation and lock-in detection, although some Gaussian noise will still bleed through. Two terms remain: $I_{diffracted}$ which is the desired signal and background in the form of interference between the temporally coincident diffracted and probe pulses. The non-Gaussian noise in the data arises from the presence of this last term in (4.2) and the instability in $\varphi_{diffracted}$ which leads to instability in $\Delta\varphi$. Probe beam noise, which is essentially Gaussian, enters into the measured signal through this interference term. The mean value of the noise in the signal, however, will fluctuate because of the

instability in $\Delta\varphi$. Fluctuations in $\Delta\varphi$ which take place on a more rapid timescale than a complete data acquisition will be impossible to average out and will appear as non-Gaussian noise.

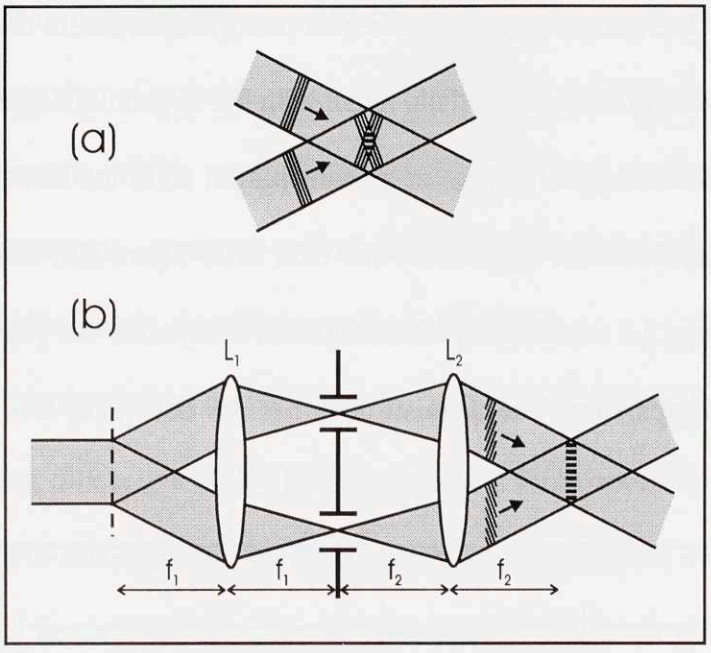

Fig. 4.1. (a) The "pancake effect". Femtosecond pulses split by a beamplsitter only overlap over a fraction of the transverse spatial extent of the beams, reducing wavevector resolution in ISS experiemnts (b). Diffractive Optic Apparatus. Pulses split with a diffraction grating and imaged with a two-lens telescope overlap over the entire area of the beams., improving wavevector resolution. In both cases, the pulses are depicted with lines of equal phase. Reproduced from ref. 3.

A novel experimental apparatus which generates transient gratings with excellent phase stability, without using any active stabilization, had just been developed for research and industrial applications in the picosecond regime[1,2]. The experimental apparatus, depicted schematically in figure 4.1(b), relies on a diffractive optic in place of a beamsplitter to separate the two pump beams. A binary phase grating which was etched to optimize diffraction into the ±1 orders is used as the diffractive optic. All other diffraction orders are blocked and the phase mask is imaged onto the sample using a two

lens telescope in an f_1-(f_1+f_2)-f_2 configuration. An enormous potential advantage had just been demonstrated for the use of this type of apparatus in the femtosecond regime[3] (see section II(i) below) and potential modifications of the technique to permit facile optical heterodyne detection of the transient grating were just being developed in the picosecond domain. Figure 4.2 depicts ISTS acoustic data, taken with the apparatus depicted in figure 4.1(b) and using a diffractive optic in place of a beamsplitter, from the same TiN sample used to measure the data shown in figure 3.8. The data from figure 3.8, taken using the apparatus shown in figure 3.2 which uses a beamsplitter to separate the pump pulses, is plotted alongside for comparison. The acquisition times for both data sets were nearly identical.

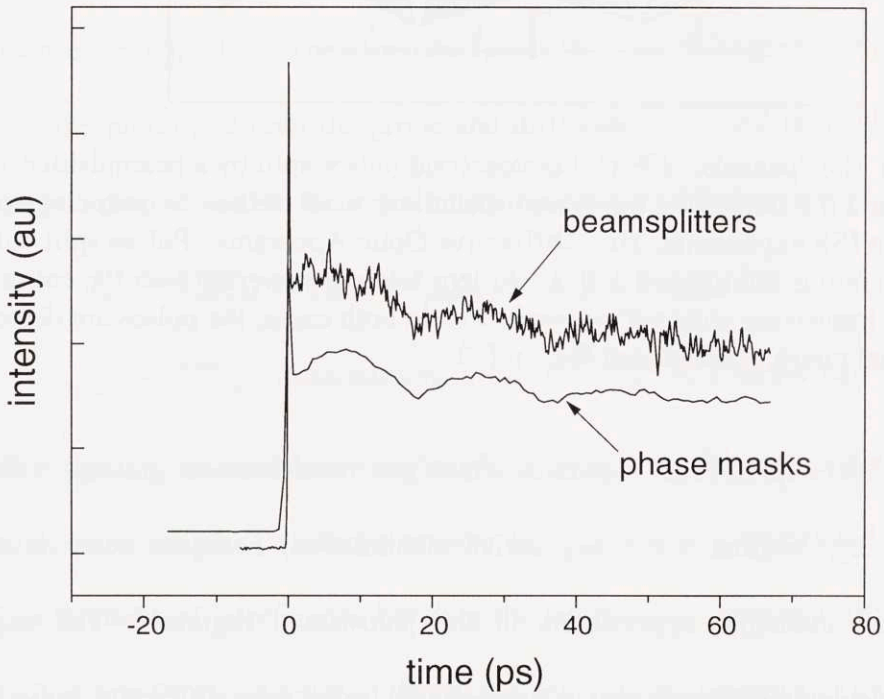

Fig. 4.2. Comparison of transient grating ISTS data taken using a beamsplitter or a diffractive optic to separate the excitation pulses. A dramatic increase in the signal-to-noise ratio is observed in the data taken with the diffractive optic apapratus, which is attributed to markedly improved phase stability of the transient grating.

The data taken using the diffractive optic apparatus shows vastly improved signal-to-noise ratio. The non-Gaussian nature of the noise was also observed to largely vanish, with increased averaging producing enhanced signal-to-noise ratios. It will be the purpose of this chapter to describe the use of the diffractive optic apparatus for the femtosecond, heterodyne detection of transient gratings. This chapter will focus on both the optical and electronic elements which were incorporated to produce an experimental system with enhanced wavevector accuracy, optical signal amplification, and enhanced information content, all while greatly simplifying optical alignment.

The layout of this chapter will be as follows. In the first section, an optical apparatus using diffractive optics to split and cross femtosecond pulses will be described and the action of this apparatus on short pulses will be explored. The use of this apparatus for the optical heterodyne detection of femtosecond timescale transient gratings will be detailed. In the second section, a system of detection electronics (including photodiode design, computer interfacing, and software) optimized for optical heterodyne detection will be expounded upon.

II. Optical Apparatus

(i). How to make femtosecond pulses overlap

It is a well known fact that crossed femtosecond pulses that have been separated by a beamsplitter have an overlap area that is much smaller than the transverse spatial dimension of the beams because of the small axial dimension of the short pulses (a 35 fs pulse is a 10 μm thick "pancake"), as illustrated in figure 4.1(a). This phenomenon, commonly called the "pancake effect,"[4] leads to a reduction in both wavevector accuracy and diffracted signal intensity when performing transient grating experiments. As

determined from the diagram in figure 4.3, the width d of the overlap region between two femtosecond pulses is roughly given by:

$$d \sim \frac{\tau c}{\sin\theta} \tag{4.3}$$

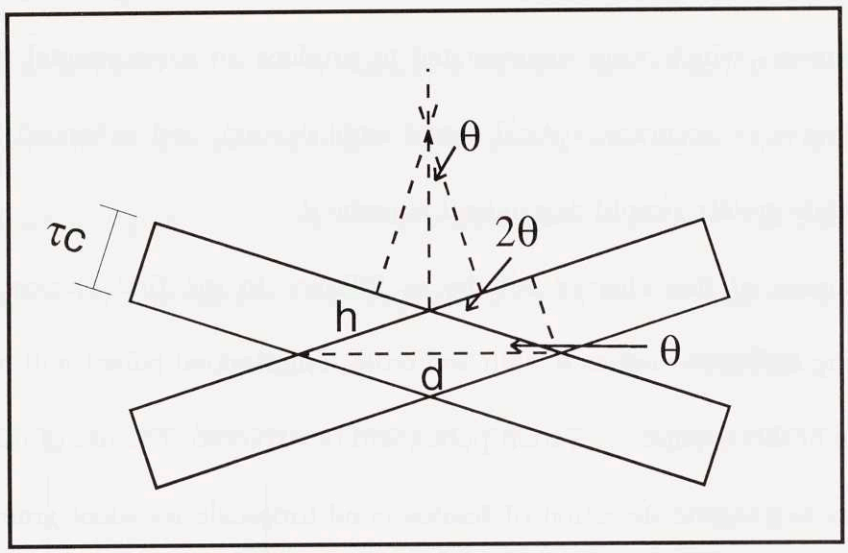

Fig. 4.3. Diagram of two, crossed femtosecond pulses.

where τ is the pulse duration and c is the speed of light. The fringe spacing Λ of the interference pattern created by the overlap between two pulses of wavelength λ crossed at an angle 2θ is:

$$\Lambda = \frac{\lambda}{2\sin\theta}. \tag{4.4}$$

Consequently, for short pulses, the number of fringes produced in the interference pattern created by crossing two pulses of duration τ is angle independent and is approximately given by the expression:

$$N \sim \frac{2c\tau}{\lambda} \tag{4.5}$$

This leads to an angle dependent wavevector uncertainty of:

$$\delta k = \frac{4\ln 2}{\delta x} \sim \frac{4\ln 2}{d} = \frac{4\ln 2 \sin\theta}{\tau c} \tag{4.6}$$

Additionally, the diffraction efficiency, defined as the ratio of the power in the diffracted field to the power in the input probe field, is quadratically related to the pulse fluence for $\chi^{(3)}$ processes like ISRS. Consequently, the diffraction efficiency for a given pump power will scale as d^2. It can be seen that the pancake effect becomes most problematic at higher wavevectors, as the diffraction efficiency decreases like $\sin^2\theta$ and the wavevector uncertainty increases like $\sin\theta$ with increasing angle and increasing wavevector. It will be shown that this limitation can be overcome through the use of the optical apparatus depicted in figure 4.1.

A qualitative picture of the performance of the optical apparatus depicted in figure 4.1 can be obtained by considering a frequency domain picture. From (4.4), the wavevector of the interference pattern created by crossing two beams is seen to be a function of the crossing angle and the wavelength of the two beams. Short pulses have a broad bandwidth, and when pulses are split with a traditional beamsplitter and then recombined, all of the different wavelengths in the short pulse cross at the same angle, producing a broad range of wavevector components in the interference pattern. In the setup used in this work, the different wavelength components in the pulse split by the grating are all diffracted and recombined at different angles, which produces a much narrower wavevector distribution in the optical interference pattern.

The quantitative treatment of a diffractive optic apparatus presented here is a close adaptation of that presented by Maznev[2]. The field of the input pulse, just before

propagating through the diffraction grating, will be assumed to have a Gaussian temporal profile:

$$E_1 = E_0 \exp\left[-(t - z/c)^2 / \tau_0^2\right] \exp\left[i\omega_0 (t - z/c)\right] \tag{4.7}$$

where ω_0 is the central frequency of light, and τ_0 is a measurement of the pulse duration related to the FWHM duration τ by $\tau_0 = \tau\sqrt{4\ln 2}$. This can also be expressed as a superposition of plane waves:

$$E_1 = \left(\frac{E_0 \tau_0}{2\sqrt{\pi}}\right) \int_{-\infty}^{\infty} \exp\left[-(\omega - \omega_0)^2 \tau_0^2 / 4\right] \exp\left[i\omega(t - iz/c)\right] d\omega \tag{4.8}$$

Consider the diffraction of one of the plane waves, with electric field given by $E_{pw} = \exp\left[i\omega(t - iz/c)\right]$ from the diffraction grating. The field of the nth order beam diffracted from a thin grating can be written[5]:

$$E_{pw,2}^{(n)} = A_n \exp\left[i\omega t - i\left(\sqrt{\omega^2/c^2 - q_n^2}\right) z - iq_n x\right] \tag{4.9}$$

where q_n is the wavevector of the grating which is related to the grating period Λ by $q_n = \frac{2\pi}{\Lambda}$, and A_n is the complex grating amplitude. A symmetric phase grating was used for all of the experiments in this work. Although A_n is ω dependent for phase gratings, for a small frequency spread $\delta\omega/\omega_0 << 1$ this dependence may be neglected. Disregarding diffraction, the action of the two lens system will be to image the field at the grating onto the sample plane:

$$E_{pw,3}^{(n)}(\omega) = A_n \exp\left[i\omega t - i\sqrt{\left(w^2/c^2 - q_n^2\right)} z' + i\left(q_n / M\right) x - iL\omega/c\right] \tag{4.10}$$

where z' is now the distance from the sample plane, $M = f_2 / f_1$ is the magnification ratio, and L is the distance between the grating plane and the z' plane with $L\omega / c$ being the overall phase shift imparted to the wave upon propagation through the lens system. The complete electric field for the nth order beam is given by the superposition of the plane waves described by (4.10) into a Gaussian pulse:

$$E_3^{(n)}(\omega) = \left(\frac{E_0 \tau_0}{2\sqrt{\pi}}\right) A_n \exp\left(iq_n x / M\right) \int_{-\infty}^{\infty} d\omega \exp\left[-\left(\omega - \omega_0\right)^2 \tau_0^2 / 4\right] \times \exp\left[i\omega t' - i\sqrt{\left(\omega^2 / c^2 - q_n^2 / M\right)} z'\right] \tag{4.11}$$

where $t' = t - L/c$, which just reflects the fact that it takes the pulse a finite amount of time to propagate through the lens system. In order to determine the pulse duration at the focal plane, it will again be assumed that $\delta\omega / \omega_0 << 1$ and that $q_n / M << \omega^2 / c^2$ at all frequencies at which $E_3^{(n)}$ is significantly non-zero. In this case, the second term in the integrand of (4.11) is approximately:

$$\exp\left[-i\omega t' - i\sqrt{\left(\omega^2 / c^2 - q_n^2 / M^2\right)} z'\right] = \exp\left[-i\omega\left(t' - z'/c + \frac{icq_n^2 z'}{2M^2 \omega}\right)\right] \tag{4.12}$$

Further, for frequencies close to ω_0, this expression can be further simplified using the following relation:

$$\frac{icq_n^2 z'}{2\omega M} \cong \frac{icq_n^2 z'}{2\omega_0 M} - \frac{icq_n^2 z'}{2\omega_0^2 M}\omega + \frac{icq_n^2 z'}{2\omega_0^3 M}\omega^2 \tag{4.13}$$

These terms generate a constant phase shift as well as a linear and quadratic phase sweep. The phase shift will not affect the form of the final expression and it will be suppressed. The linear phase sweep will produce an overall time shift of the pulse. This will also not

affect the form of the final expression in an important way and it will also be suppressed. The quadratic phase sweep will produce a stretching of the pulse. Combining (4.12), (4.13) and (4.11) yields:

$$E_3^{(n)}(\omega) = \left(\frac{E_0\tau_0}{2\sqrt{\pi}}\right) A_n \exp\left(iq_n x/M\right) \int_{-\infty}^{\infty} d\omega \exp\left[-\left(\omega-\omega_0\right)^2 \tau_0^2/4\right] \times \exp\left[i\omega\left(t'-z'/c\right)+\frac{icq_n^2}{2\omega_0 M^2}\omega^2\right] \tag{4.14}$$

Completing the square and completing the integration:

$$E_3^{(n)} \propto \exp\left(iq_n x/M\right) \exp\left(\frac{-\left(t'-z'/c\right)^2}{\tau_0^2 - i4\varphi}\right) \exp\left[i\omega_0\left(t'-z'/c\right)\right] \tag{4.15}$$

where $\varphi = \dfrac{cq_n^2 z'}{2\omega_0 M^2}$. The electric field has tilted fronts of constant phase with slope $\dfrac{cq_n}{M\omega_0}$, as seen in figure 4.3(b). The real part of (4.15) can be written in the form:

$$E_3^{(n)} \propto \exp\left(iq_n x/M\right) \exp\left(\frac{-\left(t'-z'/c\right)^2}{\tau_0^2 + 16\varphi^2/\tau_0^2}\right) \cos\left(\frac{\left(t'-z'/c\right)^2 4\varphi}{\tau_0^4 + 16\varphi^2}\right) \exp\left[i\omega_0\left(t'-z'/c\right)\right] \tag{4.16}$$

From (4.16), the new pulse duration will be defined as:

$$\begin{aligned} \tau^2 &= \tau_0^2 + 16\varphi^2/\tau_0^2 \\ &= \tau_0^2 + \frac{4c^2 q_n^4}{\omega_0^6 M^4 \tau_0^2} z'^2 \end{aligned} \tag{4.17}$$

This important result shows that, at the sample plane (i.e., $z' = 0$), the pulse duration is unaffected by propagation through the diffraction grating and lens system. The range over which the pulse stays short is roughly given by:

$$\left|z_C'\right| << \frac{\omega_0^3 M^2 \tau_0^2}{cq_n^2} \tag{4.18}$$

Under normal experimental conditions, displacements from the sample plane of 1 cm produce only a 10% change in pulse duration.

In actual practice, all but the ±1 diffraction orders are blocked. The electric field profile at the sample plane produced by these two pulses is given by:

$$E = 2A_1E_0\cos(q_1x/M)\exp(-t'^2/\tau_0^2)\exp(i\omega_0t') \tag{4.19}$$

The pancake effect has been completely eliminated! The interference pattern extends over the entire transverse spatial dimension of the input pulse. The only limit on the spatial extent of the interference pattern is the overall aperture of the optical system.

Experiments confirming these results were performed using 30-fs pulses output from an amplified Ti:sapphire system operating at an 800 nm wavelength. The beams were first crossed using mirrors and a beamsplitter, in an apparatus similar to that shown in figure 3.2. They were then crossed using the apparatus shown in figure 4.1 which used 15 cm focal length spherical mirror and gratings with spacing Λ = 10 μm. The transverse beam diameter at the input of the optical system was 4 mm. Figure 4.4 displays an image of the interference pattern at the sample plane using (a) a beamsplitter and mirrors, and (b) using a diffractive optics and two lens imaging system. The diffractive optic system clearly shows an enormous increase in the spatial extent of the interference pattern. In figure 4.5, non-collinear second harmonic generation (SHG) between the two pulses is imaged at the sample plane using both (a) the beamsplitter apparatus and (b) the diffractive optic setup. Crossing two beams in a non-linear medium produces two SHG beams which co-propagate with the transmitted fundamental and a third non-collinear beam between the fundamentals. The image taken from the beamsplitter setup clearly shows limited transverse spatial overlap between the two pulses (the "pancake effect" is

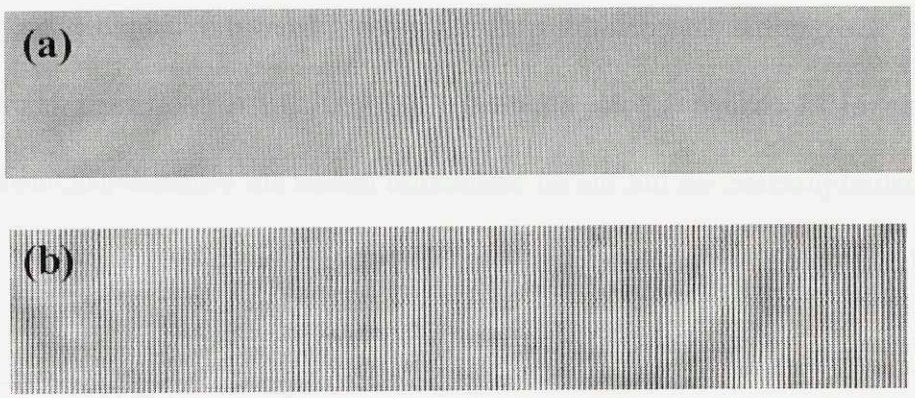

Fig. 4.4. The interference pattern created by the overlap of two 30 fs pulses (a) split and recombined with a beamsplitter and mirrors and (b) split with a diffractive optic and recombined with a two-lens imaging system. The interference pattern created by the pulses which passed through the diffractive optic apparatus extend over the entire spatial extent of the beams. Reproduced from ref. 3.

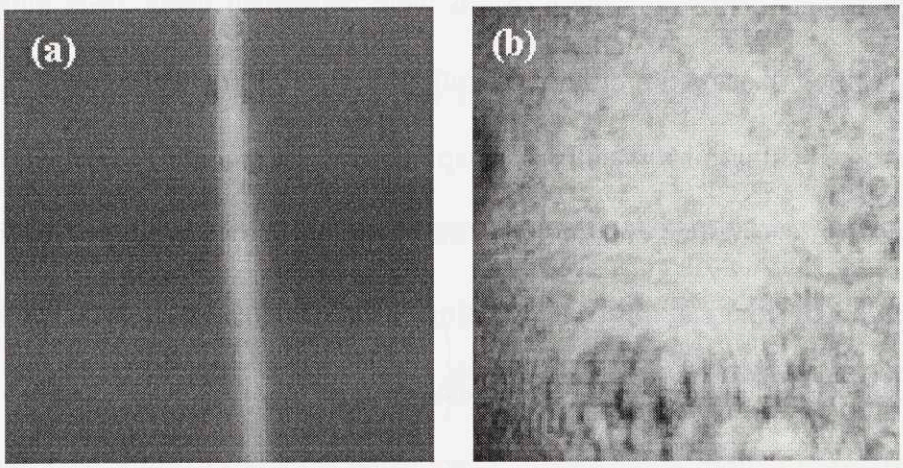

Fig. 4.5. Images of non-collinear SHG from two, crossed 30 fs pulses.(a) split and recombined with a beamsplitter and mirrors and (b) split with a diffractive optic and recombined with a two-lens imaging system. The spatial extent of the SHG beam from the diffractive optic system clearly extends over the entire area of the pulses while the SHG image from the beamsplitter system is extremely narrow. Reproduced from ref. 3.

often exploited in this type of arrangement as a single-shot autocorrelator), but the image taken from the diffractive optic setup shows overlap over the entire beam profile. Finally, the pulse duration was determined by placing a thin glass slide in each of the two diffractive orders and measuring the total non-collinear SHG intensity as a function of the

rotation angle of one of the two slides. The result is plotted in figure 4.6, where the pulse is still seen to be short at the sample plane.

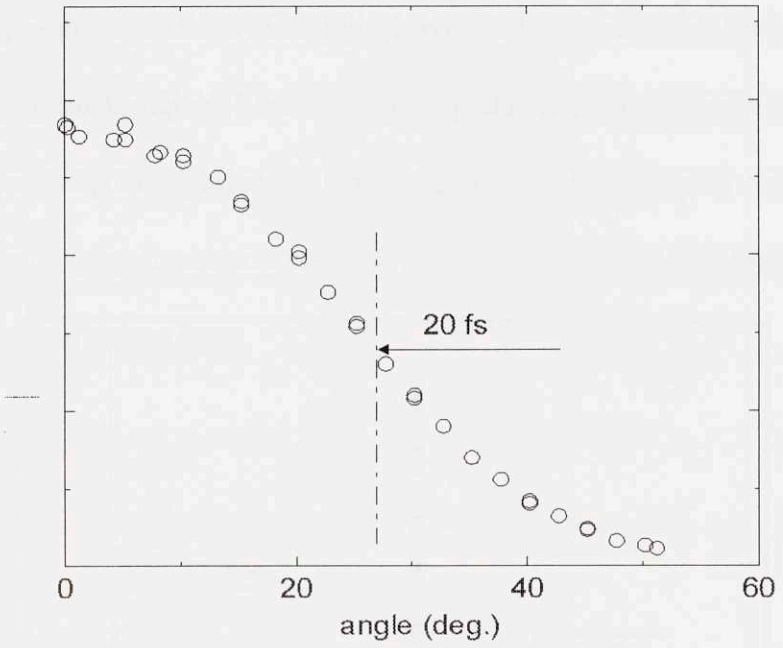

Fig. 4.6. Autocorrelation of the pump pulse at the sample plane in the diffractive optic apparatus. The optical apparatus does not introduce any dispersion into the pulse and the pulse duration remains short. Reproduced from ref. 3.

The answer to the question posed in the title of this subsection is clear. The use of a diffractive optic and a two lens imaging system is the preferred technique to cross two femtosecond pulses for most applications. The beams remain short in the front focal plane of the imaging system and they overlap over the entire spatial extent of the beam, completely eliminating the "pancake effect". An additional advantage is that the alignment of this system is extremely simple. The system contains only three optics and the two pulses are essentially guaranteed to overlap both spatially and temporally at the sample plane.

(ii). The Diffractive Optic

The ideal diffractive optic would be a symmetric transmission grating blazed to diffract entirely into the ±1 orders. Properly design binary phase gratings approaching this ideal and are easily manufactured. The performance and design of these gratings can be understood from a qualitative perspective by modeling the phase mask as two superimposed amplitude masks[6].

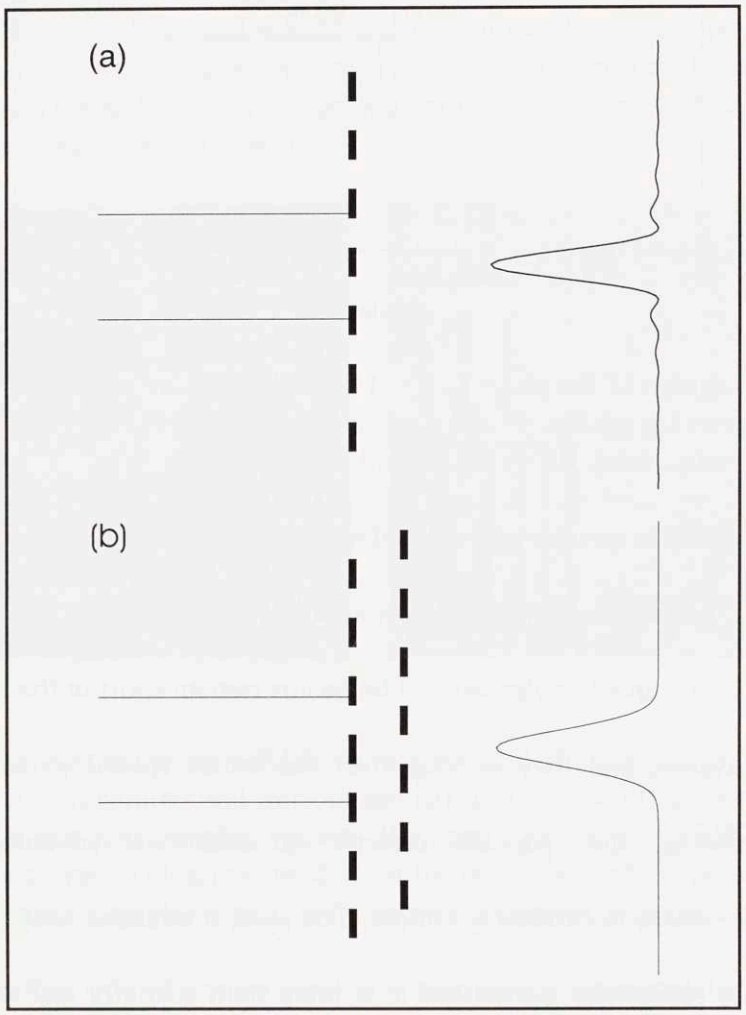

Fig. 4.7. Diffraction from (a) a mask consisting of series of slits and (b) from a spatially uniform mask that can be represented as the sum of two masks, with each mask consisting of a series of uniformly spaced slits in which one mask is offset from the other by the slit spacing. The effect of translating the mask by the slit spacing is to phase shift the non-zero diffraction orders by π.

Consider an amplitude mask which consists of a series of slits, as depicted in figure 4.7. The well-known diffraction pattern that this mask produces is also shown. If this mask is replicated, and then the replication is displaced by the spacing between the slits, this resulting pattern is just a uniform amplitude mask (see figure 4.7) which will only produce the 0^{th} diffraction order. From this result, it is apparent that the action of displacing the grating by an amount equal to the spacing between slits shifts the phase of the higher diffraction orders by π.

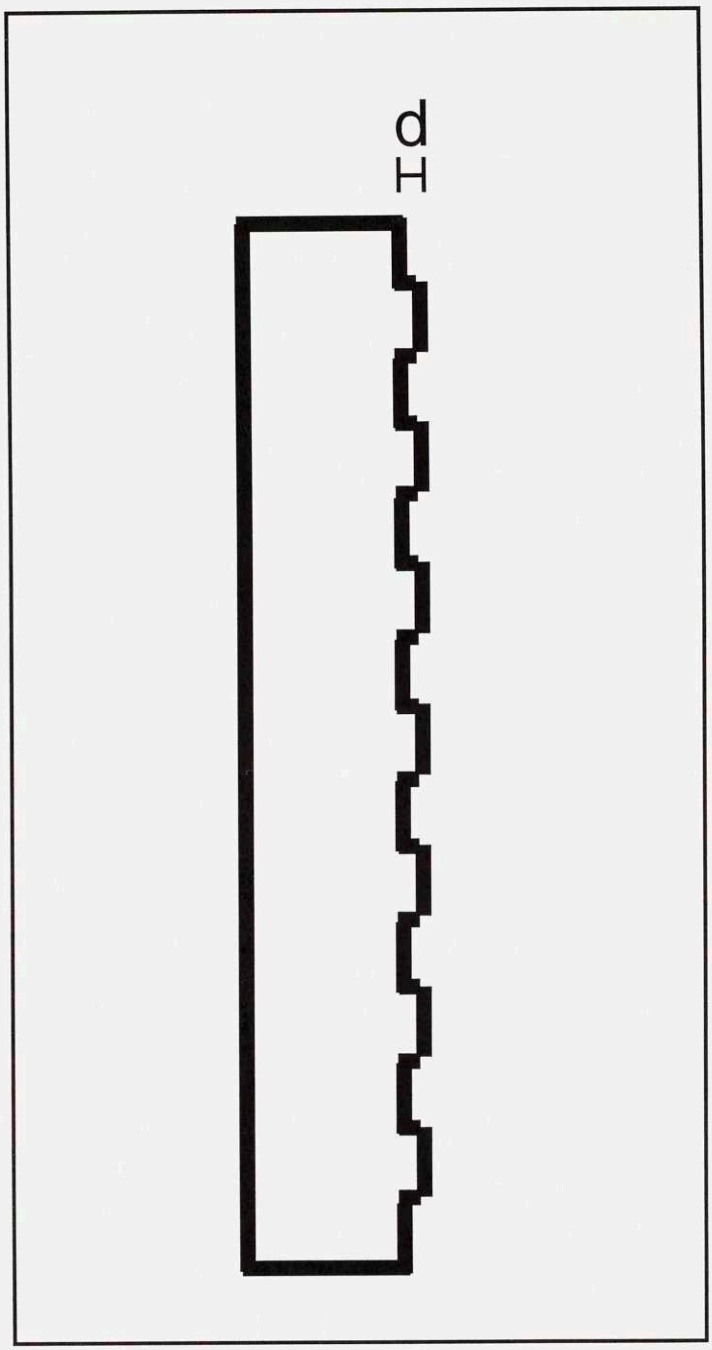

Fig. 4.8. Model for the diffractive optic which consists of the sum of two phase gratings, offset from each other by the grating spacing d. Figure features distorted for clarity.

The field produced by the binary phase grating will be modeled as the sum of the fields produced by two opaque amplitude masks: one displaced from the other in the vertical dimensions by an amount equal to the spacing between slits and in the horizontal

dimension by some distance d, as illustrated in figure 4.8. It is assumed that d is much less than the width of the slits. Let the field produced by the original (undisplaced) mask when illuminated be E_1. For all but the 0^{th} diffraction order, the field produced from the second mask will be related to the field from the first expression by:

$$E_2^{(n)} = E_1^{(n)} \exp\left(i\pi + ik\delta\right) \qquad n \neq 0 \tag{4.20}$$

where k is the wavevector of the illuminating field and δ is the optical path difference between the two slits which, for a mask of index of refraction n surrounded by air is $\delta = (n-1)d$. The factor of π results from the vertical displacement of the second mask while the $k\delta$ factor shift results from the horizontal displacement. For the 0^{th} order:

$$E_2^{(0)} = E_1^{(0)} \exp\left(ik\delta\right) \tag{4.21}$$

The total field, which is just the sum of $E_1^{(n)}$ and $E_2^{(n)}$ is given by:

$$\begin{aligned} E^{(n)} &= E_1^{(n)} + E_1^{(n)} \exp\left(i\pi + ik\delta\right) \qquad n \neq 0 \\ &= E_1^{(n)} + E_1^{(n)} \exp\left(ik\delta\right) \qquad n = 0 \end{aligned} \tag{4.22}$$

The power diffracted into each order is proportional to the intensity of the fields:

$$\begin{aligned} I^{(n)} &= 2\left(E_1^{(n)}\right)^2 \left[1 - \cos\left(k\delta\right)\right] \qquad n \neq 0 \\ &= 2\left(E_1^{(n)}\right)^2 \left[1 + \cos\left(k\delta\right)\right] \qquad n = 0 \end{aligned} \tag{4.23}$$

Optimal design can be achieved by maximizing diffraction into the higher orders (maximizing $1-\cos\left(k\delta\right)$) while minimizing diffraction into the 0^{th} order (minimizing $1+\cos\left(k\delta\right)$). This can clearly be obtain by setting $k\delta = \pi$. In general, the optimal etch depth d for light of wavelength λ and a phase mask with index of refraction n is:

$$d = \frac{\lambda}{2(n-1)} \tag{4.24}$$

Assuming that the mask material is BK7 glass, which has $n \cong 1.5$, the optimal etch depth is equal to λ. Although this maximizes diffraction into all higher orders, the first

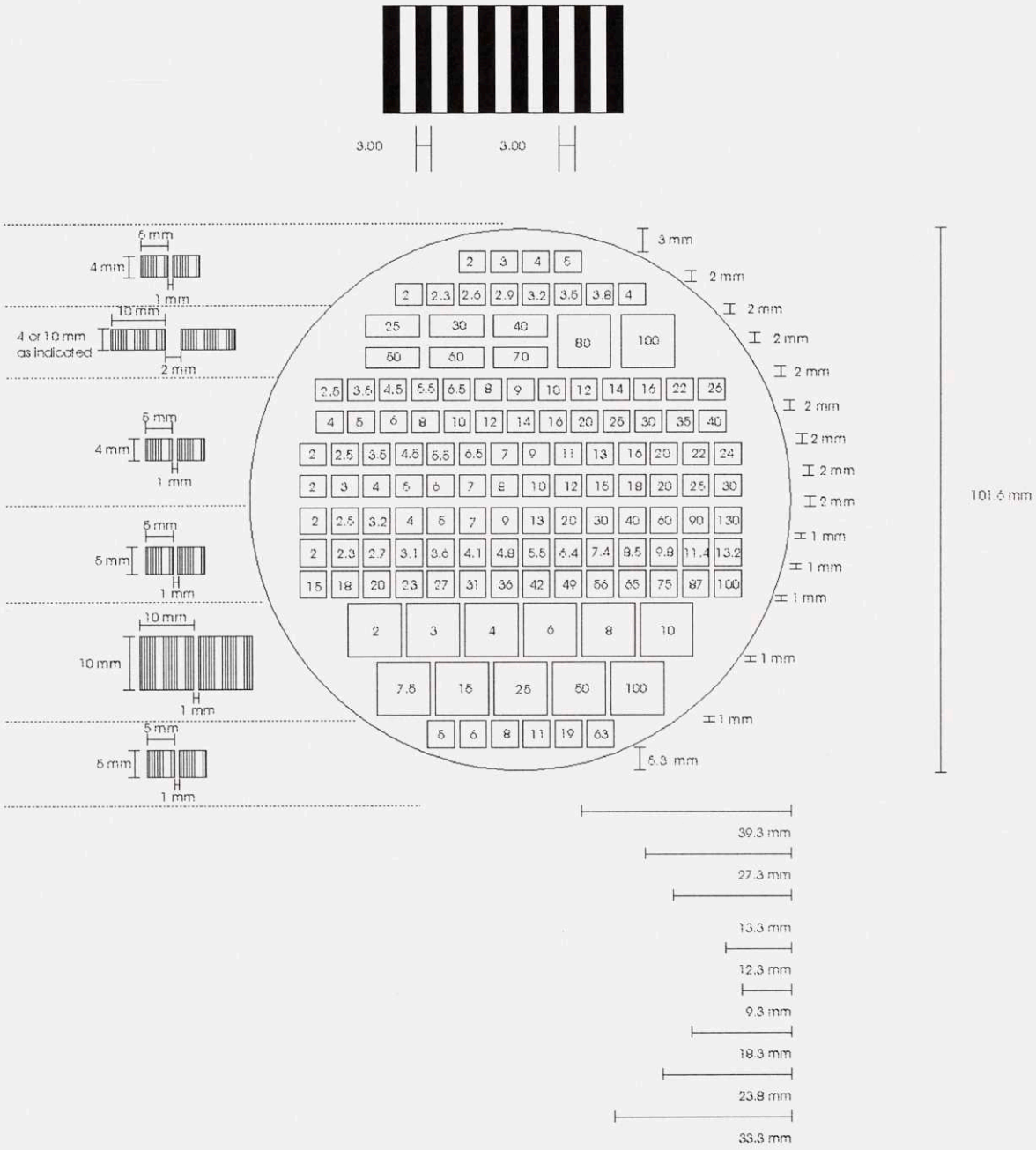

Fig. 4.9. Design for the darkfield, chrome on quartz mask used to generated the diffractive optics. Sequences of diffraction patterns were chosen to cover a range of grating spacings from 2-100 μm.

diffraction order will be the strongest[5]. While masks which eliminate higher order ($|n| > 1$) diffraction could certainly be designed, the ease of manufacturing binary gratings overrides these considerations. The binary phase gratings described in this work were typically found to diffract 70% of the energy of the incident field into the ±1 diffraction orders.

For experiments which require many wavevectors, entire sequences of masks patterns with a range of grating spacings are produced because of the high setup costs of the etching process. For this work, sequences of grating patterns were etched onto industry standard 4 inch BK7 wafers by Digital Optics Corporation. Using standard lithographic techniques, the desired mask pattern is transferred onto the wafers using a custom designed, chrome on quartz darkfield mask, manufactured by Diamond Images. The manufacture of these masks requires that the desired mask pattern be rendered in a gds2 file. These files controls the electron beam that writes the pattern onto the lithography mask. The gds2 file was created by Advanced Reproductions from a CAD file created in house and shown in figure 4.9. This CAD file was co-created by the author and Dr. Dora Paolucci. The wafer was cut into horizontal sections. Using these rows of patterns, the grating spacing can be easily changed by simply translating the glass substrate so that a selected mask pattern is situated in the beam path. This is another significant advantage of using the diffractive optic setup to perform transient grating experiments. Note that for applications needing fewer wavevectors, standard glass or plastic phase masks are readily available at low cost.

(iii). Heterodyne Detection

The primary advantage that the transient grating technique enjoys over competing techniques such as pump-probe measurements which monitor transient reflectivity or transmission is that the transient grating technique permits control over the wavevector of the sample response. The major tradeoff for this advantage is loss of a linear relationship between the sample response and the detected optical signal. This becomes especially problematic in weakly scattering samples, in samples of poor optical quality, and in samples in which multiple material responses are driven. It is well known that mixing the diffracted field with a strong local oscillator field at the photodetector will linearize the signal dependence on the material response in the transient grating technique. This can be easily seen by writing the intensity of the total field measured at the detector, which is the squared sum of the diffracted field $E_D e^{i\varphi_D}$ and the local oscillator field $E_{LO}e^{i\varphi_{LO}}$, as seen in (4.2) with $E_D = E_{diffracted}$:

$$I = \left|E_D e^{i\varphi_D} + E_{LO} e^{i\varphi_{LO}}\right|^2 = I_{LO} + I_D + 2E_D E_{LO}\cos\left(\varphi_D - \varphi_{LO}\right) \tag{4.25}$$

The first term gives a constant background signal which can be suppressed electronically, the second term describes the usual intensity of the diffracted probe beam, and the final cross term details the desired optical mixing. Techniques which seek to linearize the signal dependence through the measurement of this cross term are referred to as heterodyne detection techniques if the optical frequency of the local oscillator field is different from that of the diffracted field and homodyne detection if the frequencies are the same. The cross term is linearly related to the diffracted field and its magnitude is proportional to the local oscillator strength. This can be independently controlled, which

permits the optical amplification of weak signals (by increasing E_{LO}) and it becomes possible to selectively probe the real or imaginary part of the sample response by varying the phase of the local oscillator (by varying $\varphi_D - \varphi_{LO}$)[2].

The primary impediment to the more widespread application of these types of optical field mixing techniques is the strict set of experimental requirements: the phase difference $\varphi_D - \varphi_{LO}$ between the diffracted and reference field must be kept stable over the entire data acquisition time, the diffracted and reference fields must propagate collinearly, and both probe and local oscillator pulses must arrive at the detector simultaneously. The phase stability requirement has typically required the use of actively stabilized optical systems[7-9] or diffraction from a thermal grating[10] to provide the local oscillator. This phase stabilization problem, however, is exactly the same issue that was faced in stabilizing the grating phase in the ISTS measurements of thin films! There are two phase stabilization requirements for heterodyne/homodyne transient grating experiments: the grating phase must be stable, and the local oscillator phase must remain stable relative to the probe phase. The former can be achieved simply by using the diffractive optic apparatus to split and recombine the pump beam. The latter requirement can be met by passing the probe pulse through the same diffractive optic setup as the pump beams, as depicted in figure 4.10. The probe beam is split by the diffractive optic into two beams, one of which continues on in service as a probe beam while the other serves as the local oscillator. As shown in the diagram, the local oscillator beam passes through the sample, unaffected to first order in $E\sqrt{D_E}$ after which it propagates collinearly and simultaneously with the Bragg diffracted pulse from the probe beam.

Additionally, when the probe beam is passed through this apparatus, it arrives at the sample automatically phase matched for Bragg diffraction off the transient grating, greatly simplifying alignment. The intensity of the reference beam can be controlled by inserting optical density filters into the reference arm. A glass plate (whose thickness closely matches that of the OD filters) is then inserted in the probe arm. Rotation of the filters or the glass slide provides fine control over the phase difference between the reference and diffracted beams. Because the probe and local oscillator beams pass through almost entirely the same optics, and because the transient grating phase is extremely stable, no active stabilization is required in this apparatus.

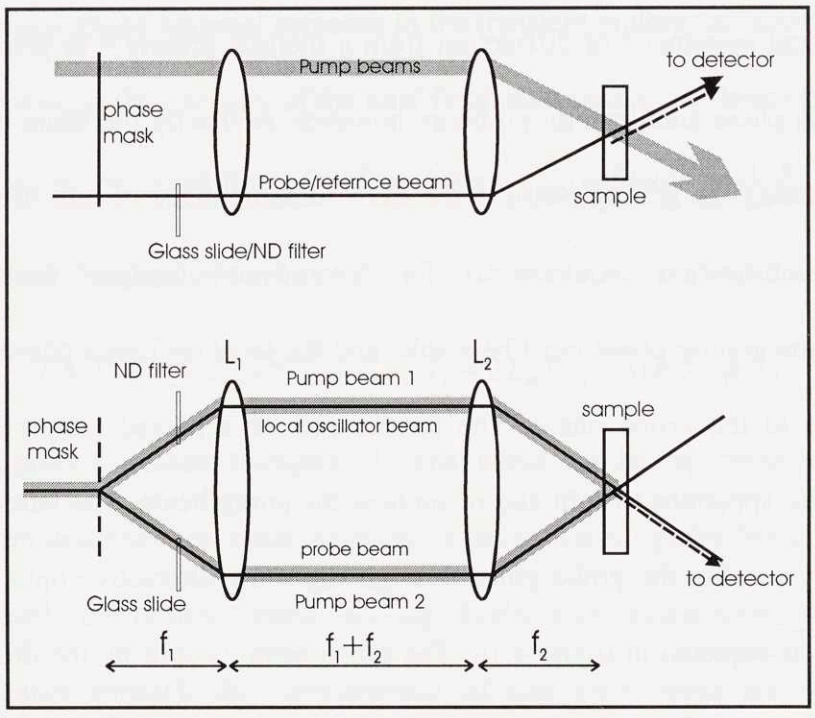

Fig. 4.10: Side-view (a), and top-view (b) of the experimental apparatus for optical heterdyne detection of transient gratings. Vertically displaced pump and probe beams are split by a diffractive optic and recombined at the sample with a two-lens telescope. Lens L1 is a cylindrical lens, focusing in the horizontal dimension, while L2 is a spherical lens. L1 and L2 image the plus and minus 1 orders diffracted from the grating onto the sample plane. L2 additionally ensures vertical overlap of the pump and probe beams. The phase of the reference beam is adjusted by rotating a filter in the reference arm. The glass in the filter is balanced in the probe arm by a glass slide.

It is instructive to consider the form that expression (4.25) takes when the experimental apparatus of Fig. 4.10 is used to heterodyne detect two counter-propagating, plane-wave phonon-polaritons with frequency ω_0 (see Chapter 5 for a description of phonon-polaritons). Note that the local oscillator will often be called a reference field or beam throughout this treatment to preserve historical consistency.(i.e., $E_{LO} \equiv E_R$) The diffracted field takes the form:

$$E_D = \frac{i\sqrt{D_E\left(E_e^2\right)}}{2} E_p e^{-\gamma t}\left[e^{i(\omega-\omega_0)t} - e^{i(\omega+\omega_0)t}\right] \tag{4.26}$$

where E_p is the probe electric field, $D_E\left(E_e^2\right) = I_D / I_P$ is the diffraction efficiency which is quadratically dependent on the excitation field E_e, and ω is the optical carrier frequency of the probe beam. The two complex exponential terms describe Stokes and anti-Stokes scattering from the two plane waves. Using the experimental apparatus shown in figure 4.10, the reference beam, with initial intensity I_R^0, loses energy through diffraction after passing through the sample, so the reference beam at the detector I_R is given by :

$$I_R = I_R^0 - D_E\left(E_e^2\right) I_R^0 e^{-2\gamma t}\left[1-\cos(2\omega_0 t)\right] \tag{4.27}$$

Making the approximation that $D_E << 1$, the reference field is given by:

$$E_R = E_R e^{i\omega t + i\varphi} - \frac{D_E\left(E_e^2\right) I_R e^{-2\gamma t}\left[1-\cos(2\omega_0 t)\right] e^{-i\omega t - i\varphi}}{2E_R} \tag{4.28}$$

This reference field is at a slightly different centered frequency than the Stokes and anti-Stokes shifted diffracted field, leading to this technique's sobriquet: heterodyne detection. The signal is given by the sum of the square of (4.26) and (4.28):

$$
\begin{aligned}
I_S &= \left|E_D + E_R\right|^2 \\
&= I_R + D_E\left(E_e^2\right)\left(I_p - I_R\right)e^{-2\gamma}\left[1-\cos(2\omega_0 t)\right] \\
&+2\sqrt{D_E\left(E_e^2\right)}E_P E_R e^{-\gamma}\sin(\omega_o t)\cos\phi + \vartheta\left(D_E^{3/2}\right) \\
&= I_R + \alpha I_D + I_H + \vartheta\left(E_e^3\right)
\end{aligned}
\tag{4.29}
$$

The first term on the right I_R, contributes a constant background, the second term is proportional to the unheterodyned diffraction intensity, and I_H is the heterodyne signal. Experimentally, I_R can be subtracted off and αI_D can be made negligibly small with a suitable choice of reference intensity. The heterodyne term is seen to be linearly related to the material response, having the same frequency and damping rate as the polariton. This term can be selectively amplified optically by increasing the reference beam intensity. Additionally, I_H is sensitive to the phase difference between the diffracted and reference fields. It should be noted that in this experimental geometry, it is possible to completely eliminate the diffracted term by setting $I_R = I_P$. This occurs because light diffracted from the probe into the transmitted reference is exactly matched by light diffracted out of the reference into the transmitted probe. Finally, (4.29) is only valid in the limit of small diffraction efficiencies, and consequently, in the low excitation energy or thin sample regime. The use of this experimental arrangement for the heterodyne detection of higher order phenomena (hyper-Raman or multi-dimensional Raman for example) requires the inclusion of higher order terms.

With the proper choice of reference beam intensity, heterodyne detection provides optimal signal to noise ratios. Figure 4.11 plots the magnitude of noise in the reference beam δI_R , the magnitude of the signal terms $I_D + 2\sqrt{I_R}\sqrt{I_D}$ in (4.25), and constant

background noise (such as parasitically scattered light or electromagnetic interference in the detector electronics) as a function of reference beam intensity. This

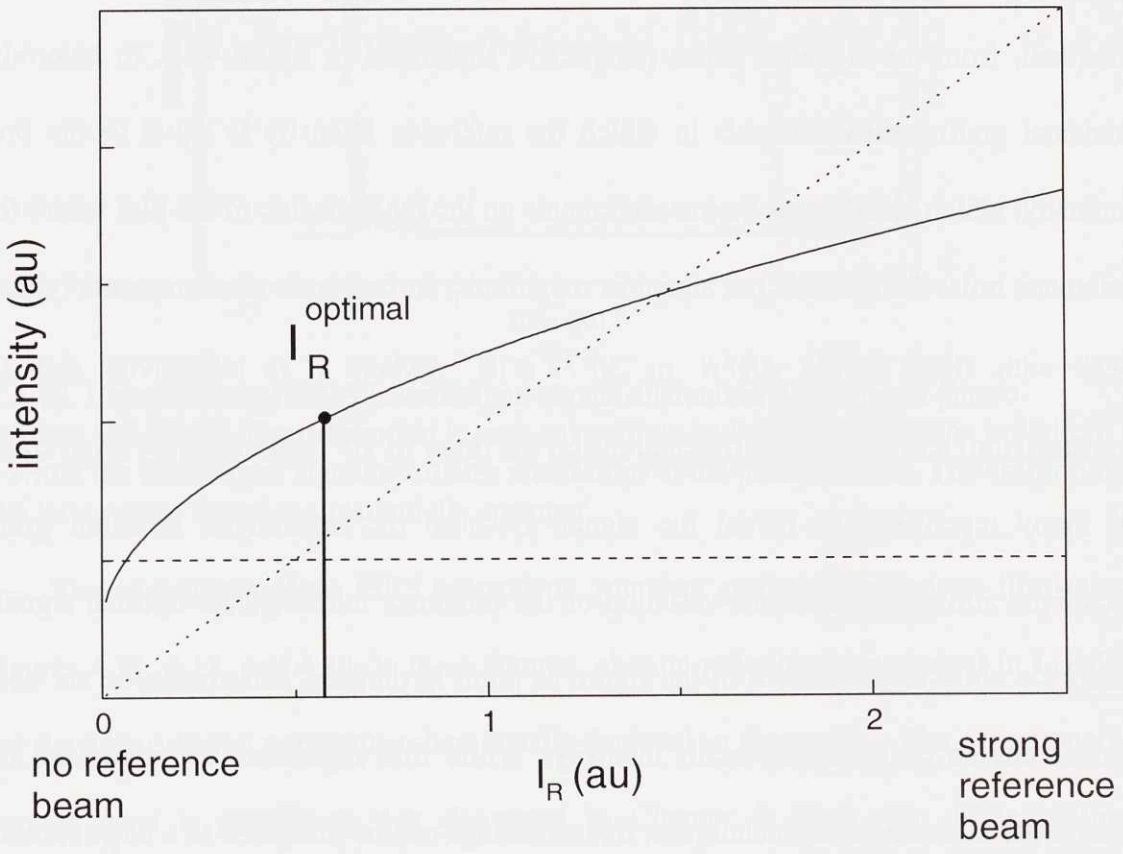

Fig. 4.11. The magnitude of the heterodyne contribution (solid line), the reference noise contribution (dotted line), and background noise contribution (dashed line) to the measured signal are plotted as a function of reference intensity. Optimal signal-to-noise ratios are obtained when the reference intensity is adjusted to maximize the difference between the heterodyne term and the reference noise.

figure is a reflection of the tradeoff between amplification and noise in heterodyne detection. In the limit that $E_R = 0$, the signal terms are equal to the diffraction intensity I_D, which in this example is less than the background noise level making it very difficult to detect. As the magnitude of the reference beam is increased, the signal term increases above the background level at which point it can be easily detected. Continued increasing

of the reference beam decreases the ratio of the signal (which is increasing like $\sqrt{I_R}$) to the reference noise (which is increasing linearly with I_R) until the reference noise exceeds the signal. Probing techniques which measure transient reflectivity or transmission are identical, from the signal to noise perspective illustrated in figure 4.11, to heterodyne transient grating measurements in which the reference intensity is equal to the probe intensity, which clearly puts the measurements on the far right side of the plot where the reference noise far exceeds the signal in magnitude. In fact such measurements typically peak with signal levels $\Delta R/R$ or $\Delta T/T \cong 10^{-5}$ (where R is reflectivity and T is transmission) and with probe fluctuations on the order of 10^{-2} and must rely on averaging of many repetitions to reveal the signal. Because the heterodyne transient grating technique allows a continuous variation of the reference intensity, the optimal signal to reference noise ratio, marked in the figure as point I_R *optimal*, can always be set with a proper choice of reference beam intensity. While this represents an advantage over conventional pump-probe techniques, this advantage can be mitigated to a large extent by electronic subtraction of the reference noise. This capability is frequently incorporated into pump-probe detection electronics, and it is incorporated into the heterodyne detection electronics described in the next section.

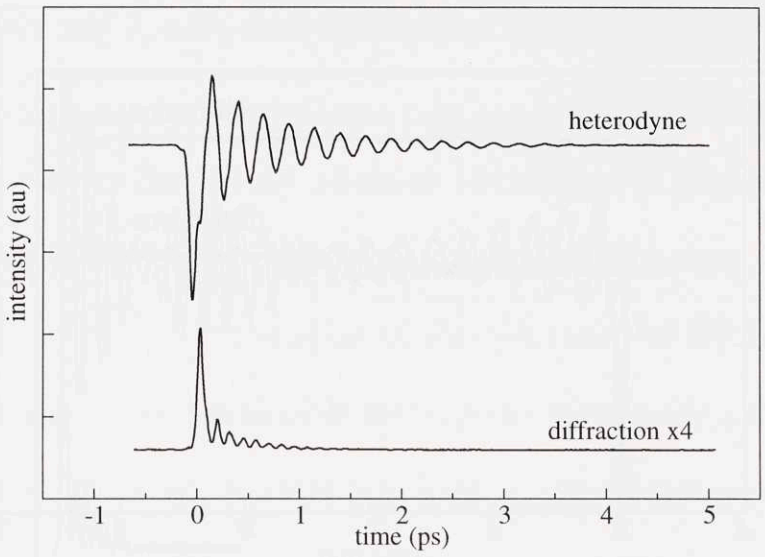

Fig. 4.12. Comparison of ISRS heterdodyne versus diffraction detection of phono-polaritons in $LiTaO_3$. The diffraction is seen to oscillate and damp at twice the polariton rate while the heterodyne signal oscillates and damps at the polariton rate. The ampltitude of the heterodyne signal is substantially stronger.

The advantages of the ISRS heterodyne, transient grating detection are illustrated in figures 4.12, 4.13, and 4.14. In these figures, phonon-polaritons are excited in $LiTaO_3$ using the experimental apparatus schematically depicted in figure 4.10. The experimental apparatus used is similar to that described in Chapter 5. Here, the phase grating wavelength is 10 μm and the reference intensity is roughly equal to the probe intensity. Figure 4.12 illustrates the advantages that linearity confers upon heterodyne data compared with the diffracted signal. The diffracted signal is seen to be much weaker and to oscillate and damp at twice the material rate, while the heterodyne signal is much greater and it oscillates and damps at the same rate as the material. This provides a two-fold increase in the number of resolvable oscillations, improving the frequency resolution

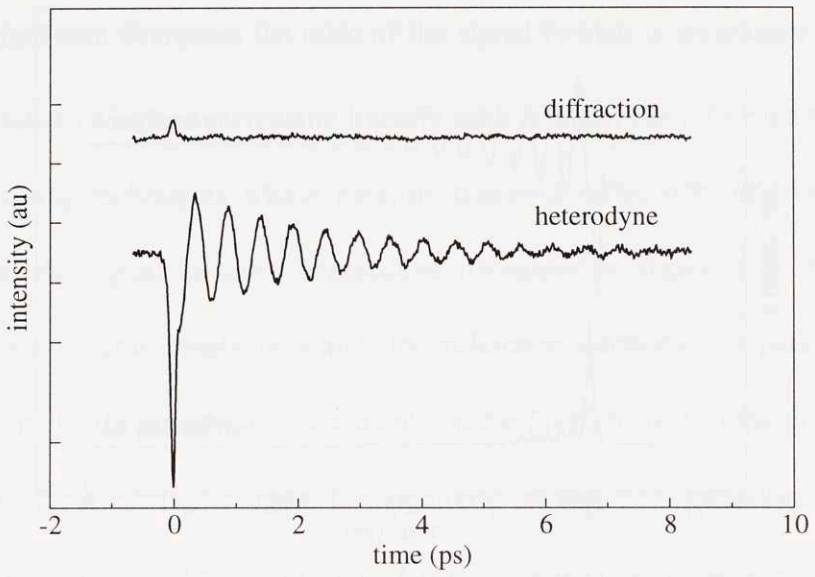

Fig. 4.13. Heterodyne amplification of ISRS data from $LiTaO_3$. The diffraction signal is swamped by noise but the heterodyne signal shows clearly resolved oscillations.

of the technique. Figure 4.13 displays the ability of heterodyne detection to amplify a signal above the background noise level. The diffracted signal is seen to be completely swamped by noise from parasitically scattered pump light, while the heterodyne signal shows clearly resolvable oscillations. Figure 4.14 highlights the advantages of signal linearity when measuring samples with multiple frequencies. The $LiTaO_3$ crystal from which this data was collected is extremely thin ~100 μm, and the multiple frequencies are robably the result of waveguide effects. The distinct beating patterns associated with multiple frequencies are clearly evident in the heterodyne signal while they are barely resolvable in the diffraction data.

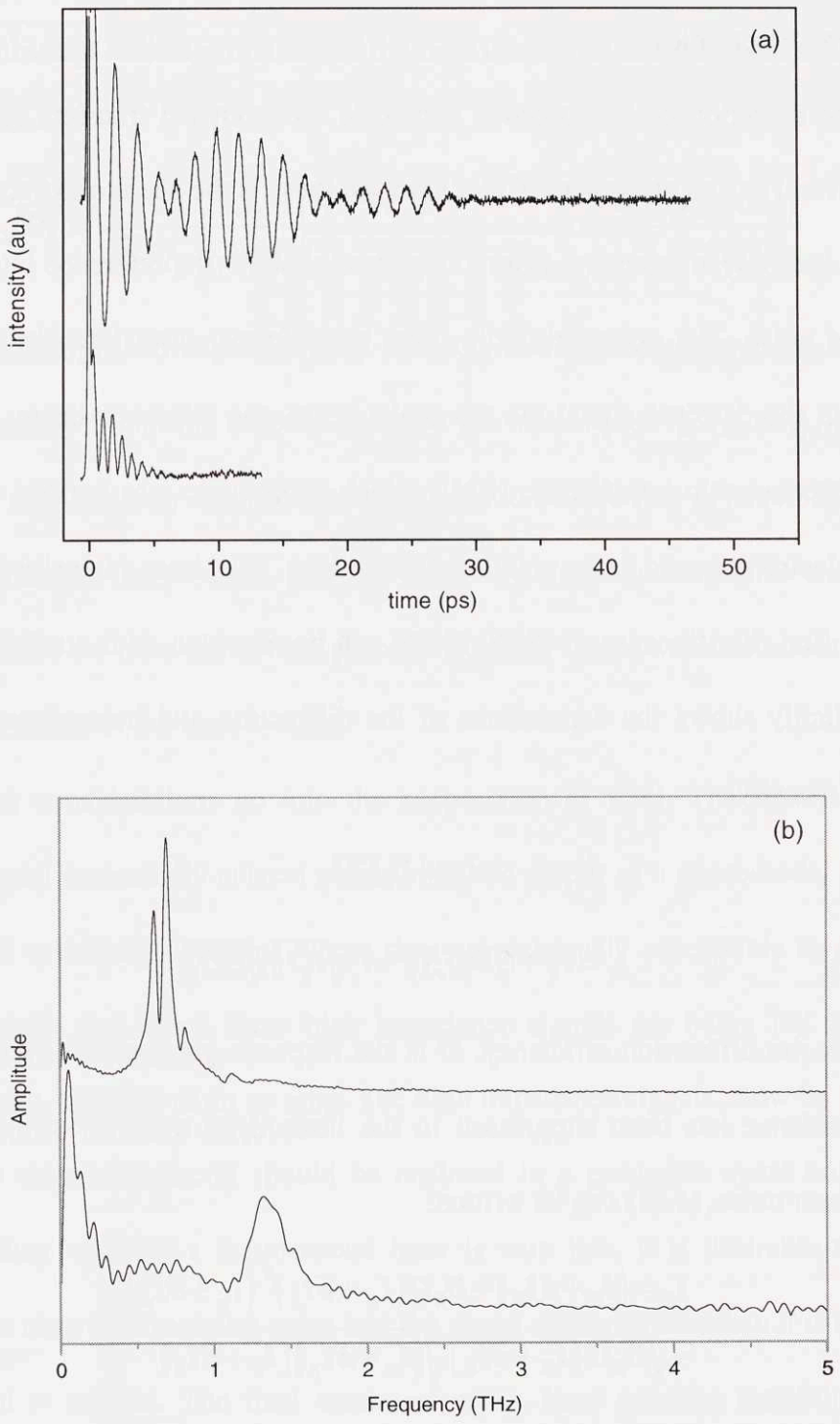

Fig. 4.14. The advantages of the heterodyne detection of samples with multiple response frequencies (a) ISRS and (b) the power spectrum. The heterodyne signal (upper lines) clearly shows the beats characteristic of multiple response frequencies, while the multiple frequencies are difficult to clearly resolve in the diffraction signal (lower lines).

III. Detection Electronics

The detection of femtosecond timescale, heterodyned transient grating signals presents several design challenges. Chief amongst these is the need to extract a very small signal (the heterodyne intensity) from a large background (the reference intensity) in the presence of noise. The noise primarily takes three forms: laser intensity noise, which shows up in the detected signal via the probe beam, the reference beam, or the pump beam, electromagnetic interference (EMI) which can couple into various stages of the detection electronics, and laser pointing fluctuations. The laser intensity noise will be considered first. For the case of ISRS, (4.25) can be rewritten with a substitution for I_D which explicitly shows the dependence of the diffraction and heterodyne term on the excitation intensity:

$$I_D = D_E G I_e^2 \tag{4.30}$$

$$I_s = I_R + G D_E I_e^2 I_p + I_e \sqrt{I_p I_R} \sqrt{G D_E} \tag{4.31}$$

where D_E is the diffraction efficiency, G is the response generation efficiency and the phase dependence has been suppressed in the heterodyne term for simplicity's sake. Including laser noise, (4.31) can be written:

$$\begin{aligned} I_S = &\left(I_R + \delta I_R\right) + D_E G \left(I_E + \delta I_E\right)^2 \left(I_p + \delta I_p\right) \\ &+ \sqrt{D_E G}\left(I_E + \delta I_E\right) \sqrt{\left(I_p + \delta I_p\right)\left(I_R + \delta I_R\right)} \end{aligned} \tag{4.32}$$

where δI is the laser intensity noise. It will be assumed that $I_R >> I_D$ so that the diffraction term can be ignored, that $\delta I_E / I_E = \delta I_R / I_R = \delta I_p / I_p$, and that $I_E \propto I_R \propto I_p$. The objective is to extract $\sqrt{D_E}$ (or something proportional to it) given I_S. This can be

achieved by subtracting $I_R + \delta I_R$ from the measured signal and normalizing by $I_x + \delta I_x$ where the x subscript indicates that any of the field intensities may be chosen. This can be expressed:

$$\sqrt{D_E} = \frac{I_S - (I_R + \delta I_R)}{\sqrt{G}(I_E + \delta I_E)\sqrt{(I_R + \delta I_R)(I_p + \delta I_p)}} \propto \frac{I_S - (I_R + \delta I_R)}{(I_R + \delta I_R)^2} \tag{4.33}$$

This can be accomplished experimentally by using two photodetectors; one to measure the signal intensity I_S and the other to measure the intensity of I_E, I_R, or I_p, any one of which can be electronically amplified or attenuated to behave like I_R in (4.33). It will be necessary to measure these values, perform the subtraction, and normalize on a shot-by-shot basis because the laser has several percent "popcorn" noise which is essentially at the 1 kHz repetition rate of the laser system.

Several considerations go into the suppression of EMI. The first is that high impedance signal (essentially current pulses) like the output of a photodiode, should not be propagated over long distances where they are extremely susceptible to corruption. This is especially true when these high impedance signals are being fed into a high impedance input, like that of an op amp. The high impedance signals show be shielded at all times and the entire circuit should be enclosed in a grounded metal box. Second, because the duty cycle of a femtosecond laser is very low, it is desirable to gate the optical signals to avoid averaging noise into the signal during times when it is known that no real signal is present. The final source of noise, laser pointing instability, is very difficult to eliminate. Using a long focal length lens to image the amplifier output onto the sample improves the condition to a certain extent, but the problem still persists.

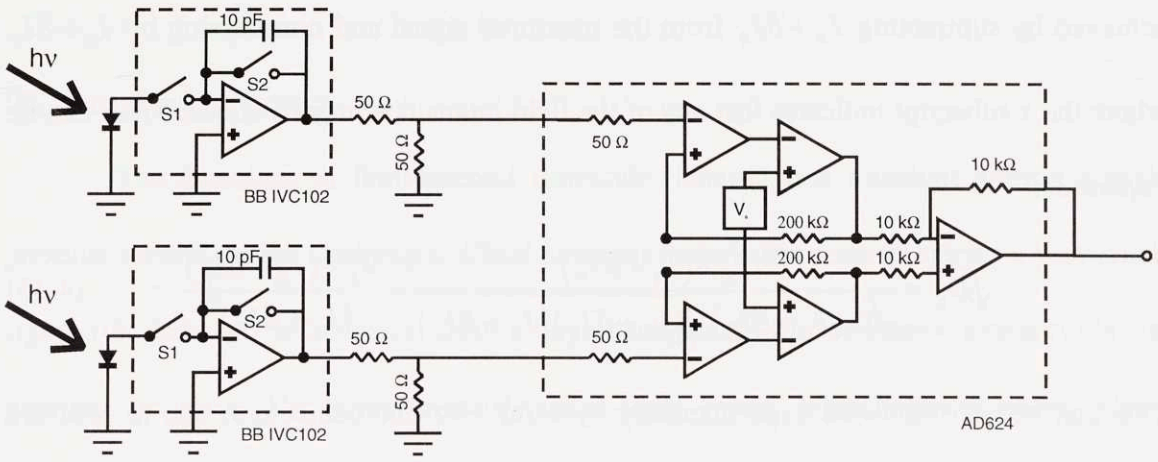

Fig. 4.15. Circuit schematic for differential detection of optically heterodyned signals.

Gated, amplified diodes were constructed to achieve the best possible signal-to-noise ratios. The circuit schematic diagram for these diodes, and the subtraction electronics, shown in figure 4.15, and the actual circuit topology for the diodes is presented in figure 4.16. Although most of the data presented in this work were taken during the various prototyping stages of this system, only the final and most complete detection system will be shown here. Comments will be added in the individual thesis sections indicating the detection system used in each experiment. The current pulse from the diode propagates less than two centimeters before being fed into the amplifier circuit. The amplifier is a switched, gated transimpedance amplifier which is fabricated as a monolithic chip (Burr-Brown IVC102). The laser Pockels cell trigger is used to close gate S1, which passes the current pulse onto capacitor C1. This produces a voltage drop across the input terminals of the op amp which is counteracted by the op amp output. This action produces the desired conversion of the current pulse (high Z) to a voltage pulse (low Z). The amplifier continues to integrate the current from the diode until switch S1is opened ~100 μs later (a smaller value could certainly be used) and the circuit holds the

value of the integrated current as an output voltage until it is reset by applying a trigger to gate S2. This is performed just prior to the arrival of the next pulse. The trigger is taken from the trigger to the Q-switch trigger of the Nd:YLF laser which pumps the Ti:sapphire laser amplifier. The circuit topology was mainly designed to shield the high impedance op amp input from capacitively coupled noise, especially from the digital gates and the power inputs. The op amp pin input was surrounded by analog ground and the digital inputs were surrounded by digital ground[11].

Two amplified diodes were constructed as described above. One detects the signal while the other detects an extraneous reflection of the excitation beam off a thin film polarizer. This reflection is passed through a polarizer which can be rotated to optically

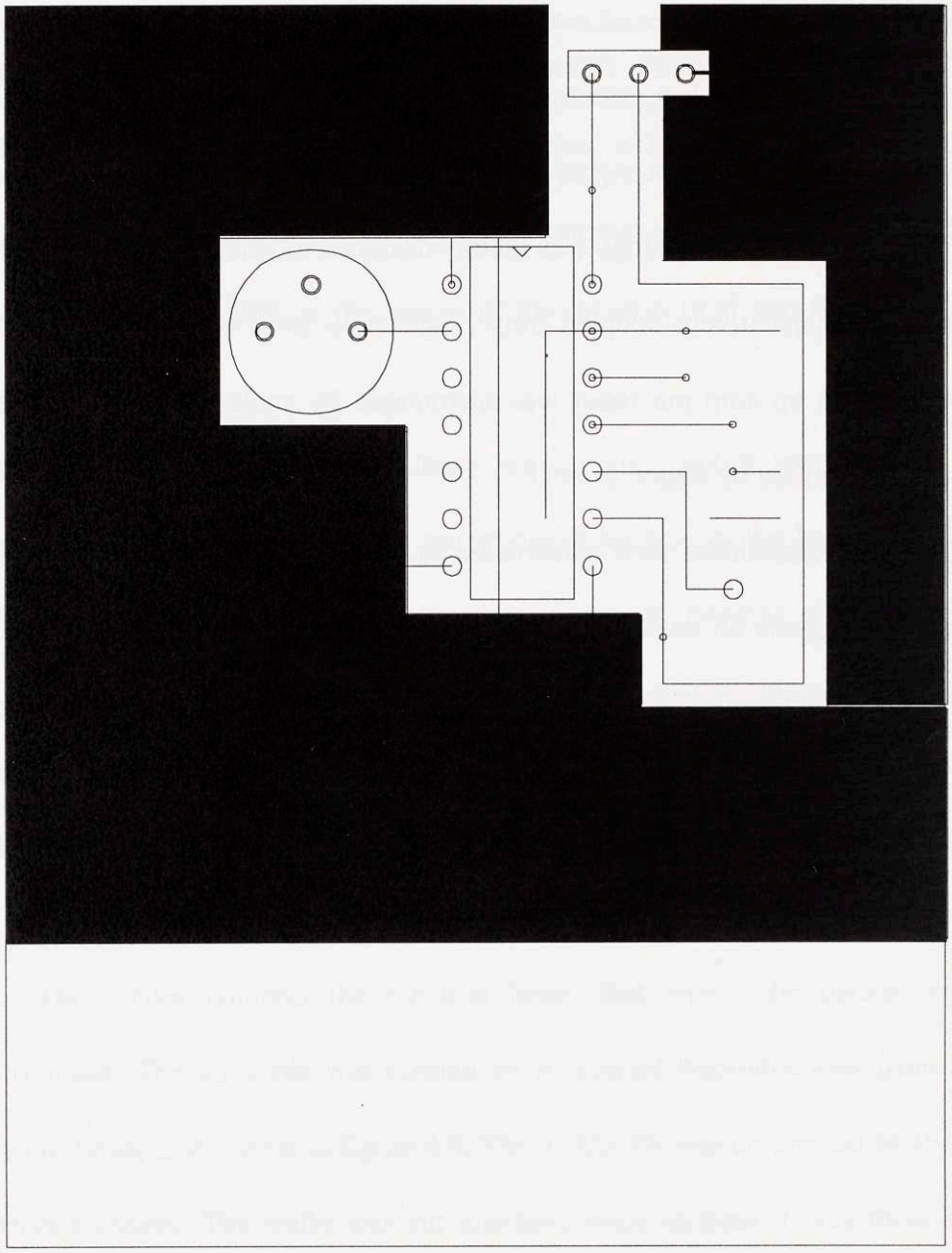

Fig. 4.16. Circuit topology for gated, integrating, amplified photodiodes. The high impedance input into pin 2 is guarded by an analog ground line and the TTL inputs into pins 11 and 12 are isolated from the pin 2 inputs by an digital ground plane.

balance the two diodes. Analog subtraction is performed using an instrumentation amplifier (Analog Devices AD624) to maximize common mode rejection. Analog subtraction of the reference intensity, as opposed to digital subtraction, was chosen to reduce the demands on the data acquisition (DAQ) board as very high digital resolution is

required to detect an extremely small signal on a large background. The output of the instrumentation amplifier and the reference intensity were fed into two channels of a 12 bit Lab PC+ National Instruments DAQ board. The pump beam was synchronously chopped at 500 Hz in these experiments, with the chopper being driven by a 500 Hz TTL train produced, via a simple digital downcounter, from a 1 KHz train taken from the laser amplifier (see [12] for more complete explanation). The state of this 500 Hz TTL line, which reflects the chopper state, was input into a third channel on the DAQ board. The board was set to measure on differential mode because of the TTL's unique digital ground. The ground of the amplified diodes was tied to the building ground which was found to reduce EMI coupled into the circuit.

The input values at the DAQ's channels were read into software using Labview. Labview is a graphical programming language designed to interface with laboratory equipment[13]. The low level functions used to read in the data were written by Dr. Ciaran Brennan and their operation is detailed in his thesis[12]. The software described below follows many of the same techniques applied by Brennan, with the exception of signal normalization. At the beginning of an acquisition, the laser intensity is monitored for 1s to determine the mean and standard deviation. The user sets an intensity gate by inputting the number of standard deviations from the mean that a pulse intensity can fall before the entire data point is rejected. A range of delay line positions are input by the user. The program positions the delay line at the first and then reads the voltage level on the three input channels. The user inputs the number of pulses N that are to be collected at each delay line position. N points are collected by the board and returned to software. The software first determines if the pulse intensity falls outside of the defined standard

deviation gate, discarding the excursive readings. The program checks the value of the chopper state and either adds the signal channel value to a running total (unchopped) or subtracts it (chopped). This performs the function of a lock-in detector. The value of the m^{th} signal pulse I_S^m is normalized in the following fashion:

$$\frac{\left(\sum_{i=1}^{N} I_R^N\right)^2}{N^2\left(I_S^m\right)^2} I_S^m \tag{4.34}$$

This type of normalization factor has been suggested to be an improvement over simply $\left(I_S^m\right)^2$ [14]. The running total is divided by $N/2$ and this value is assigned as $\sqrt{D_E}$ at that position of the delay line. The delay line is then re-positioned and the procedure is repeated for each point along the delay line range, to make up an entire scan. It was found that the best signal-to-noise ratios are obtained by reducing N to a low value and increasing the number of scans, because much of the laser noise is at a very low frequency. Rapid scans, at a higher frequency than the laser noise, will affect the form of the data less than fewer, longer scans at a lower frequency.

The linearity of the amplified diodes was tested by measuring the voltage across the 50 MΩ input impedance of an oscilloscope as a function of input light intensity which was controlled by the rotation of a polarizer. The amplified diode circuit is linear up to at least 2 V when loaded by 50 MΩ. The performance of the diode pair and subtraction circuit were also tested. Fifty milliseconds of diode output were recorded by a digital oscilloscope, and the scan was converted into a histogram that was fit to a Gaussian function. The FWHM of this Gaussian was defined as the system noise. The reference and the probe noise were measured at between 1.7 % and 3.5%, which is consistent with

a measurement of 18% noise in the diffracted signal; all of these imply laser noise of roughly 2.5% ± 1%. The output of the subtraction circuit was found to have 5.7% noise, which is within experimental uncertainty of the noise expected for the heterodyne term alone. In other words, the circuit has completely removed the reference noise. Based upon observations made during other experiments, the noise in the heterodyne signal exceeds the noise in the diffraction signal when reference subtraction is not performed. It should be noted that these tests were performed with prototype versions of the circuit described above. The prototype circuit employed inferior shielding and the subtraction was performed with a standard op amp subtraction circuit, which only should diminish the circuit performance. The circuit described above will perform slightly better.

IV. Summary

An experimental system has been presented which has been shown to perform near optimal detection of heterodyned transient grating measurements on a femtosecond timescale. This technique is ideal for many ultrafast, time-resolved measurements. It provides wavevector control while maintaining linearity. It provides for optimal signal-to-noise ratios. The optical system is easy to align and it eliminates the "pancake effect", producing much higher wavevector resolution. The detection electronics are shown to still further maximize the signal-to-noise ratio. The range of accessible materials has been greatly expanded to include weakly diffracting samples and samples of poor optical quality. Signals from samples whose responses exhibit multiple frequencies are much clearer and easier to interpret. This is an outstanding way to perform transient grating experiments and it is a powerful tool in the study of nature with short pulses of light.

References

1 J. A. Rogers, M. Fuchs, M. J. Banet, J. B. Hanselman, R. Logan, and K. A. Nelson, Appl. Phys. Lett. **71,** 225 (1997).

2 A. A. Maznev and K. A. Nelson, Opt. Lett. **23**, 1319 (1998).

3 A. A. Maznev, T. F. Crimmins, and K. A. Nelson, Opt. Lett. **23**, 1378 (1998).

4 Y.-X. Yan and K. A. Nelson, J. Phys.Chem. **87,** 6240-6256 (1987).

5 H. A. Haus, *Waves and Fields in Optoeletronics* (Prentice-Hall, Inc., Englewood Cliffs, 1984).

6 A. A. Maznev, personal communication (1997).

7 S. Matsuo and T. Tahara, Chem. Phys. Lett. **264,** 636 (1997).

8 D. W. Pohl, IBM J. Res. Dev. **23,** 604 (1979).

9 Y. J. Chang, P. Cong, and J. D. Simon, J. Phys. Chem. **99,** 7857-7859 (1995).

10 P. Vohringer and N. F. Scherer, J. Phys. Chem. **99,** 2684-2695 (1995).

11 B. C. Baker, Sensors Magazine (1997).

12 C. Brennan, Thesis, Massachusetts Institute of Technology, 1997.

13 D. Paolucci, Thesis, Massachusetts Institute of Technology, 1998.

14 P. A. Anfinrud, personal communication (1997).

Chapter 5. Heterodyned Impulsive Stimulated Raman Scattering of Phonon-Polaritons in $LiTaO_3$ and $LiNbO_3$

I. INTRODUCTION

The low-frequency optic phonons of ferroelectric crystals have been studied extensively because of their roles as soft modes in ferroelectric phase transitions and their importance in nonlinear optical, electro-optical, and piezoelectric properties[1]. The very large dipole moments associated with the soft modes give rise to the characteristically high dielectric constants of ferroelectric crystals in the far-infrared spectral region. They also result in the typically large splittings between longitudinal and transverse optic (LO and TO respectively) phonon frequencies and the strong coupling of the TO modes to far-infrared radiation. This coupling results in strongly mixed vibrational/electromagnetic modes, phonon-polaritons, which propagate through the host crystals at light-like speeds. The characteristic phonon-polariton dispersion properties are illustrated schematically in figure 5.1.

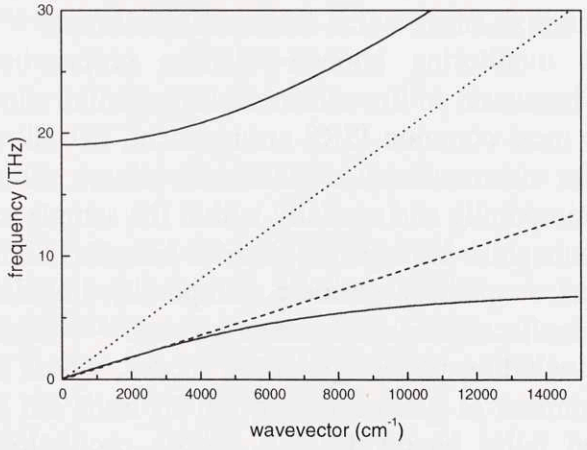

Fig. 5.1. Phonon-polariton dispersion in $LiTaO_3$. The solid lines indicate the upper and lower polariton branches. The dashed and dotted lines describe optical dispersion at low and high frequencies respectively. The lower branch is primarily electromagnetic in character at low wavevectors, and primarily mechanical at high wavevectors.

Careful study of phonon-polariton dispersion can reveal important details of ferroelectric crystal behavior including the progression from underdamped to overdamped response near phase transition temperatures and interactions between the soft mode and other lattice modes. To elucidate the dispersion properties, Raman spectroscopy of phonon-polaritons[2] can be conducted at a range of scattering wavevectors achieved through the use of variable scattering angles, usually in the 1-20 degree range. Extensive studies of $LiTaO_3$ and $LiNbO_3$ have been carried out.[3-14] More recently, impulsive stimulated Raman scattering (ISRS) has been used for phonon-polariton characterization in the time domain.[15-18] ISRS offers the advantages of facile characterization of heavily damped or overdamped responses, good separation of phonon-polariton responses from relaxational responses (which in the frequency-domain light scattering spectrum give rise to central peaks that may overlap with broad low-frequency Raman features), and, as in other coherent Raman scattering methods such as coherent anti-Stokes Raman scattering, excellent wavevector resolution even at very small (<1 degree) scattering angles as well as the capability for monitoring phonon-polariton propagation through the host crystal.[16,17,19-21] In the most common ISRS arrangement, two ultrashort excitation laser pulses are overlapped temporally and spatially within the sample to define the scattering wavevector. They exert a spatially periodic, temporally impulsive driving force on Raman-active modes, including phonon-polariton modes, whose frequencies lie within the coherent excitation pulse bandwidth (i.e. whose oscillation periods exceed the excitation pulse duration). The resulting phonon-polariton oscillations and decay are

observed by coherent scattering (i.e. "diffraction") of variably delayed probe light that is incident at the phase-matching ("Bragg") angle.

ISRS measurements have been conducted on several ferroelectric crystals.[15-18,21-42] Detailed measurements of soft mode behavior near the phase transitions in $KNbO_3$ and $BaTiO_3$ revealed that the soft modes in these materials at all temperatures near the transitions studied were strongly damped or overdamped but distinct from "hopping" or relaxational modes that would be associated with order-disorder rather than displacive phase transition character.[21-23] Careful angle-dependent ISRS measurements of $LiTaO_3$ revealed coupling between the soft mode and several other modes, evident through wavevector-dependent peaks in the signal damping rate[26-28] (analogous to wavevector-dependent anomalous Raman linewidths, but often more easily revealed through the time-domain measurements). Independent measurements of $LiTaO_3$ and also $LiNbO_3$ yielded somewhat different results[18,29-32], which were interpreted in terms of an extremely anharmonic, triple well ferroelectric phonon potential energy surface, of the type first suggested by Lines.[43-45] Important differences between the experimental approaches that yielded conflicting results in these measurements will be discussed below.

In this chapter the results of extensive measurements of the phonon-polariton dispersion properties in $LiTaO_3$ and $LiNbO_3$ are reported using a newly developed optical heterodyne ISRS method.[46-48] The new method couples excellent wavevector resolution with simplification of the form of the data, resulting in unambiguous results for the number and properties of modes that contribute to signal. This simplifies the interpretation of signals from phonon-polaritons since both upper and lower branches as well as multiple modes may be Raman active and may be observed through ISRS

measurements. The present results permit rationalization of the previous, apparently contradictory reports and clarify the nature and number of phonon-polariton modes in the two prototype ferroelectric crystals studied. Additionally, the phase sensitive nature of heterodyne detection permits enhanced observation and characterization of polaritons that have traveled outside of the excitation region

The chapter is organized as follows. Section II provides experimental background that compares different ISRS methods and heterodyne approaches. Section III describes the experimental conditions. Section IV presents measurements of phonon-polariton dispersion properties in $LiTaO_3$ and $LiNbO_3$, with attention focused on the 0-5,000 cm^{-1} wavevector region in which contradictory findings have been reported. In Section V, a detailed theoretical description of the heterodyne detection of propagating responses is presented.

II. BACKGROUND: DIFFERENT ISRS METHODS AND RESULTS

ISRS measurements on phonon-polaritons have been conducted in several different ways. The experiments can be classified roughly by the following criteria.

(1) The two excitation beams are produced through (a) reflective optics or (b) diffractive optics.
(2) The probing beam is incident at (a) the excitation region or (b) a spatially distinct region.
(3) Optical heterodyne detection is (a) used or (b) not used.
(3') When optical heterodyne detection is used, the "reference" field arises from (a) parasitically scattered light or (b) an independently controlled reference beam with adjustable amplitude and optical phase.

In the next sections, a theoretical formulation of the measurements is presented and the effects of the possibilities elaborated above can be seen quantitatively. However the

qualitative effects can be appreciated readily through consideration of the following factors.

(1) As presented in Chapter 4.I(i), when a beamsplitter is used to produce two pulses that are subsequently crossed at a sample, the region of spatial overlap is limited to a narrow volume that is often substantially smaller than that determined by the spot sizes. Since the ISRS scattering wavevector is determined by this transverse extent of this interference pattern, the wavevector is better defined when diffractive optics are used. Use of a beamsplitter results in a far broader excitation wavevector range.

(2) When reflective optics are used for the excitation pulses, resulting as described above in a small excitation region with relatively few interference fringes, there may be some incentive to make measurements with the probe beam translated laterally away from the excitation region instead of overlapped spatially with it since the counterpropagating polariton waves may leave this region after a short time[18]. For wavevector regimes with high polariton group velocity and low damping rate, in which the polariton wave can propagate into and through a spatially distinct probing region without too much damping, this effectively doubles the total temporal range over which the polariton wave can be observed since polariton entry into as well as departure from the probing region are monitored, as illustrated in Fig. 5.2. If optical heterodyne detection is used, this doubles the number of oscillations observed and therefore improves the accuracy of frequency measurement. With diffractive optics, very large excitation regions (substantially exceeding the region over which the phonon-polaritons will propagate before being substantially damped away) can be achieved. In this case, there are only two possible incentives to conduct the

measurements with the probe beam at regions distinct from the excitation area: first, small excitation beam spot sizes may be needed if the pulse fluence of a spatially broad beam is insufficient to generate a detectable polariton response, or second, if accurate measurements of polariton damping are desired in wavevector regions of low damping and high polariton group velocity. It is still possible to probe at distinct regions, if necessary by using small excitation spot sizes so that there is significant phonon-polariton propagation outside the excitation region.

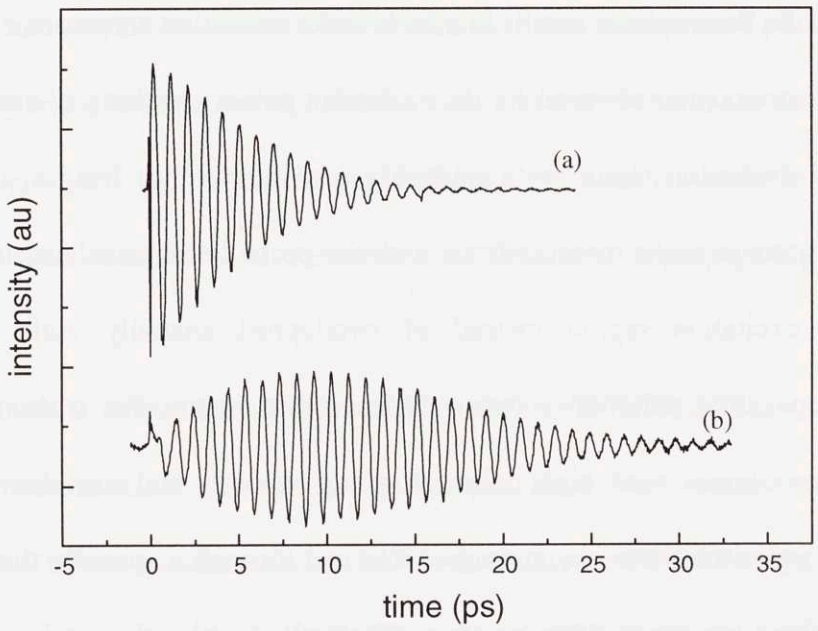

Fig. 5.2. Heterodyne detection of propagating responses with the probe beam overlapping the excitation area (a), and displaced from the excitation area by 1 mm (b). The amplitude of the signal in (a) is twice that in (b), but the number of resolvable oscillations is greater in (b).

(3) Without optical heterodyne detection, ISRS signals are proportional to the square of the vibrational displacements[49]. Heterodyne detection can linearize this dependence, in some cases simplifying interpretation of the data[50]. If probing is conducted away from the excitation region, then without heterodyne detection one would expect to see simply a gradual time-dependent rise and fall of signal as the propagating phonon-

polariton wavepacket enters and passes through the probing region. With heterodyne detection, one expects to see individual oscillation cycles in the signal, since the optical phase of the coherently scattered field shifts by 180 degrees each time the phonon-polariton wavepacket moves by half its wavelength while the phase of the reference field is unshifted.

(3') The form of the signal in any optical heterodyne measurement depends on the relative amplitudes and phases of the signal and the reference fields. In general, it is useful to adjust the reference field amplitude and phase such that constructive interference with the signal field and the signal/noise level are optimized. This is straightforward if there is a reference beam generated experimentally whose amplitude and optical phase are readily controlled. If the reference field arises from parasitically scattered light, then the form of the data may depend on variables like the probe location, since the amplitude and optical phase of the reference field will vary from one sample region to another.

Qualitative illustration of some of the effects described above is provided in figs. 5.3-5.6. Figures 5.3 and 5.4 show results obtained with the probe beam completely overlapping the excitation region. Figure 5.3 shows data collected with the reference beam equal in intensity to the probe beam at several different reference phases. At reference phases of 0 and 180 degrees, the heterodyne term dominates and the data follow the form of a simple damped sine wave. Figure 5.4 shows data collected with a reference beam intensity one one-hundredth that of the probe beam at a variety of phases. In this case, the diffraction and heterodyne term are roughly equal and the data is seen to have one contribution oscillating and damping at twice the material response rate and another

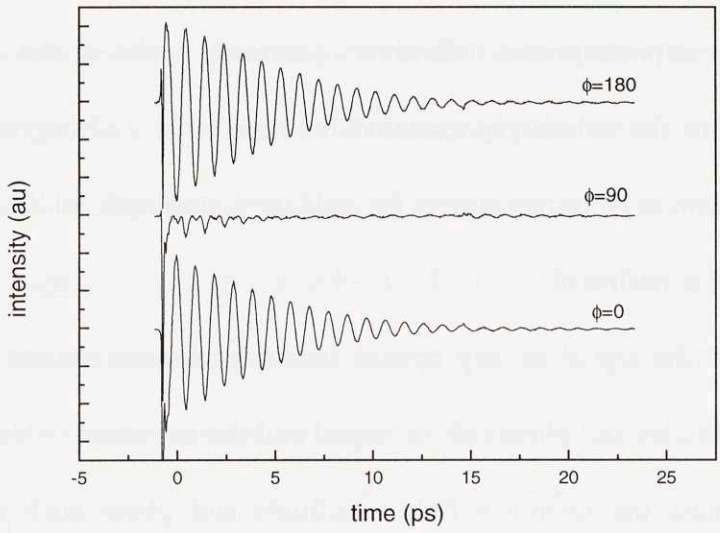

Fig. 5.3. Heterodyne ISRS of $LiTaO_3$ with the probe beam overlapping the excitation area and with the amplitude of the reference beam much greater than that of the diffracted beam. The amplitude of the signal varies as a function of the reference beam phase.

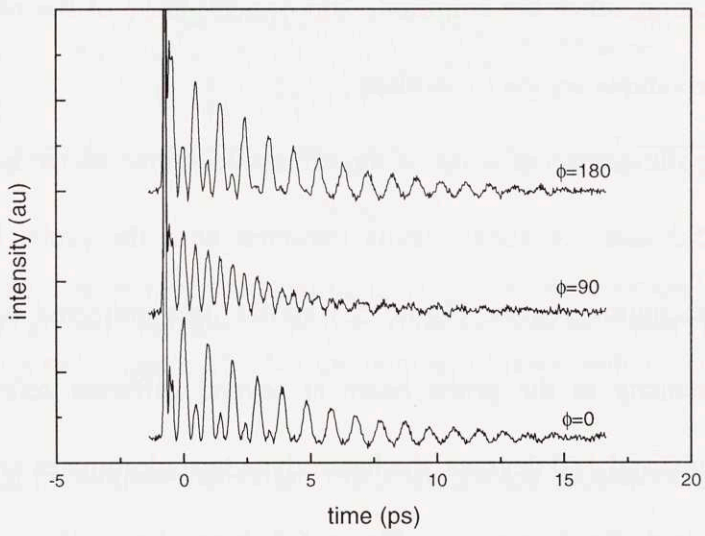

Fig. 5.4. Heterodyne ISRS of $LiTaO_3$ with the probe beam overlapping the excitation area and with the amplitude of the reference beam roughly equal to that of the diffracted beam. Oscillations at the fundamental and second harmonic of the material response frequency are observed. The amplitude of the heterodyne component of the signal varies as a function of reference phase.

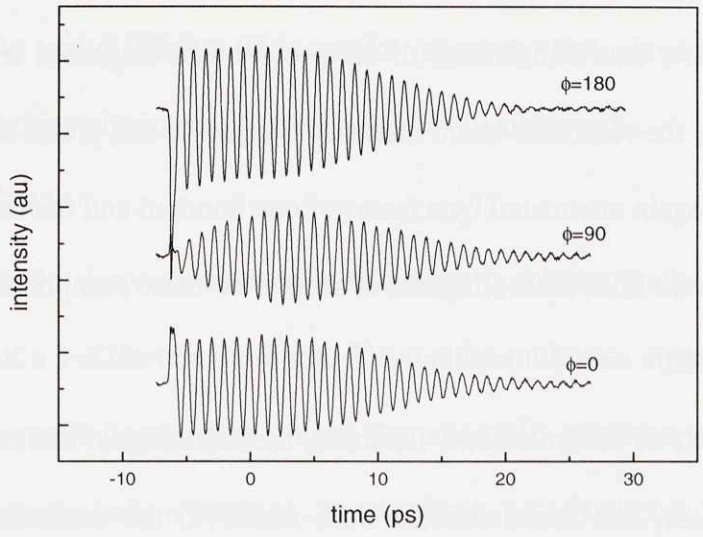

Fig. 5.5. Heterodyne ISRS of $LiTaO_3$ with the probe beam displaced 500 μm from the excitation area and with the amplitude of the reference beam much greater than that of the diffracted beam. At early times, the amplitude of the signal is a function of the optical phase of the reference beam, while at later times, the phase of the signal oscillations is a function of the reference beam phase.

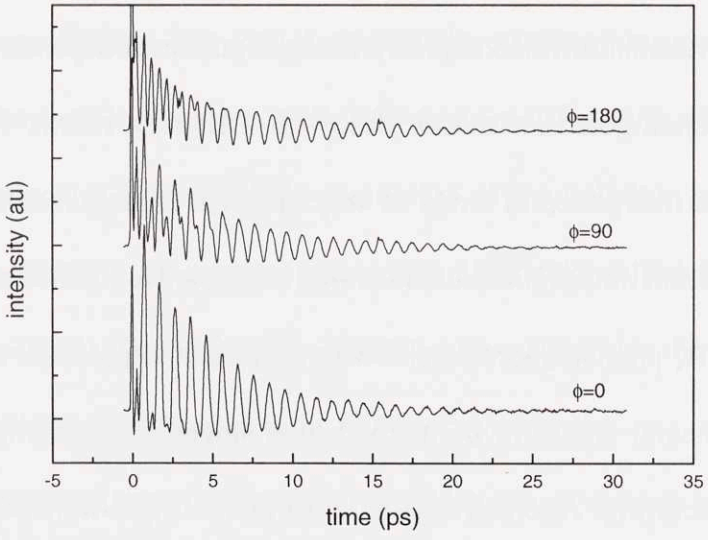

Fig. 5.6. Heterodyne ISRS of $LiTaO_3$ with the probe beam displaced 500 μm from the excitation area and with the amplitude of the reference beam roughly equal to that of the diffracted beam. A substantial component of diffracted signal is present at early times.

contribution whose dynamics are linearly related to those of the material response. Figures 5.5-5.6 show data collected with the probe beam displaced from the excitation region. In Fig. 5.5, the reference beam intensity is equal to the probe beam intensity and in Figure 5.6, it is again attenuated by a factor of one hundred and the data are collected at a variety of phases. In both cases, the data is seen to be more complicated than a damped sinusoidal oscillation.

As these sets of measurements illustrate, the ISRS signal and its power spectrum take on the simplest, and most accurate form when (1) the excitation region is large giving rise to many oscillations, (2) the probe spot overlaps the center of the excitation region, (3) optical heterodyne detection is used, and (3') the reference beam amplitude substantially exceeds that of the signal field and the reference beam phase is adjusted for maximized constructive interference with the signal field.

The interpretation of ISRS data at a fundamental level depends on the number of nature of the phonon-polariton modes observed. Different results from $LiTaO_3$ and $LiNbO_3$ have been interpreted in terms of very different models for the lattice potential energy surface. Recent *ab initio* calculations find a double-well lattice potential along the lowest frequency A_1 phonon coordinate,[51] with a substantial potential energy barrier and no direct experimental signature of more than a single minimum in which coherent oscillations are occurring. Alternatively, an anharmonic triple-well potential model has been used,[18,43-45,52] which was first postulated by Lines based upon work by Johnston and Kaminow[3] and was later reinforced by neutron scattering studies performed by Abrahams *et al.*[53] Based upon this three-well model, Bakker *et al.*[31] posited the existence of a 32 cm^{-1} tunneling resonance in $LiTaO_3$ to explain the appearance of several

frequency components at various wavevectors in ISRS data from the lowest frequency A_1 modes of $LiTaO_3$ and $LiNbO_3$. This model suggests that, in some cases, direct experimental signatures of triple-well potentials may be observed.

III. EXPERIMENTAL

The experimental apparatus used in this work is schematically depicted in figure 4.10. The output of a 1-KHz repetition rate Ti:sapphire multipass amplifier was used for the pump and the probe beams. The output was spectrally centered at 800 nm and the pulses were 40 femtoseconds in duration. The vertically polarized pump and probe beams were separated with a beamsplitter, passed through the experimental setup shown in figure 4.10, and focused onto the sample. The co-propagating diffracted light and the reference beam were sent into a photodiode and the resulting current pulse was amplified and then detected with a lock-in amplifier. The pump and probe beams contained 10 microjoules and significantly less than 1 microjoule of energy respectively. The beam spatial profile in the sample plane was well fit by a gaussian function with FWHM of 600 microns in the horizontal dimension (the dimension of the polariton wavevector) and a FWHM of 130 microns in the vertical dimension. Diffraction efficiencies of around 1 percent were observed. The reference intensity was equal to the probe intensity, producing a heterodyne amplification ratio, I_H / I_D of twenty.

In the experiments described below, 1mm thick, single domain samples of $LiTaO_3$ and $LiNbO_3$ were used. The crystals were x-cut and polished to optical quality. The z axis of the crystal, or the direction of the ferroelectric polarization, was oriented along the direction of the excitation and probe fields' polarization.

IV. HETERODYNE ISRS RESULTS FROM $LiTaO_3$ AND $LiNbO_3$

Heterodyne ISRS data taken were taken at many wavevectors in both $LiTaO_3$ and $LiNbO_3$ from A_1 phonons excited and probed in (ZZ) geometry. Data from wavevectors around the previously reported tunneling resonance[29] are shown in fig. 5.7 for $LiTaO_3$. The power spectra of the polariton response at all points in this wavevector range are well fit by a single lorentzian lineshape function. A peak in the frequency domain response is observed at 0.92 ± 0.02 THz , which falls, within experimental error, in the previously reported frequency gap[29] which was assigned as an avoided crossing between the phonon-polariton and a tunneling resonance. Throughout the entire wavevector range studied in $LiNbO_3$, all power spectra could be well fit by a single lorentzian lineshape function. No evidence of avoided crossings was observed in this work for either $LiTaO_3$ or $LiNbO_3$ and the previously reported polariton beats[18,29-32] were not reproduced.

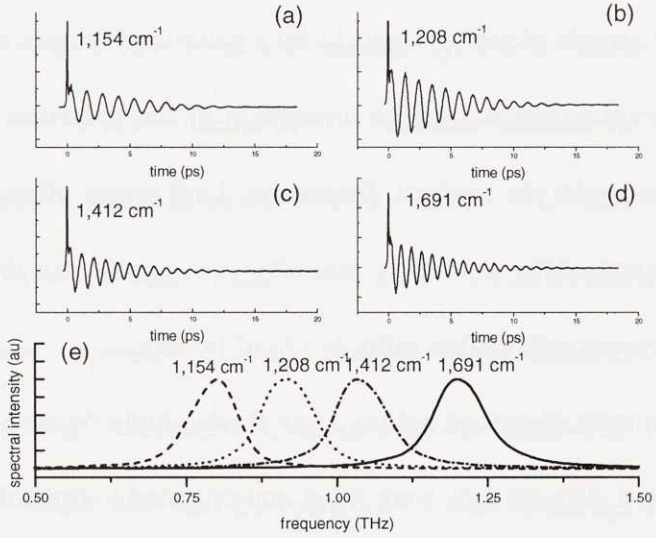

Fig. 5.7. Heterodyne ISRS measurements of the dispersive A_1 polariton in $LiTaO_3$ around 1 THz, (a)-(d). In (e), the power spectra of these data are shown. No beating patterns are observed in the time domain data and single peaks are observed in the power spectra which are well fit by single Lorentzian lineshapes.

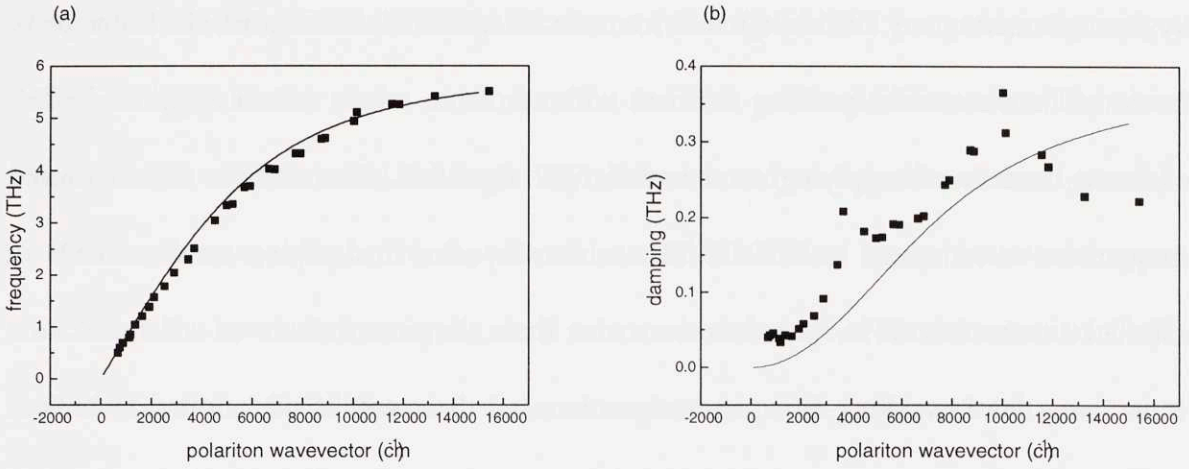

Fig. 5.8. Complex dispersion of the lowest frequency A_1 phonon in $LiTaO_3$. (a) The real part of the dispersion (squares) is plotted along with the theoretically predicted dispersion relation (solid line). (b). The imaginary part of the dispersion (squares) along with the theoretically predicted dispersion relation (solid line). All material parameters used in calculating the theoretical results were taken from literature. A single frequency below 6 THz was observed at all wavevectors.

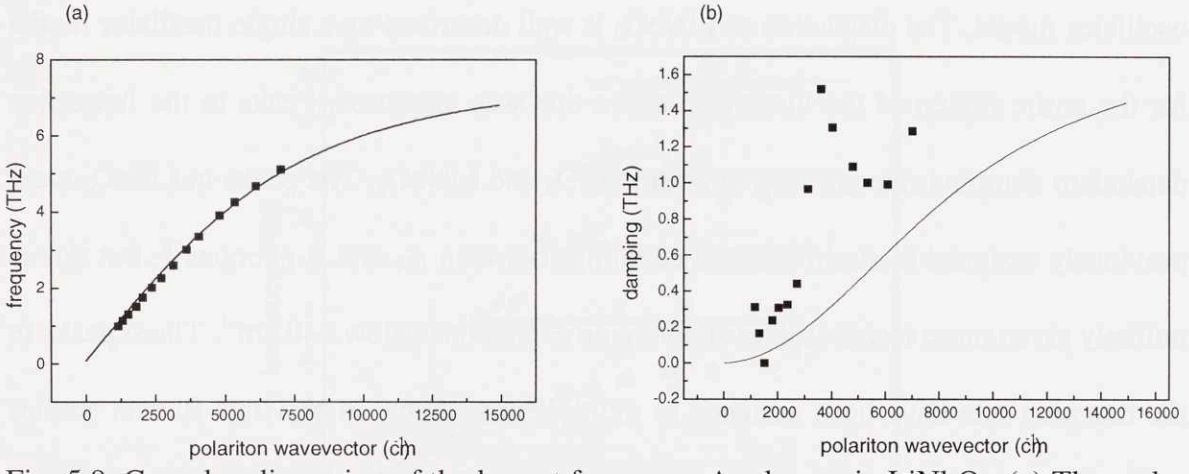

Fig. 5.9. Complex dispersion of the lowest frequency A_1 phonon in $LiNbO_3$. (a) The real part of the dispersion (squares) is plotted along with the theoretically predicted dispersion relation (solid line). (b). The imaginary part of the dispersion (squares) along with the theoretically predicted dispersion relation (solid line). All material parameters used in calculating the theoretical results were taken from literature. A single frequency below 6 THz was observed at all wavevectors.

The dispersion and frequency dependent damping from this work are shown in figures 5.8 and 5.9. The frequencies and damping rates were obtained from fitting the power spectrum of the data to a lorentzian lineshape. The power spectrum was obtained

by first subtracting any DC background from the data, second deleting the electronic peak from the data set, third packing the data with zeroes to create a data array of 32,768 elements, and fourth applying a numerical FFT algorithm. The error in the measured frequencies is estimated to be 0.02 THz while the error in damping measurements is estimated to be 0.1 THz. The data were also fit in the time domain to a damped sine wave using the Levenburg-Marquardt algorithm, but these results were found to be less accurate than the power spectrum fit described above (see appendix 5A). The wavevector was determined by measuring the angle between pump beams using reflections from the crystal surface and a precision rotation stage. The uncertainty in wavevector is estimated to be 1 percent. The dispersion of $LiTaO_3$ is seen to be well described by a single oscillator model. The dispersion of $LiNbO_3$ is well described by a single oscillator model for the entire region of the dispersion curve that was measured. Peaks in the frequency dependent damping rate are seen in both $LiTaO_3$ and $LiNbO_3$. The peaks in $LiTaO_3$ were previously assigned to strain induced couplings between A_1 and E phonons[28], but this is unlikely given more recent studies showing no E phonons below 140 cm^{-1}. These peaks in the damping rate have been assigned to multiphonon effects in previous Raman studies based upon their temperature dependent intensities [10,54]. It should be emphasized that these multiphonon effects are not related to the resonances reported in reference[18,29-32]. The damping rates, measured from the peak widths in the data's power spectrum, appear to be anomalous below 2,000 cm^{-1}

Previous time domain studies have observed only a single polariton branch in these crystals, primarily because an increasingly short pulse duration is required to excite and probe higher frequency responses. The need is exacerbated without heterodyne

detection since the oscillations in the data are at twice the phonon frequency, requiring a correspondingly shorter probe pulse duration for time-resolved observation. The short pulse duration used here and the sensitivity of the heterodyne detection make it possible to observe three nondispersive A_1 phonon modes in addition to the lower and upper branches of the lowest frequency A_1 mode across a broad range of wavevectors in $LiTaO_3$ as shown in figure 5.10. Note that the measurement provides access to each successive higher-frequency branch with a successively higher minimum wavevector. This effect arises due to the forward wavevector component of the excitations, which increases with increasing frequency and with increasing phase velocity.[55] The identical wavevector restrictions arise in conventional Raman spectroscopy of phonon-polaritons.[56]

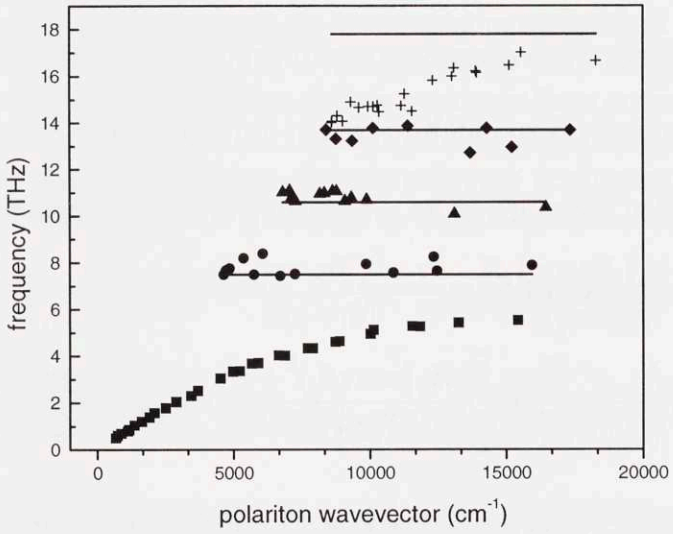

Fig. 5.10. Multiple A_1 phonon branches observed in $LiTaO_3$. Four phonon branches, including three non-dispersive phonons (circles, triangles, and diamonds) and the upper (plus sign) and lower (squares) branch of the dispersive phonon, are shown. The solid lines are the frequencies of the higher phonon branches reported in literature. The wavevector offset in the higher lying phonon branches is a result of the fact that the forward wavevector component becomes much more important at higher frequencies.

V. THEORETICAL TREATMENT OF HETERODYNED ISRS DETECTION OF PROPAGATING RESPONSES

In order to describe the heterodyned ISRS signal observed from propagating responses, it is important to treat the polariton as a propagating wavepacket generated by the non-linear interaction between two laser pulses with finite (Gaussian) spatial profiles. This wavepacket is then detected by a probe pulse with a Gaussian spatial profile which has been offset from the center of the excitation region. The theoretical approach of Siegmann[57], followed closely in description of ISS experiments on propagating acoustic modes[19], will be followed here as well.

ISRS will be broken down into two distinct steps: polariton generation and detection. Both the excitation and the probe beams will be treated in the CW limit, which introduces no difficulties when describing experiments using diffractive optics. Extension to the case of pulsed lasers is straightforward but it unnecessarily complicates the results. The field of a Gaussian excitation pulse propagating at a small angle to the z axis may be written in the usual approximation as

$$E_e(x,y,z,t) \cong E_e^0\left(\frac{1}{z+ib_e}\right)\exp\left[\frac{-ik_e\left(x-z\theta_e\right)^2+y^2}{2\left(z+ib\right)}-ik_e\left(z-\frac{z\theta_e^2}{2}+x\theta_e\right)\right]\exp\left(i\omega_e t\right) \quad (5.1)$$

where k_e is the excitation wavevector, $b = k_e w_0^2 / 2$ is the confocal parameter, and w_0 is the minimum Gaussian beam radius. If two excitation beams of slightly different frequency ω_e overlap in the sample center and drive a phonon response at the difference frequency, the spatial profile of the two-beam interference pattern is given by

$$g(x,y,z)=\frac{1}{2}\left[E_e(\theta_e)E_e^*(-\theta_e)+E_e^*(\theta_e)E_e(-\theta_e)\right] \tag{5.2}$$

where the fields have been written as functions of incident angle for notational convenience. For non-oscillatory responses, the spatial profile of this interference pattern is mapped directly onto the spatial profile of the material response. For oscillatory responses, the spatial profile of the material response acquires a forward wavevector component because of the phase lag between oscillations at the front and rear of the sample caused by finite light propagation speeds.[55] Because a probe beam with the same propagation speed that is phase matched for Bragg diffraction will experience a constant material response phase as it propagates through the sample[15], the forward wavevector component will be suppressed in this treatment. The optical grating derived can be interpreted as the effective grating existing for a probe pulse incident at the Bragg angle. Finally, only the second term of equation (5.2) is important for a probe beam incident at θ_p and detected at $-\theta_p$. The important part of the interference grating may thus be written

$$g(x,y,z)=\left|E_e^0\right|^2\frac{1}{w_e(z)}\exp\left[\frac{-ik_e\left(x+z\theta_e\right)^2+y^2}{2\left(z+ib\right)}+\frac{ik_e\left(x-z\theta_e\right)^2+y^2}{2\left(z-ib\right)}+i2k_e\theta_e x\right] \tag{5.3}$$

where $w^2(z)=2b_e/k_e\left(1+z^2/b^2\right)$. The length of overlap between the excitation pulses in the z dimension is roughly given by $l\approx w_0/\theta_e=\pi w_0^2/N_f\lambda$ which is shorter than the Rayleigh range $\pi w_0^2/\lambda$ by ~N_f times, where N_f is the number of fringes produced by crossing two CW beams or two pulses split with diffractive optics and recombined as described in chapter IV. It can therefore be assumed that the excitation and probe beams are collimated through the sample region and the grating will assume the simplified form

$$g(x,y,z)=\left(\frac{k_e b_e}{\pi}\right)\frac{1}{w_e}\exp\left[\frac{-2\left(x^2+y^2+\theta_e^2 z^2\right)}{w_e^2}+i2k_e\theta_e x\right] \tag{5.4}$$

where w_e=$w(0)$. The extension to the pulsed laser case will change (5.4) in two ways. First, there will be a convolution over the bandwidth of both excitation pulses that will affect the overall intensity of the grating. Second, if reflective optics are used to split the excitation beam, the spread of the grating in the x dimension will be reduced by the "pancake effect".

When the two excitation beams are crossed in a nonlinear medium the grating pattern described in equation (5.4) will be mapped onto the spatial profile of the material displacements $Q(x,y,z)$ and the dielectric constant $\tilde{\varepsilon}_{NL}$ through impulsive stimulated scattering, and the material response will linearly alter the complex dielectric constant of the sample, creating an optical grating. For the purposes of this work, the proportionality between the interference grating and the material displacement can be expressed with a phenomenological constant G_E, which is related to the differential polarizability of the mode.[24,55] It will be assumed initially that the material response is static; propagation effects will be introduced below. The small change in the dielectric constant $\tilde{\varepsilon}_{NL}$ has the same spatial profile as the interference grating

$$\tilde{\varepsilon}_{NL}(x,y,z)=\varepsilon\chi_m Q(x,y,z)=\varepsilon\chi_m G_E g(x,y,z) \tag{5.5}$$

and it is detected via diffraction of a third, probe beam arriving at an angle θ_p which illuminates the volume grating, generating a nonlinear polarization p_{NL}

$$p_{NL}(x,y,z)=\chi_m\varepsilon G_E g(x,y,z)E_p(\theta_p) \tag{5.6}$$

where the probe electric field E_p takes has the form of equation (5.1). Both equations (5.5) and (5.6) are nonzero only inside the sample volume.

The electric field of the scattered probe can be determined from the paraxial wave equation

$$\left(\frac{\partial^2}{\partial x^2}+\frac{\partial^2}{\partial y^2}-2ik_p\frac{\partial}{\partial z}\right)E_D(x,y,z)=-\omega_p^2\mu_0 p_{NL}(x,y,z) \tag{5.7}$$

where the nonlinear polarization acts as a source term on the right-hand side. One approach to solving equation (5.7) involves first defining the transverse fourier transform of the nonlinear polarization $\tilde{p}_{NL}\left(s_x,s_y,z\right)$

$$\tilde{p}_{NL}\left(s_x,s_y,z\right)=\int_{-\infty}^{\infty}\int_{-\infty}^{\infty}p_{NL}\left(x,y,z\right)\exp\left(i2\pi s_x x+i2\pi s_y y\right)dxdy \tag{5.8}$$

with a similar transform for the scattered electric field. The paraxial equation can be transformed and integrated along the z dimension to give the transformed solution in the far field limit for a sample of length L

$$\tilde{E}_D\left(s_x,s_y,z\right)=-i\left(\frac{\omega_p^2\mu}{2k_p}\right)\exp\left(i\pi\lambda_p s^2 z\right)\int_{-L/2}^{L/2}\exp\left(-i\pi\lambda_p s^2 z'\right)\tilde{p}_{NL}(s_x,s_y,z')dz' \tag{5.9}$$

where $s^2=s_x^2+s_y^2$ .The transformed nonlinear polarization may be written as the two dimensional convolution of the transformed optical grating and probe electric field

$$\tilde{p}_{NL}(s_x,s_y,z)=\chi_m\varepsilon G_E\tilde{g}(s_x,s_y,z)\otimes\tilde{E}_p\left(s_x,s_y,z\right) \tag{5.10}$$

The transform of the grating and the spatial profile of the probe are

$$\tilde{g}(s_x,s_y,z)=\frac{\pi}{2}\left|E_e^0\right|^2\exp\left[\frac{-w_e^2}{8}\left(2\pi s_x+2k_e\theta_e\right)^2\right]\exp\left[-\frac{\left(2\pi s_y\right)^2 w_e^2}{8}\right] \tag{5.11}$$

$$\tilde{e}_p(s_x,s_y,z)=\pi E_p^0\exp\left(\frac{ik_pz\theta_p^2}{2}\right)\exp\left[-\left(2\pi s_x-k_p\theta_p\right)^2\frac{w_p^2}{4}\right]$$
$$\exp\left[-\frac{\left(2\pi s_y\right)^2w_p^2}{4}\right] \tag{5.12}$$

where terms which vary slowly along the z coordinate over the distance L (which will contribute almost nothing to the integral in equation (5.9)) have been neglected. At this point, the effects of response propagation and displacement of the probe from the center of the excitation region can be easily introduced. In the case of phonon-polaritons and other propagating excitations in which two, counter-propagating wavepackets are excited via ISRS, the dynamic grating may be written

$$g\left(x,y,z,t\right)=-\left[g\left(x+vt,y,z\right)-g\left(x-vt,y,z\right)\right] \tag{5.13}$$

where v is the group velocity of the polariton wavepacket. Similarly, horizontal displacement of the probe beam can be accounted for by changing x to x-d in equation (5.1). The transforms of these new functions can be determined by applying the fourier shift theorem to equations (5.11) and (5.12), yielding

$$\tilde{g}(s_x,s_y,z)=-\frac{\pi}{2}\left|E_e^0\right|^2\exp\left[\frac{-w_e^2}{8}\left(2\pi s_x+2k_e\theta_e\right)^2\right]\exp\left[-\frac{\left(2\pi s_y\right)^2w_e^2}{8}\right] \tag{5.14}$$
$$\times\left[\exp\left(i2\pi s_xvt\right)-\exp\left(-i2\pi s_xvt\right)\right]$$

$$\tilde{e}_p(s_x,s_y,z)=\pi E_p^0\exp\left(\frac{ik_pz\theta_p^2}{2}\right)\exp\left[-\left(2\pi s_x-k_p\theta_p\right)^2\frac{w_p^2}{4}\right]$$
$$\times\exp\left[-\frac{\left(2\pi s_y\right)^2w_p^2}{4}\right]\exp\left(i2\pi s_xd\right) \tag{5.15}$$

Equations (5.14) and (5.15) are convolved and inserted into (5.10) to obtain the transform of the nonlinear polarization

$$\tilde{p}_{NL}\left(s_x,s_y,z\right)=-\frac{4\pi^3}{w_e^2+2w_p^2}\chi_m\varepsilon G_E\left|E_e^0\right|^2E_p^0\exp\left(\frac{-2v^2t^2}{w_e^2}-\frac{d^2}{w_p^2}\right)\exp\left(idk_p\theta_p\right)$$
$$\left\{\exp\left[-\frac{w_e^2w_p^2}{4\left(w_e^2+2w_p^2\right)}\left(2\pi s_x+2k_e\theta_e-k_p\theta_p-\frac{i4vt}{w_e^2}-\frac{i2d}{w_p^2}\right)^2\right]\exp\left(-ivt2k_e\theta_e\right)\right.$$
$$\left.-\exp\left[-\frac{w_e^2w_p^2}{4\left(w_e^2+2w_p^2\right)}\left(2\pi s_x+2k_e\theta_e-k_p\theta_p+\frac{i4vt}{w_e^2}-\frac{i2d}{w_p^2}\right)^2\right]\exp\left(ivt2k_e\theta_e\right)\right\} \tag{5.16}$$
$$\exp\left[-\frac{w_e^2w_p^2}{4\left(w_e^2+2w_p^2\right)}\left(2\pi s_y\right)^2\right]\exp\left(\frac{ik_pz\theta_p^2}{2}\right)$$

The nonlinear polarization will radiate a diffracted field in the direction set by conservation of the x component of the wavevector. Equation (5.16) is proportional to the field diffracted from a thin grating at position z in the sample. Integration along the sample depth, as expressed in equation (5.9), will impose a conservation of the z component of the wavevector which grows gradually stricter as the sample thickness is increased. This produces the familiar Bragg angle phase matching condition for thick gratings, which is expressed below as a filter $F(\theta_p,s_x)$ imposed on the nonlinear polarization and, consequently, on the diffracted field:

$$\tilde{E}_D\left(s_x, s_y, z \to \infty\right) = iA\exp\left(\frac{-2v^2t^2}{w_e^2} - \frac{d^2}{w_p^2}\right)\exp\left(idk_p\theta_p\right)$$
$$\left\{\exp\left[-w\left(2\pi s_x + 2k_e\theta_e - k_p\theta_p - \frac{i4vt}{w_e^2} - \frac{i2d}{w_p^2}\right)^2\right]\exp\left(-i\omega_0 t\right)\right.$$
$$\left.-\exp\left[-w\left(2\pi s_x + 2k_e\theta_e - k_p\theta_p + \frac{i4vt}{w_e^2} - \frac{i2d}{w_p^2}\right)^2\right]\exp\left(i\omega_0 t\right)\right\} \qquad (5.17)$$
$$\exp\left[-w\left(2\pi s_y\right)^2\right]F\left(\theta_p, s_x\right)P(z)$$

$$A = \frac{8\pi^3}{w_e^2 + 2w_p^2}\chi_m\varepsilon G_E\left(\frac{\omega_p^2\mu}{2k_p}\right)E_p^0\left|E_e^0\right|^2$$

$$F\left(\theta_p, s_x\right) = \frac{-4k_e\sin\left\{\frac{\left[\left(2\pi s\right)^2 - k_p^2\theta_p^2\right]L}{4k_p}\right\}}{\left(2\pi s\right)^2 - k_p^2\theta_p^2}$$

$$P(z) = \exp\left\{-i\left[k_p - \frac{\left(k_x^2 + k_y^2\right)}{2k_p}\right]z\right\}$$

$$w = \frac{w_e^2 w_p^2}{4\left(w_e^2 + 2w_p^2\right)}$$

$$\omega_0 = v2k_e\theta_e$$

The two bracketed exponents describing the s_x distribution contain real terms, which describe the direction in which the diffracted beam propagates (this expresses the x coordinate conservation), and imaginary terms which describe the position of the beam center along the x coordinate of position space. It is clear that ω_0 is the material response frequency and $P(z)$ is the z component of the wavevector which varies with s_x and s_y in

order to satisfy the requirement that $k_p^2 = k_x^2 + k_y^2 + k_z^2$. The diffraction and heterodyne terms can be determined from equation (5.17). The signal measured at the detector is proportional to the power contained in the respective fields, where power is defined as the time averaged magnitude of the complex Poynting vector integrated over s_x and s_y. Assuming that the probe beam is reasonable well collimated and is incident at the Bragg angle, and that the sample is not extremely thick (more specifically, that the condition $L >> \frac{(2k_e\theta_e)^2\sqrt{\varepsilon_0}}{2\pi\lambda_p}$ does not hold), the filter function is approximately equal to unity at all significant wavevectors and it can be ignored. The power in the diffracted field is given by

$$P_D = A'\exp\left[-\frac{4(vt-d)^2}{w_e^2+2w_p^2}\right] + A'\exp\left[-\frac{4(vt+d)^2}{w_e^2+2w_p^2}\right] \\ -2A'\exp\left(\frac{-4d^2}{w_e^2+2w_p^2}\right)\exp\left(\frac{-4v^2t^2}{w_e^2+2w_p^2}\right)\cos(2\omega_0 t) \tag{5.18}$$

where

$$A' = \frac{\chi_m \varepsilon G_E \left(\frac{\omega_p^2\mu}{2k_p}\right) I_p^0 \left|I_e^0\right|^2}{w_e^2 w_p^2}$$

The first two terms represent the detection of traveling waves outside of the excitation area. These terms exhibit no oscillations and are at a maximum at the point in time when the wavepacket center coincides with center of the probe beam. The final term describes the detection of the standing wave in the excitation region. This term is reduced with time as the wavepackets propagate outside of the excitation area, it is reduced if the probe beam is displaced from the center of this region, and it oscillates at twice the material

response frequency. When the probe beam overlaps the excitation area, i.e., d=0, equation (5.18) simplifies to

$$P_D = 4A' \exp\left[-\frac{4v^2t^2}{w_e^2 + 2w_p^2}\right] \sin^2(2\omega_0 t) \tag{5.19}$$

as expected. The ratio between the amplitude of signals detected at d=vt=0 and d=vt~∞ is 4:1. The contribution of the heterodyne term, with a reference field

$$\begin{aligned} \tilde{E}_R(s_x, s_y, z) &= E_R^0 \exp\left(\frac{-d^2}{w_p^2}\right) \exp\left(idk_p\theta_p\right) \exp\left[-w\left(2\pi s_y\right)^2\right] \\ &\exp\left[\frac{-w_p^2}{4}\left(2\pi s_x + 2k_e\theta_e - k_p\theta_p - \frac{i2d}{w_p^2}\right)^2\right] \exp(i\varphi) P(z) \end{aligned} \tag{5.20}$$

to the total power, at any position along the z dimension, is

$$\begin{aligned} P_H &= \frac{1}{2}\sqrt{\frac{\varepsilon}{\mu}} \operatorname{Re}\left[E_D E_R^* + E_D^* E_R\right] = \frac{1}{2}\sqrt{\frac{\varepsilon}{\mu}} \int_{-\infty}^{\infty} \int_{-\infty}^{\infty} \operatorname{Re}\left[E_D E_R^* + E_D^* E_R\right] ds_x ds_y \\ &= A'' \left\{ \exp\left[\frac{-2(vt-d)^2}{w_e^2 + w_p^2}\right] \sin(\omega_0 t + \varphi) + \exp\left[\frac{-2(vt+d)^2}{w_e^2 + w_p^2}\right] \sin(\omega_0 t - \varphi) \right\} \end{aligned} \tag{5.21}$$

where

$$A'' = \frac{-8}{w_p^2}\sqrt{\frac{2}{w_e^2\left(w_e^2 + w_p^2\right)}} \chi_m \varepsilon G_E\left(\frac{\omega_p^2 \mu}{2k_p}\right) I_e^0 \sqrt{I_p^0 I_R^0}$$

In the limit that d=0 or vt=0, equation (5.21) reduces to

$$P_H = -2A'' \left\{ \exp\left[-\frac{2(\xi)^2}{w_e^2 + w_p^2}\right] \sin(\omega_0 t) \cos\varphi \right\} \tag{5.22}$$

where $\xi = vt$ for the case that d=0 and $\xi = d$ for the case that vt=0. The two counter-propagating polaritons produce a standing wave in the excitation area at early times and at zero probe displacement which oscillates at the material response frequency, as described

by equation (5.22). The amplitude of this expression is a function of the reference phase, and it has a value of $2A''$ when $\varphi = 0°, 180°$. When the two wavepackets are detected after having propagated outside of the excitation area, there is no longer any substantial interference between them and only one of the two terms in equation (5.21) contributes. The phase of the oscillations of this term is a function of the reference beam phase; the amplitude is A'' for all reference phases. When the probe beam partially overlaps the excitation area the amplitude of the early time signal and the phase of the oscillations in the late time signal will be a function of the reference beam phase. Consequently, at a range of reference beam phases, the phase of the observed oscillations will shift with time, even though the underlying material response creating the signal is entirely linear and has a constant phase. This can produce a distortion of the power spectrum of the signal when $d \neq 0$ and artificially alter measurements of frequency and damping based on lineshape analysis. It must be emphasized, however, that these types of effects do not appear to be able to reproduce the results of ref. [18,29-32], in which multiple peaks were observed in the power spectrum, not mere distortions. It should also be noted that the exponential decay factors describing response propagation outside of the probe beam area are slightly different in equations (5.19) and (5.21), with the apparent damping produced by response propagation being equal to

$$\Gamma_P^D = \frac{4}{w_e^2 + 2w_p^2} \tag{5.23}$$

for the diffraction term and

$$\Gamma_P^H = \frac{2}{w_e^2 + w_p^2} \tag{5.24}$$

for the heterodyne term. The overall factor of 2 difference between the two damping terms clearly results from the fact that the diffraction and heterodyne terms are quadratically and linearly related to the material response, respectively. The difference in the denominators is explained by the fact that the center of a beam produced by diffraction from a propagating response shifts in time, reducing the overlap between the diffracted and reference fields at later times and increasing the apparent damping.

VI. CONCLUSION

A new optical apparatus has been used to perform heterodyne ISRS measurements of the complex dispersion of phonon-polaritons in lithium tantalate and lithium niobate. This apparatus greatly simplifies and improves the optical heterodyne detection of light diffracted from transient gratings by providing for facile experimental alignment, controllable reference beam (local oscillator) intensity and phase, and by markedly increasing the potential wavevector resolution. Heterodyne detection is shown to enhance ISRS: the form of the data is simplified, especially when multiple frequencies are present; signals can be optically amplified leading to improved sensitivity; and, phase information can be obtained about responses which have propagated outside of the excitation area. A theoretical analysis of the heterodyne detection of propagating responses is presented and it is shown that frequency and damping measurements that rely upon either time domain fits to damped sine waves or power spectrum fits to Lorentzian lineshapes are most accurate when the response is probed either completely within the excitation area, or at late times after the two counter-propagating responses have traveled far enough apart that there is no substantial overlap between them.

The phonon-polariton response has been extensively investigated in both $LiTaO_3$ and $LiNbO_3$. The polariton dispersion of $LiTaO_3$ and $LiNbO_3$ has been elucidated in detail. The complex part of the dispersion has revealed the coupling of the lower polariton branch to other phonon modes of the system in $LiTaO_3$ and $LiNbO_3$. The dispersion of four transverse optic phonon modes in $LiTaO_3$ has been measured across a broad range of wavevectors. Heterodyne detection has been used to perform the phase sensitive detection of polaritons which have propagated outside of the excitation region.

Their specific results for $LiTaO_3$ and $LiNbO_3$ from Bakker, et. al. were not consistent with frequency domain Raman measurements nor with inelastic neutron scattering, both of which are sensitive enough to detect effects of the magnitude observed by Bakker, et. al. Additionally, the model used to explain the polariton beats is inconsistent with *ab initio* calculations which clearly indicate a two, and not three, well potential for this lowest frequency A_1 phonon.[51] In the present work, heterodyne detection is performed with control of the reference field phase and amplitude, with increased wavevector accuracy, brought on by the use of larger spot sizes and diffractive optics, which leads to increased accuracy of frequency and lineshape determinations, and with no displacement of the probe beam from the excitation area. The polariton beats observed by Bakker, et. al. are not reproduced. Although no definitive explanation for the previous results can be given, it is suggested that they may be caused by sample specific effects (some type of defect states, for example), or that they may be an experimental artifact caused by a temporally unstable and spatially inhomogeneous local oscillator phase.

The advantages brought on by heterodyne detection substantially broaden the class of possible applications for ISRS. The simplification in data form and the increased sensitivity extend the range of samples and excitations suitable to study to include weakly scattering bulk crystals, thin ferroelectric films, and surface excitations and effects in bulk and thin film samples.

REFERENCES

1 M. E. Lines and A. M. Glass, *Principles and Applications of Ferroelectrics and Related Materials* (Clarendon Press, Oxford, 1977).

2 A. S. Barker and R. Loudon, Rev. Mod. Phys. **44,** 18-47 (1972).

3 W. D. Johnston and I. P. Kaminow, Phys. Rev. **168,** 1045-1054 (1968).

4 Y. Okamoto, P.-c. Wang, and J. F. Scott, Phys. Rev. B **32,** 6787-6792 (1985).

5 M.-S. Zhang and J. F. Scott, Phys. Rev. B **34,** 1880-1883 (1986).

6 J. L. Servoin and F. Gervais, Solid State Comm. **31,** 387-391 (1979).

7 A. F. Penna, A. Chaves, P. d. R. Andrade, and S. P. S. Porto, Phys. Rev. B **13,** 4907-4917 (1976).

8 A. F. Penna, A. Chaves, and S. P. S. Porto, Solid State Comm. **19,** 491-494 (1976).

9 A. F. Penna, S. P. S. Porto, and E. Wiener-Avnear, Solid State Comm. **23,** 377-380 (1977).

10 C. Raptis, Phys. Rev. B **38,** 10007-10019 (1988).

11 U. T. Schwarz and M. Maier, Phys. Rev. B **53,** 5074-5077 (1996).

12 U. T. Schwarz and M. Maier, Phys. Rev. B **55,** 11041-11044 (1997).

13 U. T. Schwarz and M. Maier, Phys. Rev. B **58,** 766-775 (1998).

14 Y. Tezuka and S. Shin, Phys. Rev. B **49,** 9312-9321 (1994).

15 D. H. Auston and M. C. Nuss, IEEE J. Quantum Electron. **24,** 184-197 (1988).

16 P. C. M. Planken, L. D. Noordam, J. T. M. Kennis, and A. Lagendijk, Phys. Rev. B **45,** 7106-7114 (1992).

17 T. P. Dougherty, G. P. Wiederrecht, and K. A. Nelson, J. Opt. Soc. Am. B **9,** 2179-2189 (1992).

18 H. J. Bakker, S. Hunsche, and H. Kurz, Rev. of Mod. Phys. **70,** 523-536 (1998).

19 Y.-X. Yan and K. A. Nelson, J. Phys. Chem. **87,** 6240-6256 (1987).

20 Y.-X. Yan and K. A. Nelson, J. Chem. Phys. **87,** 6257-6265 (1987).

21 T. P. Dougherty, G. P. Wiederrecht, K. A. Nelson, M. H. Garrett, H. P. Jensen, and C. Warde, Science **258,** 770-774 (1992).

22 T. P. Dougherty, G. P. Wiederrecht, K. A. Nelson, M. H. Garrett, H. P. Jenssen, and C. Warde, Phys. Rev. B **50,** 8996-9019 (1994).

23 T. P. Dougherty, G. P. Wiedderrecht, and K. A. Nelson, Ferroelectrics **164,** 253-264 (1995).

24 L. Dhar, J. A. Rogers, and K. A. Nelson, Chemical Reviews **94,** 157-193 (1994).

25 L. Dhar, B. Burfeindt, K. Nelson, and C. M. Foster, Ferroelectrics **164,** 1-13 (1995).

26 G. P. Wiederrecht, T. P. Dougherty, L. Dhar, and K. A. Nelson, Ferroelectrics **150,** 103-118 (1993).

27 G. P. Wiederrecht, T. P. Dougherty, L. Dhar, and K. A. Nelson, Ferroelectrics **144,** 1-16 (1993).

28 G. P. Wiederrecht, T. P. Dougherty, L. Dhar, K. A. Nelson, D. E. Leaird, and A. M. Weiner, Phys. Rev. B **51,** 916-931 (1995).

29 H. J. Bakker, S. Hunsche, and H.Kurz, Phys. Rev. Lett. **69,** 2823-2826 (1992).

30 H. J. Bakker, S. Hunsche, and H. Kurz, Phys. Rev. B **48,** 13524-13537 (1993).

31 H. J. Bakker, S. Hunsche, and H. Kurz, Phys. Rev. B **48,** 9331-9335 (1993).

32 H. J. Bakker, S. Hunsche, and H. Kurz, Phys. Rev. B **50,** 914-920 (1994).

33 D. H. Auston, Appl. Phys. Lett. **43,** 713-715 (1983).

34 D. A. Kleinman, and D. H. Auston, IEEE J. Quantum Electron. **QE-20,** 964-970 (1984).

35 D. H. Auston, K. P. Cheung, J. A. Valdmanis, and D. A. Kleinman, Phys. Rev. Lett. **53,** 1555-1558 (1984).

36 O. Albert, M. Duijser, J. C. Loulergue, and J. Etchepare, J. Opt. Soc. B **13,** 29-33 (1996).

37 D. P. Kien, J. C. Loulergue, and J. Etchepare, Opt. Commun. **101,** 53-59 (1993).

38 P. Grenier, D. Houde, S. Jandl, and L. A. Boatner, Phys. Rev. B **50,** 16295-16308 (1994).

39 J. C. Loulergue and J. Etchepare, Phys. Rev. B **52,** 15160 (1995).

40 P. Grenier, D. Houde, S. Jandl, and L. A. Boatner, Phys. Rev. B **47,** 1-4 (1993).

41 D. P. Kien, J. C. Loulergue, and J. Etchepare, Phys. Rev. B **47,** 11027-11030 (1993).

42 J. Etchepare, G. Grillon, A. Antonetti, J. C. Loulergue, M. D. Fontana, and G. E. Kugel, Phys. Rev. B **41,** 12362-12365 (1990).

43 M. E. Lines, Phys. Rev. **177,** 812-818 (1969).

44 M. E. Lines, Phys. Rev. **177,** 797-811 (1969).

45 M. E. Lines, Phys. Rev. **177,** 819-829 (1969).

46 A. A. Maznev and K. A. Nelson, Opt. Lett. **23**, 1319 (1998).

47 J. A. Rogers, M. Fuchs, M. J. Banet, J. B. Hanselman, R. Logan, and K. A. Nelson, Appl. Phys. Lett. **71,** 225 (1997).

48 G. D. Goodno, G. Dadusc, and R. J. D. Miller, J. Opt. Soc. Am. B **15,** 1791 (1998).

49 Y.-X. Yan, E. B. Gamble, and K. A. Nelson, J. Chem. Phys. **83,** 5391-5399 (1985).

50 H. J. Eichler, P. Gunter, and D. W. Pohl, *Laser-Induced Dynamic Gratings* (Springer-Verlag, Berlin, 1986).

51 I. Inbar and R. E. Cohen, Phys. Rev. B **53,** 1193-1204 (1996).

52 D. P. Birnie, J. Appl. Phys. **69,** 2485-2488 (1991).

53 S. C. Abrahams, E. Buehler, W. C. Hamilton, and S. J. Laplaca, J. Phys. Chem. Solids **34,** 521-532 (1973).

54 Y. N. Polivanov and S. N. Poluektov, Sov. Phys. Solid State **20,** 2014-2015 (1978).

55 C. Brennan, Thesis, Massachusetts Institute of Technology, 1997.

56 R. Claus, L. Merten, and J. Brandmuller, *Light Scattering by Phonon-POlaritons* (Springer-Verlag, Berlin, 1975).

57 A. E. Siegman, J. Opt. Soc. Am. **67,** 545-550 (1977).

Appendix 5A. Analysis of heterodyned ISRS data from phonon-polaritons

A classical, linear, single oscillator model was observed to accurately fit all of the data collected from both $LiTaO_3$ and $LiNbO_3$ at all wavevectors. The following model and its prediction follow closely the presentation of ref. 1. The objective will be to determine the trajectories of a ring of N charged, coupled oscillators in planes spaced a distance a apart from one another, which are oscillating in a harmonic potential energy well and which are coupled to an optic field. Begin by first ignoring the coupling to the optical field which will be introduced phenomenologically later on. Consider the first non-zero term in the expansion of the potential energy surface about its equilibrium position. The motion of the oscillators can be determined with the following equation of motion:

$$\sum_{s=1}^{N}\left(\ddot{q}_{s+1}-\ddot{q}_{s}\right)=-\omega_0^2\sum_{s=1}^{N}\left(q_{s+1}-q_{s}\right)-\gamma\sum_{s=1}^{N}\left(\dot{q}_{s+1}-\dot{q}_{s}\right) \tag{A.1}$$

The following notation is in use: q_s is the time dependent displacement of particle s in the ring. The individual displacement coordinates will be transformed to coupled phonon coordinates:

$$q_s = N^{-1/2}\sum_{n=1}^{N} Q_k e^{iksa} \tag{A.2}$$

Examining (A.1) term wise:

$$\begin{aligned}\ddot{q}_{s+1}-\ddot{q}_{s} &= N^{-1/2}\sum_{k=1}^{N}\ddot{Q}_k\left[e^{ik(s+1)a}-e^{iksa}\right]\\ &= N^{-1/2}\sum_{k=1}^{N}\ddot{Q}_k e^{iksa}\left(e^{ika}-1\right)\end{aligned} \tag{A.3}$$

$$q_{s+1} - q_s = N^{-1/2} \sum_{k=1}^{N} Q_k e^{iksa} \left(e^{ika} - 1 \right) \tag{A.4}$$

$$\dot{q}_{s+1} - \dot{q}_s = N^{-1/2} \sum_{k=1}^{N} \dot{Q}_k e^{iksa} \left(e^{ika} - 1 \right) \tag{A.5}$$

Equation (A.1) can be written:

$$\begin{aligned} \sum_{s=1}^{N} N^{-1/2} \sum_{n=1}^{N} \ddot{Q}_{k(n)} e^{ik(n)sa} \left[e^{ik(n)a} - 1 \right] &= \frac{-\omega_0^2}{\sqrt{N}} \sum_{s=1}^{N} \sum_{n=1}^{N} Q_{k(n)} e^{ik(n)sa} \left[e^{ik(n)a} - 1 \right] \\ -\frac{\gamma}{\sqrt{N}} \sum_{s=1}^{N} \sum_{n=1}^{N} \dot{Q}_{k(n)} e^{ik(n)sa} \left[e^{ik(n)a} - 1 \right] & \end{aligned} \tag{A.6}$$

which can be rewritten as follows for any n in the summation:

$$\begin{aligned} \frac{\ddot{Q}_{k(n)}}{\sqrt{N}} \left[e^{ik(n)a} - 1 \right] \sum_{s=1}^{N} e^{ik(n)sa} &= \frac{-\omega_0^2 Q_{k(n)}}{\sqrt{N}} \left[e^{ik(n)a} - 1 \right] \sum_{s=1}^{N} e^{ik(n)sa} \\ + \frac{\gamma}{\sqrt{N}} \dot{Q}_{k(n)} \left[e^{ik(n)a} - 1 \right] \sum_{s=1}^{N} e^{ik(n)sa} & \end{aligned} \tag{A.7}$$

which simplifies to:

$$\begin{aligned} \frac{\ddot{Q}_{k(n)}}{\sqrt{N}} \left[e^{ik(n)a} - 1 \right] &= \frac{-\omega_0^2 Q_{k(n)}}{\sqrt{N}} \left[e^{ik(n)a} - 1 \right] \\ + \frac{\gamma}{\sqrt{N}} \dot{Q}_{k(n)} \left[e^{ik(n)a} - 1 \right] & \end{aligned} \tag{A.8}$$

The strategy will be to solve for the equations of motion for the case in which the oscillators ride in a harmonic potential, but are coupled to an EM field, i.e., solve the classical, linear phonon-polariton problem.

Begin by rewriting (A.8), introducing a phenomenological coupling with the electric field (i.e., the ions are charges and can act upon and be acted upon by the field), and assuming a vector notation:

$$\ddot{\vec{Q}}_{k(n)} = -\omega_0^2 \vec{Q}_{k(n)} + \gamma \dot{\vec{Q}} + b_{12} E \tag{A.9}$$

Maxwell's equations will also have to be considered, and a phenomenological relationship between the polarization and the electric field is posited:

$$\vec{P} = b_{21}\vec{Q}_{k(n)} + b_{22}\vec{E} \tag{A.10}$$

$$\vec{\nabla} \cdot \vec{D} = \vec{\nabla} \cdot (\vec{E} + 4\pi \vec{P}) = 0 \tag{A.11}$$

$$\vec{\nabla} \cdot \vec{H} = 0 \tag{A.12}$$

$$\vec{\nabla} \times \vec{E} = \frac{-1}{c}\dot{\vec{H}} \tag{A.13}$$

$$\vec{\nabla} \times \vec{H} = \frac{1}{c}(\dot{\vec{E}} + 4\pi \dot{\vec{P}}) \tag{A.14}$$

First, consider the static extreme, which allows the neglection of Maxwell's equation which are not necessary in electrostatics. Consider solutions of the form:

$$\vec{E} = \vec{E}_0 \exp(-i\omega t) \tag{A.15}$$

$$\vec{Q}_{k(n)} = \vec{Q}^{(0)}_{k(n)} \exp(-i\omega t) \tag{A.16}$$

$$\vec{P} = \vec{P}_0 \exp(-i\omega t) \tag{A.17}$$

Substituting (A.15), (A.16), and (A.17) into (A.9), (A.10):

$$-\omega^2 \vec{Q}^{(0)}_{k(n)} = b_{11}\vec{Q}^{(0)}_{k(n)} - i\omega\gamma\vec{Q}^{(0)}_{k(n)} + b_{12}\vec{E} \tag{A.18}$$

$$\vec{P} = b_{21}\vec{Q}^{(0)}_{k(n)} + b_{22}\vec{E} \tag{A.19}$$

From (A.18):

$$\vec{Q}^{(0)}_{k(n)} = \left(\frac{b_{12}}{-b_{11} - \omega^2 + i\omega\gamma} \right) \vec{E} \tag{A.20}$$

From (A.19), (A.20) :

$$\vec{P} = \left(b_{22} + \frac{b_{12} b_{21}}{-b_{11} - \omega^2 + i\omega\gamma} \right) \vec{E} \tag{A.21}$$

Comparing with the definition of dielectric displacement :

$$\vec{D} = \vec{E} + 4\pi \vec{P} = \varepsilon \vec{E} \tag{A.22}$$

we have:

$$\varepsilon = 1 + 4\pi b_{22} + \frac{4\pi b_{12} b_{21}}{-b_{11} - \omega^2 + i\omega\gamma} \tag{A.23}$$

in the $\omega=0$ limit, we have:

$$\varepsilon_0 = 1 + 4\pi b_{22} + \frac{4\pi b_{12} b_{21}}{-b_{11}} \tag{A.24}$$

in the $\omega=\infty$ limit :

$$\varepsilon_\infty = 1 + 4\pi b_{22} \tag{A.25}$$

and set ω_0 as the peak in the real part of the dielectric function :

$$\omega_0 = -b_{11} \tag{A.26}$$

(A.26) can be also be chosen to include the damping term (it is the other peak in the response function), but (A.26) will be kept as is to keep with historic convention. It can be written by inspection of (A.23), (A.24), and (A.25):

$$b_{11} = -\omega_0^2 \tag{A.27}$$

$$b_{12} = b_{21} = \left(\frac{\varepsilon_0 - \varepsilon_\infty}{4\pi} \right)^{1/2} \omega_0 \tag{A.28}$$

$$b_{22} = \frac{\varepsilon_\infty - 1}{4\pi} \tag{A.29}$$

$$\varepsilon = \varepsilon_\infty + \frac{\omega_0^2(\varepsilon_0 - \varepsilon_\infty)}{\omega_0^2 - \omega^2 + i\omega\gamma} \tag{A.30}$$

Returning to the dynamic problem, (A.11)-(A.14) will be considered and solutions of the following form will be assumed :

$$\left.\begin{aligned} \vec{Q} &= \vec{Q}^{(0)}_{k(n)} \\ \vec{P} &= \vec{P}_0 \\ \vec{E} &= \vec{E}_0 \\ \vec{H} &= \vec{H}_0 \end{aligned}\right\} e^{-i\omega t} e^{i\vec{k}(\omega)\cdot\vec{r}} + c.c. \tag{A.31}$$

Inserting (A.31) into (A.9)-(A.14):

$$-\omega^2 \vec{Q}^{(0)}_{k(n)} = b_{11}\vec{Q}^{(0)}_{k(n)} - i\omega\gamma\vec{Q}^{(0)}_{k(n)} + b_{12}\vec{E} \tag{A.32}$$

$$\vec{P} = b_{21}\vec{Q}^{(0)}_{k(n)} + b_{22}\vec{E} \tag{A.33}$$

$$i\vec{k}\cdot\vec{E} + 4\pi i\vec{k}\cdot\vec{P} = 0 \tag{A.34}$$

$$i\vec{k}\cdot\vec{H} = 0 \tag{A.35}$$

$$i\vec{k}\times\vec{E} = -\frac{i}{c}\omega\vec{H} \tag{A.36}$$

$$i\vec{k}\times\vec{H} = \frac{1}{c}\left(-i\omega\vec{E} - 4\pi i\omega\vec{P}\right) \tag{A.37}$$

Equations (A.32) and (A.33) will reproduce (A.20) and (A.21). From (A.21) into (A.34):

$$(\vec{k}\cdot\vec{E})\cdot\left\{1 + 4\pi b_{22} + \frac{4\pi b_{12}b_{21}}{-b_{11} - \omega^2 + i\omega\gamma}\right\} = 0 \tag{A.38}$$

It can be shown that the $\vec{k}\cdot\vec{E} = 0$ case corresponds to the transverse phonon-polariton while the case is which the bracketed term equals zero corresponds to the uncoupled longitudinal phonon and photon. Consider just the polariton (transverse) case:

$$\vec{k} \cdot \vec{E} = 0 \tag{A.39}$$

$\vec{k}, \vec{E}, \vec{H}$ form a right handed coordinate system and from (A.36):

$$kE = \frac{-\omega}{c} H \tag{A.40}$$

and from (A.37) :

$$kH = \frac{-\omega}{c}(E + 4\pi P) \tag{A.41}$$

From (A.40), (A.21) into (A.41):

$$\frac{k^2 c^2}{\omega^2} = 1 + \frac{4\pi b_{12} b_{21}}{-\omega^2 - b_{11} + i\omega\gamma} + 4\pi b_{22} \tag{A.42}$$

This provides the well known polariton dispersion relation. The vector notation will be dropped at this point. In the impulsive limit, the Raman force has the effect of preparing the polariton with a spatially varying initial velocity distribution. We'll assume that we're in the classical T=0 limit. Combining these two statements gives the following initial conditions on the problem :

$$\dot{Q}(t=0) = -\pi \varepsilon_0 \varepsilon_\infty^2 r_{33} \omega_0 \left(\frac{\varepsilon_0 - \varepsilon_\infty}{4\pi} \right)^{-1/2} I(\vec{r}) \tag{A.43}$$

$$\mathrm{Re}\left[Q(t=0)\right] = 0 \tag{A.44}$$

The ISRS driving force is applied by an optical field with intensity profile

$$I(\vec{r}) = I_0 \cos(q\vec{r}) \tag{A.45}$$

From (A.43) we get :

$$\begin{aligned} Q_q^{(0)} &= -\pi \varepsilon_0 \varepsilon_\infty^2 r_{33} \omega_0 \left(\frac{\varepsilon_0 - \varepsilon_\infty}{4\pi} \right)^{-1/2} I_0 \frac{i}{\omega} \\ Q_{k(n)}^{(0)} &= 0 \quad for\, k(n) \neq q \end{aligned} \tag{A.46}$$

The temporal polariton response to a driving force with wavevector q is a damped sine wave with a frequency given by the real solution (A.42) and damping given by the imaginary part of (A.42). In order to compare ISRS experimental data with the predictions of this model, it will be necessary to determine if the polariton response at a given wavevector can be well fit by a damped sine function with frequency ω_0 and damping γ and to determine if ω_0 and γ have the wavevector dependence predicted by (A.42).

Three methods were employed to determine the frequency and damping from experimental ISRS data. First, the data were fit in the time domain to a damped sine function using the Levenburg-Marquardt algorithm. Second, a power spectrum estimation was taken of the data using the conventional FFT algorithm (see Chapter 5), and this was fit to a Lorenzian function (see description below). Third, a power spectrum estimation was taken of the data using the maximum entropy method (MEM) and this frequency domain result was fit to a Lorenzian lineshape. The effectiveness of each method was evaluated based upon several considerations. A sample data set (without noise) was generated from known parameters and the data were fit using all three methods. The MEM performed poorly, routinely underestimating the linewidth by 10%. Additionally, the MEM produced spurious peaks when greater than 50 poles were used. Accordingly, the MEM was rejected for this application. Both of the other techniques performed well when fitting the sample data set. In data sets in which multiple frequency components were present, the time domain fit performed poorly, even when additional damped sine functions were added to the fit function. These fits were extremely sensitive to the initial parameter estimates and there appeared to be considerable coupling between various

parameters in the fit function. Consequently, the time domain fit was rejected for this application.

A conventional fast fourier transform algorithm, written in C, was used to perform the power spectrum estimation of the data. The functional form of the power spectrum of a damp sine wave will be shown to be a Lorezian lineshape. Consider the power spectrum of the heterodyne signal $I_S(t) = \sin(\omega_v t) e^{-\gamma t/2}$ where $\omega_v = \sqrt{\omega_0 - \gamma^2/4}$. The fourier transform is given by:

$$I_S(\omega) = \int_{-\infty}^{\infty} \sin(\omega_v t) e^{-\gamma t/2} e^{i\omega t} dt \tag{A.47}$$

which can be simplified to:

$$I_S(\omega) = \frac{1}{2} \frac{-\omega_v - i\gamma/2}{\omega^2 - \omega_v^2 + i\gamma\omega - \gamma^2/4} \tag{A.48}$$

The power spectrum is given by:

$$PS = |I_S(\omega)|^2 = \frac{1}{4} \frac{\omega_0^2}{4\omega_0^2 (\omega - \omega_0)^2 + \gamma^2\omega^2} \tag{A.49}$$

For ω approximately equal to ω_0, this can be expressed as a Lorenzian function:

$$PS \cong \frac{1}{4} \frac{1}{4(\omega - \omega_0)^2 + ^2} \equiv L(\omega) \tag{A.50}$$

The power spectrum of the data was fit with the Lorenzian function from (A.50) using the Levenburg-Marquardt algorithm in Origin, a commercial spreadsheet package.

It is important to note that the wavevector of the optical interference pattern k_g is not equal to the wavevector of the polariton, because of the forward component required by wavevector conservation[2]. In order to determine the polariton wavevector, the forward

component of the wavevector k_f must be found. Assume that the sample has index of refraction n_r and that the sample is surrounded by air n=1. The incident angle of a beam will be denoted θ_i while the angle in the material will be θ_r. The forward velocity of light in the sample is given by:

$$\begin{aligned}\left(v_f^l\right)^2 &= \frac{c^2}{n_r^2 \cos^2\theta_r} \\ &= \frac{c^2}{n_r^2\left(1-\sin^2\theta_r\right)} \\ &= \frac{c^2}{n_r^2\left(1-\dfrac{\sin^2\theta_i}{n_r^2}\right)} \\ &= \frac{c^2}{n_r^2-\sin^2\theta_i}\end{aligned} \tag{A.51}$$

The forward wavevector component is given by:

$$k_f^2 = \frac{\omega^2}{\left(v_f^l\right)^2} = \frac{\omega^2\left(n_r^2-\sin^2\theta_i\right)}{c^2} \tag{A.52}$$

The total polariton wavevector k_p can be found from:

$$k_p = \sqrt{k_f^2+k_g^2} = \sqrt{\frac{\omega^2\left(n_r^2-\sin^2\theta_i\right)}{c^2}+\frac{4\pi^2}{\Lambda^2}} \tag{A.53}$$

where $k_g = 2\pi/\Lambda$ is the interference grating wavevector. The procedure for determining the polariton wavevector will be to measure θ_i at the sample, to measure ω from the power spectrum of the data, and then to determine the polariton wavevector according to (A.53).

References

1 M. Born and K. Huang, *Dynamical Theory of Crystal Lattices* (Oxford University Press, Oxford, 1954).
2 C. Brennan, Thesis, Massachusetts Institute of Technology, 1997.

Chapter 6. Future Work and Conclusions

I. A simple terahertz spectrometer

Light in the far IR spectral region is rapidly evolving as a valuable tool in the spectroscopic study of liquids[1-3], dielectrics[4], gasses[5-7], semiconductors[8,9], and superconductors[10,11] and as an illumination source for the chemically sensitive imaging of everything from integrated circuits to biological samples[12-14]. Spectroscopy in this terahertz (10^{12} hz) frequency regime is especially potent in liquids, where it probes properties on length and time scales in between those characteristic of bulk dielectric responses and intermolecular motions. In glass-forming liquids, the terahertz dielectric response is crucially important. Theoretical predictions [15,16] have been made concerning it, but ordinary dielectric spectroscopy only gets to around 100 GHz with standard techniques and up to 400 GHz[17]only with considerable difficulty. "T"-ray imaging, or imaging of objects with terahertz radiation, has a diverse range of potential applications including trace gas analysis, safe packaging inspection, and biological imaging. Polar liquids, such as water, tend to strongly absorb terahertz radiation while most dry, nonmetallic materials are highly transparent, motivating a demonstrative application of "T"-ray imaging to the mapping of water in leaves[13].

The experimental challenges involved in the generation and detection of terahertz radiation stand as the main impediments to its more widespread application. Microwaves, which border "T"-rays on the low frequency side, are typically generated using high frequency electronics while infrared waves, on the high frequency border, are generated by light sources, usually via blackbody radiation or lasers. The fastest electronic devices operate at around 100 GHz and the intensity of blackbody radiation is extremely dim

much below 10 THz, leaving a substantial gap that has just recently been bridged with a practical source. The illumination of photoconducting dipole antennas with femtosecond optical pulses was shown to radiate broad bandwidth, coherent bursts of light with substantial spectral density from 100 GHz to 5 THz. [18-23] This terahertz radiation, which was propagated through free space, could be focused or collimated using far IR optics (typically large gold reflectors), passed through a sample, and detected using another, similar photoconducting dipole antenna, which is gated by a variably-delayed femtosecond pulse. The spectroscopy and imaging applications discussed above were all performed with this general technique, whose main drawbacks are its requirements for far-IR optics, carefully fabricated, complex photoconducting dipole antennas, and, for some applications, the extremely broad bandwidth of the THz burst.

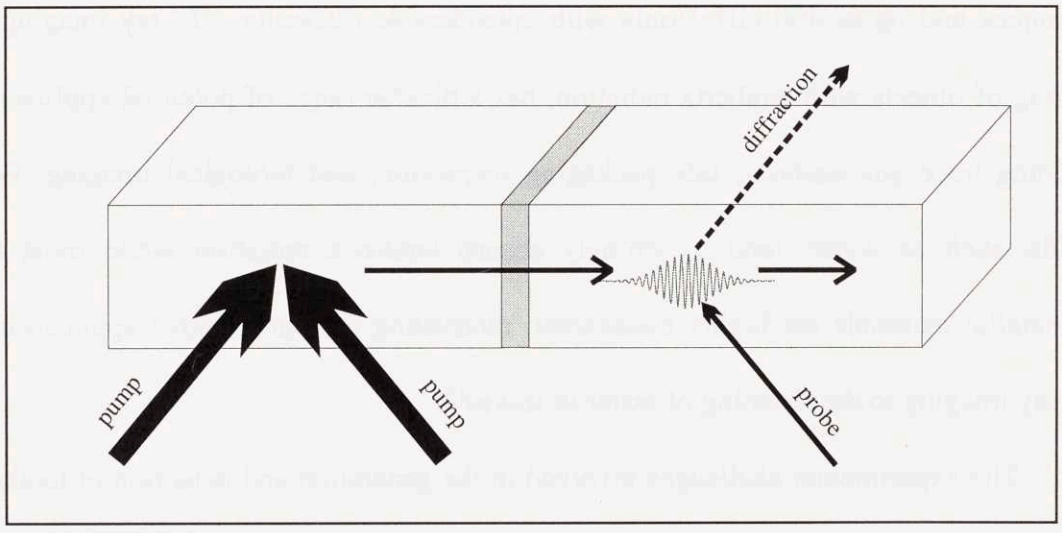

Fig. 6.1. A schematic drawing of a simple terahertz spectrometer. Phonon-polariton are excited in one ferroelectric crystal, propagated through a liquid sample, and detected in a second crystal .

Figure 6.1 depicts an alternate apparatus for conducting terahertz spectroscopy of liquids that has only visible light pulses as inputs and outputs and that requires no far-IR optics or special antennas. In this apparatus, two femtosecond pulses in the visible region

of the spectrum are interfered in one $LiTaO_3$ crystal, driving a mixed mechanical-electromagnetic wave via impulsive stimulated Raman scattering[24-26]. Called a phonon-polariton, this wave has the same spatial periodicity as the interfering pulses, and it is frequency tunable between roughly 0.5-6 THz by adjusting the periodicity. Propagating through the crystal at one-sixth the speed of light in air, the polariton is partially coupled (~50% of the EM energy would be coupled into water) into a liquid sample. It enters a second $LiTaO_3$ crystal where it is detected by monitoring of the heterodyned diffraction (see Chapter 4) of a variably delayed, visible probe pulse with a conventional silicon photodiode. Preliminary data are plotted in Figure 6.2, where the responses from polaritons that have and have not propagated through the liquid sample layer are plotted together for comparison. The attenuation and phase shifting of the electromagnetic portion of the polariton caused by propagation through the liquid can clearly be determined from these data, which reveals the dielectric response of the liquid in the terahertz regime. It must be emphasized that the terahertz radiation never leaves the crystal-sample-crystal assembly, only visible light is used, and no IR optics or detectors are necessary.

This technique possesses many advantages. The terahertz radiation is tunable and the bandwidth is controlled by simply adjusting the spot size of the excitation beams. Both the real and imaginary part of the dielectric constant can be measured simultaneously. Finally, the high intensities of the polaritons should make non-linear optical measurements, such as hole burning and pump-probe spectroscopy, a real possibility.

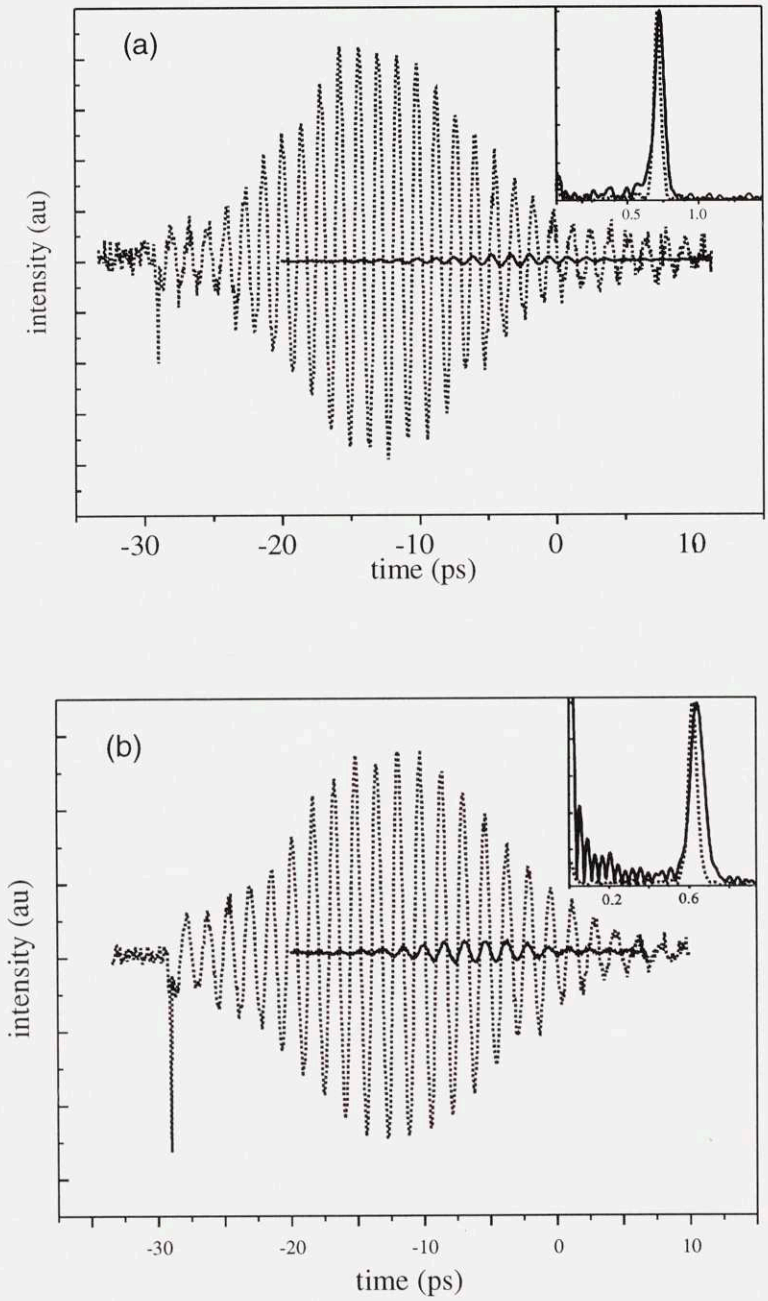

Fig. 6.2. A terahertz bandwidth polariton wavepacket detected after propagating through only $LiTaO_3$ (dotted line) or a $LiTaO_3$-glycerol-$LiTaO_3$ cell (solid line). A 65 μm garting spacing (a) corresponding to a frequency of 0.7 THz and a 75 μm grating spacing (b) corresponding to a frequency of 0.6 THz are shown. The glycerol layer was ~250 μm thick and the polariton was detected after propagating 1mm. The inset plots the power spectrum of both wavepackets.

Several crucial experimental variables were left uncontrolled in the demonstrative experiments the results of which are shown in figure 6.2. The spacing between the two crystals was on the order of 1mm but was not known to a high degree of accuracy. A special sample cell has been fabricated to increase the degree of accuracy to which this spacing is known, and experiments with this cell will soon be performed. A second, serious omission was the failure to measure the incident angle of the beams upon the sample. At the low wavevectors used in these experiments, the polariton has a substantial forward wavevector component (see appendix 5A) as illustrated in figure 6.3 and the polariton propagates through the crystal at a significant angle (~20°) with respect to the crystal face. Because of the extreme refractive index mismatch between the ferroelectric crystal and the liquid sample, the magnitude of the polariton transmission through the crystal-liquid interface is a strong function of the angle between the crystal y-face and the polariton (see figure 6.4). Assuming that the bisector ofthe incident beams is normal to the crystal's x-face, the polariton will undergo total internal reflection from the crystal-liquid (ε=5) interface, which implies that this angle was at least ten degrees in the experiments whose results are shown in figure 6.4. It will be important to carefully control this angle when these experiments are repeated. Additionally, the angle between bisector of the incident beams and the x-face of the crystal should be set quite high to maximize transmission through the two interfaces. Finally, it will be important to model the effect that polaritons reflected off of the back face of the crystal have on the form of the heterodyne signal, a task that will also be required in the analysis of the thin crystal data presented below in section II.

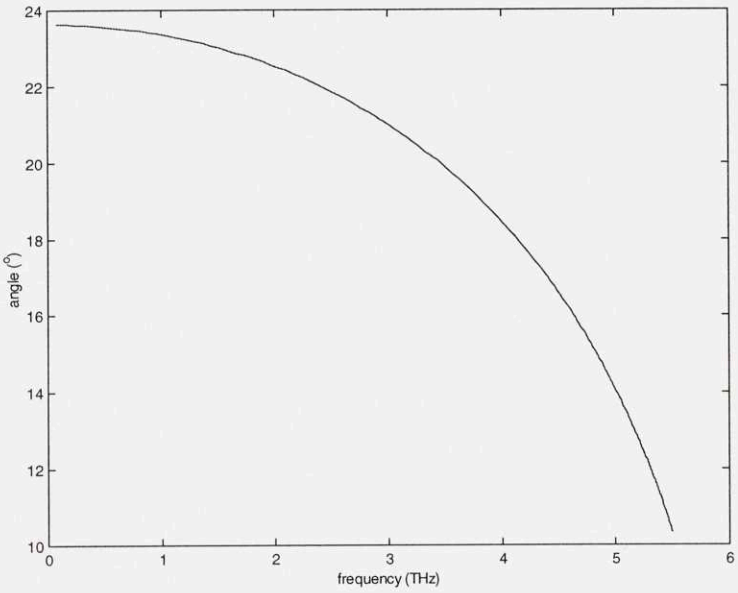

Fig. 6.3. A plot of polariton angle with respect to the y-face as a function of frequency for $LiTaO_3$. The polariton wavevector picks up a substantial forward component at low frequencies.

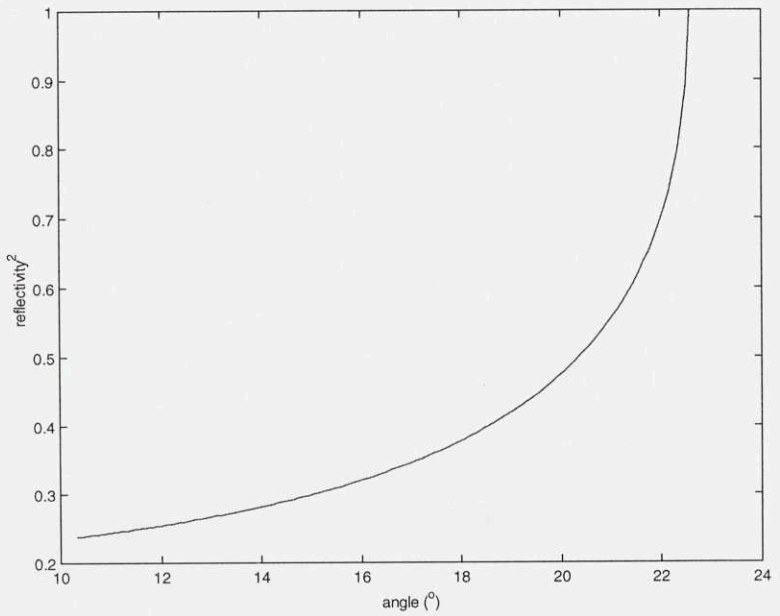

Fig. 6.4. The reflectivity of a $LiTaO_3$-liquid (n=5) interface is plotted a function of polariton angle. Total internal reflection sets in at roughly 22°.

In conclusion, potential applications of a newly developed experimental method for generation and detection of narrowband, frequency-tunable, high-power terahertz radiation and shaped terahertz waveforms were explored. This technique will provide relatively simple access to a host of properties of fundamental and applied interest in an extremely broad range of samples.

II. Heterodyned ISRS from thin $LiTaO_3$ crystals

Ultrafast spectroscopic studies of thin ferroelectric films are expected to reveal interesting new phenomena: polariton surface and waveguide modes as well as coupled poalriton modes in hybrid ferroelectric-semiconductor structures should all be observed. Because the diffraction efficiency from a 1 mm crystal will be a factor of 10^6 greater than that from a 1 μm film, considerable detection sensitivity is required to monitor these polaritons responses in thin films. In addition, the surface, waveguide, and coupled modes are all expected to exhibit complicated responses consisting of many frequencies. Heterodyne detection is an ideal method for studying thin film responses as it provides exceptional sensitivity and signal clarity.

Devices consisting of ultrafast laser systems and ferroelectric materials have considerable potential in the fields of high bandwidth signal processing and optical communication, and ferroelectric DRAMs already enjoy commercial use. In general, higher bandwidth will be possible with signals written into phonon-polariton wavepackets, which can contain bandwidths of up to several terahertz. Optical readout of the wavepacket would be performed (after propagation or manipulation of the polariton) by a probe beam set in spatially distinct region of the device. Practical devices will likely

be built from thin (~1 μm) ferroelectric films because of the relative ease of fabrication of such films compared with bulk crystals. Additionally, the polariton response of a thin film is expected to differ markedly from that of a bulk sample, as waveguide effects are expected to become prominent as the sample thickness approaches the polariton wavelength[27].

In this section, preliminary ISRS results from ferroelectric films are presented, with data collected from a 100 μm $LiTaO_3$ at a range of low wavevectors being reported. A crystal of this thickness is expected to show properties between that of the thin film and the bulk. Data from several wavevectors are presented in figure 6.5, alongside data collected from a 1mm thick crystal in figure 6.6. At these long polariton wavelengths (50-100μm), the polariton response from the 100 μm crystal is already seen to be quite different from that of the bulk sample. Multiple frequency components are observed in all wavelengths from 50-100μm. While these data yet been quantitatively modeled, it is likely that the beating patterns are a consequence of the onset on waveguide behavior. In these crystal samples, which are still reasonable thick by waveguide standards at 100μm, it should be possible to model the signal by considering the polariton as a wavepacket repeatedly reflecting off of the front and back crystal surfaces. In this case, it will be necessary to determine the diffraction efficiency from a sample with an arbitrary, depth dependent, refractive index profile.

Excellent signal to noise ratios were achieved with acquisition times of roughly 10 minutes and excitation beam intensities of between 10 and 75 μJ / pulse (horizontal spot sizes of FWHM~800 nm). With increased excitation beam intensities, decreased spot

sizes, and/or the use of lasers with higher repetition rates, the goal of achieving rapid polariton response characterization from 1 μm films appears to be quite plausible.

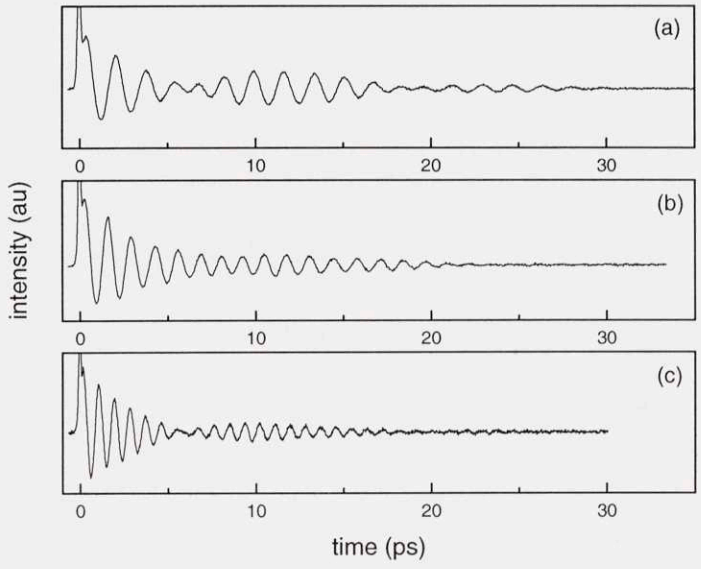

Fig. 6.5. Heterodyned ISRS data from a 100 μm $LiTaO_3$ with three grating wavelengths shown: (a) 89 μm (b) 68 μm (c) 44 μm. Beating patterns, assigned to waveguide effects, are visible at all wavevectors.

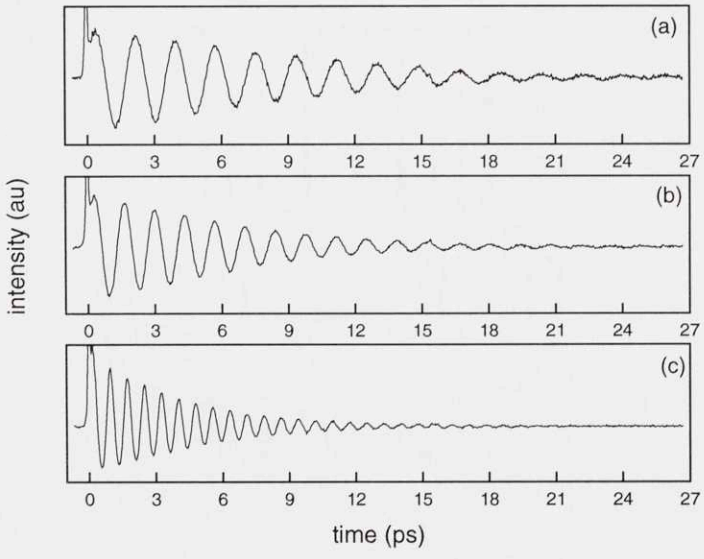

Fig. 6.6. Heterodyned ISRS data from a 1 mm $LiTaO_3$ with three grating wavelengths shown: (a) 89 μm (b) 68 μm (c) 44 μm. No beating is observed in contrast to fig. 6.5.

III. Conclusions

An optical apparatus has been developed for the femtosecond time-scale, heterodyne detection of transient gratings using a diffractive optic to split the reference and probe beams as well as to separate the excitation pulses. This apparatus maintains phase stability amongst all beams over long periods of time, permitting optical heterodyne detection to be conducted without active stabilization. The apparatus also features improvements in transverse wavevector resolution and ease of alignment compared with traditional, beamsplitter based transient grating methods. Additionally, an electronics system has been developed for computer-controlled, 1 kHz acquisition of short-pulse heterodyne transient grating data.

This apparatus was applied to heterodyne ISRS studies of the A_1 phonon modes of the prototype ferroelectrics $LiTaO_3$ and $LiNbO_3$. This work served to clear up contradictory results and provide further validation for a double-well model of the potential energy surface of the lowest frequency A_1 phonon-polariton in the two crystals. The behavior of this mode, which takes the ions from their position in the paraelectric phase to their position in the ferroelectric phase, is extremely important to understand, as it provides clues about the origins of ferroelectricity in these materials. The heterodyne ISRS technique was used to map the complex dispersion of all four A_1 modes of $LiTaO_3$ across 16,000 cm^{-1}. A Fermi resonance between the lowest frequency A_1 phonon-polariton and a 140 cm^{-1} E symmetry phonon was suggested as the cause of an anomolous peak in the imaginary part of the $LiTaO_3$ dispersion. Finally, the heterodyne detection of propagating responses was investigated both theoretically and experimentally.

Heterodyne ISRS data were seen to take their simplest form when propagating responses were measured either in the excitation region or completely outside of it, as phase shifts in the time domain are expected for intermediate probe displacements for many values of reference phase.

A simple terahertz spectrometer was built using only visible light as its inputs and outputs. This device, which took advantage of the improved sensitivity of the heterodyne ISRS technique, changed the role of propagating polariton waves from passive participants in studies of the host medium to active actuators in the study of the terahertz dielectric properties of the polar liquid glycerol. The dielectric properties in this region of the frequency spectrum provide important information about properties of the liquid that fall between the bulk elastic and the microscopic, information that is critical in understanding the liquid-glass transition.

Heterodyne ISRS data were collected from thin $LiTaO_3$ crystals. These data show the apparent onset of waveguide behavior in phonon-polaritons as the polariton wavelength approaches the crystal thinckness. For a broad range of materials and prospective photonic devices, thin film samples and structures represent the only plausible fabrication options, making the ability to collect and understand data from such systems necessary for continued develpoment in these areas.

The transient grating technique has been applied to the detection of surface and bulk through-plane acoustic waves in metal films. Surface displacement was shown to be the primary diffraction mechanism in both nickel and aluminum. A computational method was developed to simulate through-plane ISTS data from multi-layer metal film structures. Transient gratring ISTS was shown to be a metrology tool capable of

extracting information about the morphology of metal films and the thicknesses of individual layers in multi-layer film stacks.

The femtosecond time-scale, heterodyne transient grating technique extends our ability to study nature with light. Gigahertz and terahertz bandwidth responses have been studied and presented from metal film structures, bulk and thin film ferroeletrics, and polar liquids, which highlight the method as a valuable tool in the study of complex, dispersive materials. It has been shown that projects incorporating this technique have made important contributions to science, and early results indicate that they will continue to do so well into the future.

References

1 J. T. Kindt and C. A. Schmuttenmaer, J. Phys. Chem. **100,** 10373-10379 (1996).

2 J. E. Pedersen and S. R. Keiding, IEEE J. Quantum Electron. **28,** 2518 (1992).

3 L. Thrane, R. H. Jacobsen, U. Jepsen, and S. R. Keiding, Chem. Phys. Lett. **240,** 330 (1995).

4 D. Grischkowsky, S. Keiding, M. v. Exter, and C. Fattinger, J. Opt. Soc. Am. B **7,** 2006 (1990).

5 H. Harde and D. Grischkowsky, J. Opt. Soc. Am. B **8,** 1642 (1991).

6 H. Harde and N. Katzenellenbogen, J. Opt. Soc. Am. B **11,** 1018 (1994).

7 R. H. Jacobsen, D. M. Mittleman, and M. C. Nuss, Optics Letters **21,** 2011 (1996).

8 M. v. Exter and D. Grischkowsky, Phys. Rev. B **41,** 12140 (1990).

9 S. E. Ralph, S. Perkowitz, N. Katzenellenbogen, and D. Grischkowsky, J. Opt. Soc. Am. B **11,** 2528 (1994).

10 B. I. Greene, J. F. Federici, D. R. Dykaar, A. F. J. Levi, and L. Pfeiffer, Opt. Lett. **16,** 48 (1991).

11 R. H. M. Groeneveld and D. J. Grischkowsky, J. Opt. Soc. Am. B **11,** 2502 (1994).

12 M. C. Nuss, in *IEEE Pamphlet No. 8755-3996/96* (1996), p. 25-30.

13 B. B. Hu and M. C. Nuss, Optics Letters **20,** 1716 (1995).

14 D. M. Mittleman, R. H. Jacobsen, and M. C. Nuss, IEEE Seected Topics in Quantum Electronics **2,** 679 (1996).

15 W. Gotze and L. Sjogren, Rep. Prog. Phys. **55,** 241 (1992).

16 K. L. Nagi and e. al., J. Chem. Phys. **86,** 4768 (1987).

17 P. Lunkenheimer, A. Pimenov, M. Dressel, Y. G. Goncharov, R. Bohmer, and A. Loidl, Phys. Rev. Lett. **77,** 318 (1996).

18 P. R. Smith, D. H. Auston, and M. C. Nuss, IEEE Journal of Quantum Electronics **24,** 255 (1988).

19 G. Mourou, C. V. Stancampiano, A. Antonetti, and A. Orszag, Appl. Phys. Lett. **45,** 295-296 (1981).

20 R. Heidemann, T. Pfeiffer, and D. Jager, Electron. Lett. **19,** 316-317 (1983).

21 D. H. Auston, K. P. Cheung, and P. R. Smith, Appl. Phys. Lett. **284-286,** 284 (1984).

22 J. R. Karin, P. M. Downey, and R. J. Martin, IEEE J. Quantum Electron. **QE-22,** 677-681 (1986).

23 A. P. DeFonzo and C. R. Lutz, Appl. Phys. Lett. **51,** 212-214 (1987).

24 D. H. Auston, Applied Physics Letters **43,** 713-715 (1983).

25 Y.-x. Yan and K. A. Nelson, The Journal of Physical Chemistry **87,** 6240-6256 (1987).

26 Y.-X. Yan and K. A. Nelson, The Journal of Chemical Physics **87,** 6257-6265 (1987).

27 E. Garwire, in *Electromagnetic Surface Excitations*, edited by R. F. Wallis and G. I. Stegeman (Springer-Verlag, Berlin, 1986).